Studies on Roles of Nonmuscle Myosin II Isoforms in Stress Fiber Organization and Directionally Persistent Migration of Fibroblasts

By
Masahiro KURAGANO

Dissertation

Graduate School of Chemical Sciences and Engineering,
Hokkaido University

2018

Index

Abbreviation list

BBS: blebbistatin
CCD: charge coupled device
DAPI: 4',6-diamidino-2-phenylindole
DMEM: Dulbecco's modified Eagle's medium
dSF: dorsal stress fiber
EGFP: enhanced green fluorescent protein
FA: focal adhesion
FBS: fetal bovine serum
FITC: fluorescein isothiocyanate
HMM: heavy meromyosin
KD: knockdown
MTOC: microtubule-organizing center
NLS: nuclear localization signal
NMHC: nonmuscle myosin heavy chain
NMII: nonmuscle myosin II
PAGE: polyacrylamide gel electrophoresis
PCR: polymerase chain reaction
RLC: regulatory light chain
PBS: phosphate-buffered saline
SF: stress fiber
siRNA: small interfering RNA
S1: subfragment 1
TA: transverse arc
TBS: tris buffered saline
TFM: traction force microscopy
TRITC: tetramethylrhodamine
vSF: ventral stress fiber
WT: wild type
0P-RLC: dephosphorylated regulatory light chain
1P-RLC: monophosphorylated regulatory light chain at Ser19
2P-RLC: diphosphorylated regulatory light chain at Thr18 and Ser19

Introduction

1: Nonmuscle myosin II

Nonmuscle myosin II (NM II) plays a key role in diverse types of cellular motility by generating contractile forces together with actin filaments [1,2]. NMII is composed of a pair of heavy chains and two pairs of light chains. This motor protein comprises two globular heads, which are involved in motor activity, and a long rod-like tail, which is involved in filament formation (Figure 1). The motor head domain including neck region is called subfragment 1, S1.

2: Regulation of activity of NMII

The motor activity and filament formation of NMII are dependent on phosphorylation of its regulatory light chain (RLC) subunit at Thr18 and Ser19 by several kinases such as ROCK/Rho-kinase and myosin light chain kinase [2,3] (Figure 2). Phosphorylation of RLC at Ser19 (1P-RLC) increases actin-activated Mg^{2+}-ATPase activity and promotes filament formation. Diphosphorylation of RLC at Thr18 and Ser19 (2P-RLC) results in a further increase of actin-activated Mg^{2+}-ATPase activity and NMII filament stability [4,5] (Figure 3). These activations are required for the assembly and maintenance of stress fibers (SFs), as well as for the maturation of focal adhesions (FAs) [2,6]. Furthermore, Rho-kinase directly diphosphorylates RLC [7]. Distinct localization of 1P-RLC and 2P-RLC was indicated in SFs [8–11], however, these studies did not focus on the differences of SF subtypes. On the other hands, although it was reported that the localization of either one of 1P-RLC or 2P-RLC in SF subtypes [12–14], the functional differences between 1P-RLC and 2P-RLC in SF subtypes are still unclear.

3: NMII isoforms

In mammalian cells, there are three isoforms of nonmuscle myosin heavy chain (NMHC), namely, NMHC-IIA, NMHC-IIB, and NMHC-IIC. Nonmuscle myosin IIA (NMIIA), IIB (NMIIB), and IIC (NMIIC) are homodimeric with respect to their corresponding heavy chain subunit composition [2,3,15]. *In vitro* studies revealed that these isoforms have distinct motor properties [16–19]. NMIIA exhibits higher motor activity for translocation of actin filaments than NMIIB. On the other hand, NMIIB exhibits slow ADP release and high ADP affinity, resulting in a high duty ratio (the fraction of time that the NMII head spends in the strong actin-binding states during the ATPase cycle). Based on these distinct motor properties, NMIIA and NMIIB have been suggested to mainly function in the translocation (motor property) and crosslinking (structural property) of actin filaments, respectively [2,3,16,19–21]. Moreover, the ADP release rate of both isoforms, especially NMIIB, is decreased by the resisting load, suggesting that NMIIB has a role to maintain tension [19] (Figure 4).

4: Stress fiber subtypes

SFs are contractile, force-generating bundled structures consisting mainly of actin filaments, NMII filaments, and α-actinin. These fibers are prominent in cultured mesenchymal cells, such as fibroblasts and osteoblasts, as well as in cultured smooth muscle cells (Figure 5). There are three subtypes of SFs, namely, ventral SFs (vSFs), transverse arcs (TAs), and dorsal SFs (dSFs), which are categorized based on their distinct subcellular localizations and termination sites (Figure 6) [22–26]. vSFs are tightly packed actomyosin bundles located along the basal surface of cells. Both ends of vSFs link to FAs. vSFs mediate stable adhesion with the underlying substrate and also facilitate contraction of the rear of migrating cells. Both TAs and dSFs are present in highly protrusive cells that possess flat lamellae. TAs are curved actomyosin bundles that form beneath the dorsal surface of lamellae. They undergo centripetal flow toward the cell body and eventually disappear near the end of the lamella [27–29]. TAs, which do not directly link to FAs at both ends, mediate the periodic protrusion and retraction of the leading edge of cells during migration [28]. dSFs are relatively short actin filament bundles that are prominent in lamellae. They link to FAs only at the distal end of the ventral surface and often connect to TAs at right angles at the proximal end of the dorsal surface. Some dSFs connect to regions close to the ends of TAs [30]. dSFs act to transmit the force, which is generated by the contraction of TAs, to substrates [14,31,32].

Although several studies demonstrated that both NMIIA and NMIIB are involved in the formation of SFs and FAs [33–42], most of them did not focus on the categorization of SF subtypes. On the other hand, many important findings on the function of NMII in the organization of SF subtypes have been reported [14,30–32,43]. However, most of these studies did not address the different roles of NMIIA and NMIIB in the organization of each SF subtype. Therefore, clarifying the relationship between properties of NMII isoforms and organization of SF subtypes is an important theme for the cytoskeleton field.

5: Cell migration

Cell migration is essential for embryogenesis, the immune response, and wound healing [44]. Determination of the cell front and rear, i.e. establishment of migratory polarity is necessary for directional cell migration (Figure 7A) [45]. Cell migration consists mainly of four processes, namely, (i) protrusion of membrane lamellipodia or filopodia by actin polymerization, (ii) formation of new adhesive structures, (iii) translocation of the cell body forward, and (iv) disruption of cell-substratum attachments and tail retraction. By repeating these process, the cells continue to migrate (Figure 7B) [46,47] . Rac1 and Cdc42 of the small G protein Rho family are activated in the cell anterior to induce lamellipodia and filopodia, respectively [48,49]. Thus, establishment of migratory polarity is essential for the cell migration. There are two factors which

regulates the directional migration; one is external regulation and the other is the intrinsic cell directionality (Figure 8) [50]. The external regulation is response to external stimulations such as chemoattractant, extracellular matrix, and mechanical signal. When cells sense the asymmetric gradient of a certain stimulation, the directional migration is induced. On the other hands, the intrinsic directionality was observed without external stimulations. Actually, certain cells with a high level of intrinsic directionality display directionally persistent migration even in the presence of uniform concentrations of chemoattractants [50]. It was reported that the Rac1 activity regulates the intrinsic directionality in several fibroblasts, that is, the restricted activation of Rac1 in the leading edge promotes the highly directional migration [51]. However, the molecular mechanism via which intrinsic cell directionality is mostly unresolved.

NMII plays an essential role in intrinsic cell directionality through the maintenance of cell morphology [50]. It has been reported that NMIIA is present throughout cells, whereas NMIIB is generally excluded from the lamellar region of stationary cells and the anterior lamellar region of migrating cells [9,20,52–54]. In addition, the distinct properties of NMII isoforms are important for the regulation of intrinsic directionality of migrating cell. NMIIA is indicated to play a role in the formation of a stable protrusion in the anterior region of fibroblasts through the proper regulation of Rac1 signaling [37]. On the other hand, NMIIB is suggested to promote directional migration by mediating the formation of contractile actomyosin bundles in the posterior region [55]. However, there remain unanswered questions regarding the roles of NMII isoforms in intrinsic and directed migration (IDM) of cells.

6: Purpose of this study.

In this study, I elucidated whether NMII isoforms play distinct roles in organization of SF subtypes and regulation of IDM in fibroblasts. To investigate the detailed function of the NMIIA and NMIIB in distinct two stage of cytoskeleton regulation, I performed knockdown (KD) experiment using isoform-specific small interfering RNAs (siRNAs) and analyzed the dynamics of SF subtypes in human immortalized fibroblasts and the migration style of normal human fibroblasts.

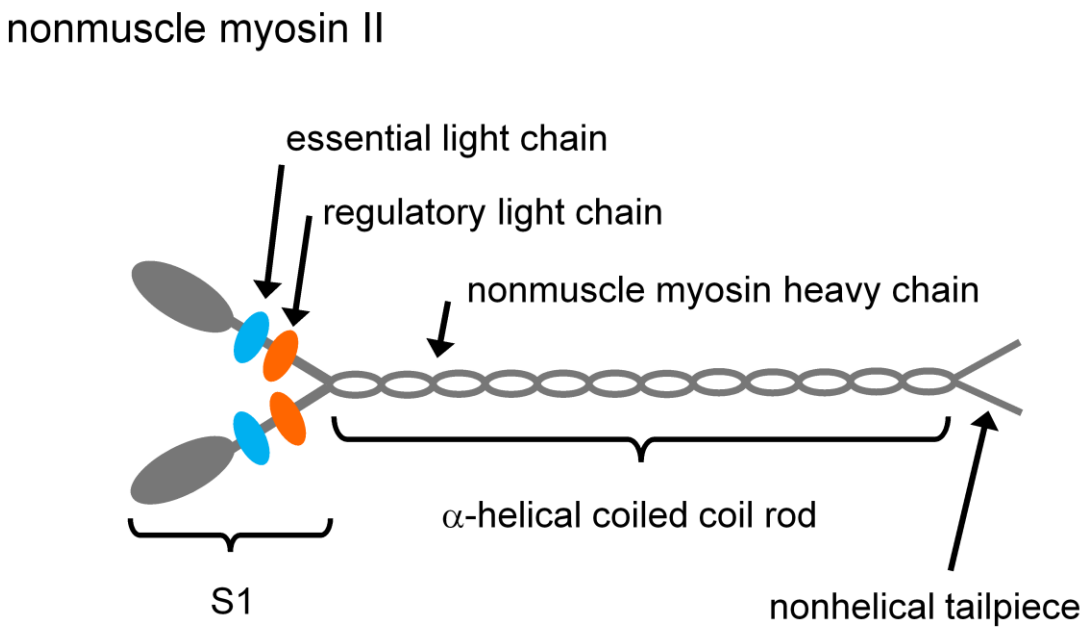

Figure 1. Domain structure of NMII.

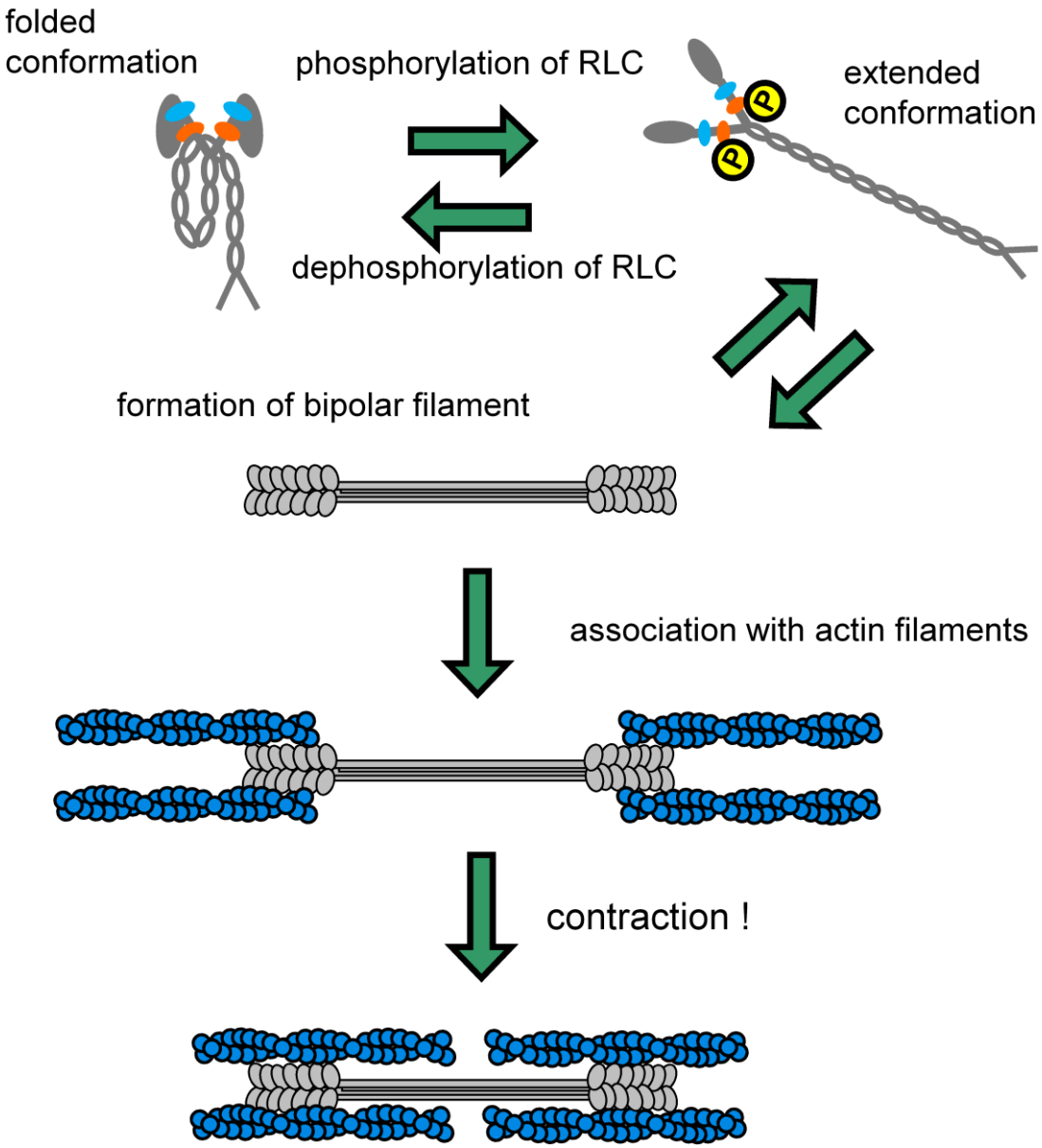

Figure 2. Conformation of NMII.

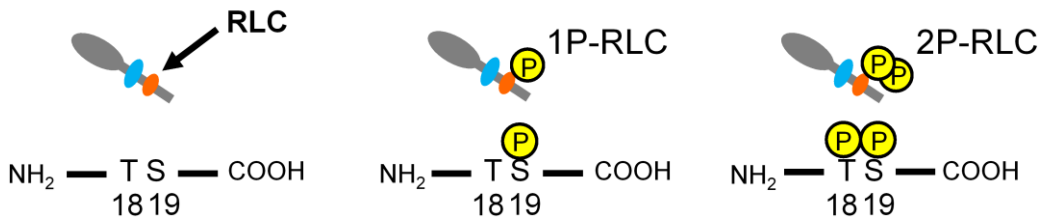

	dephosphorylation	monophosphorylation (1P)	diphosphorylation (2P)
ATPase activity	inactive	active	more active
filament stability	unstable	stable	more stable

Figure 3. Distinct phosphorylation level of RLC.

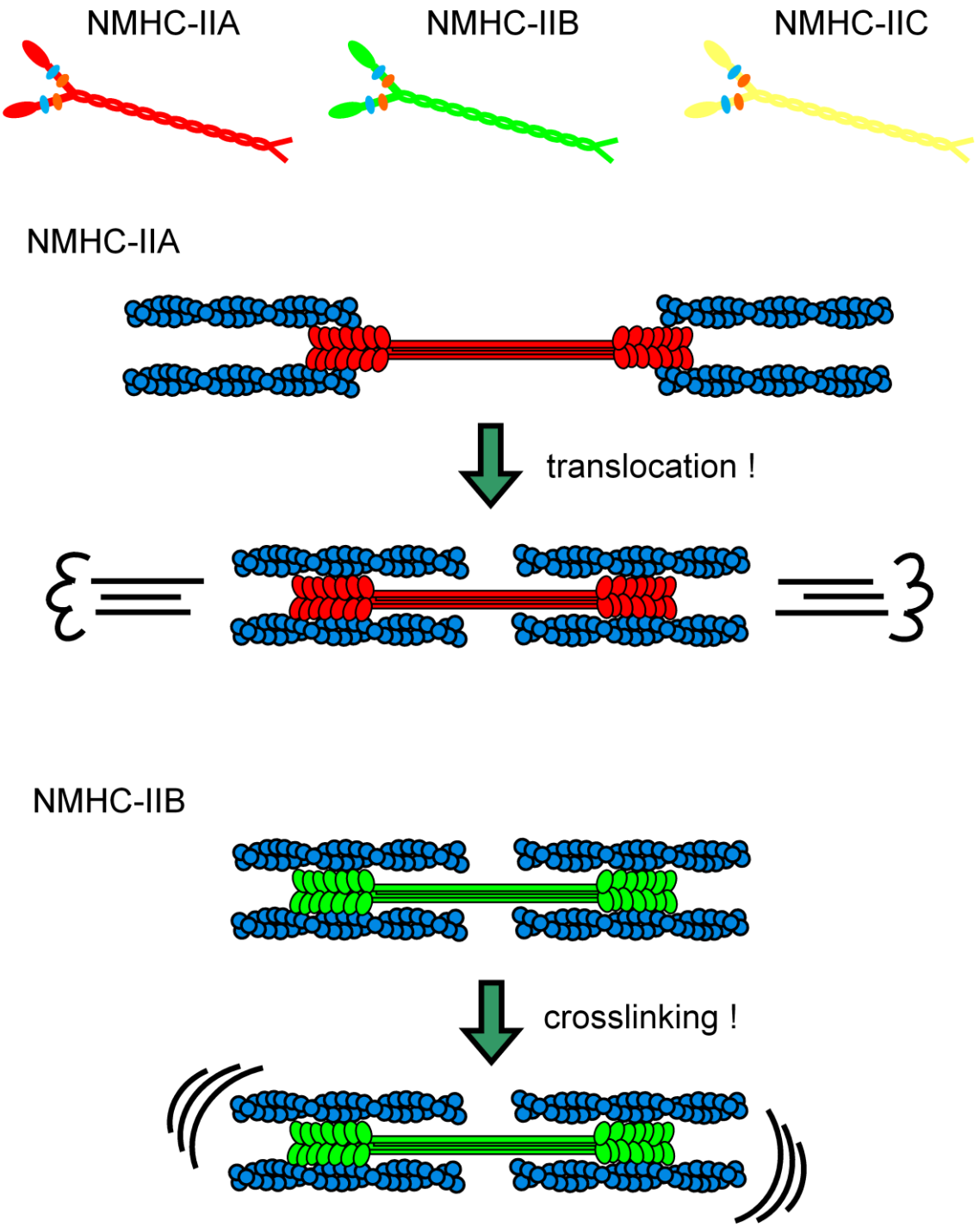

Figure 4. Properties of NMII isoforms.

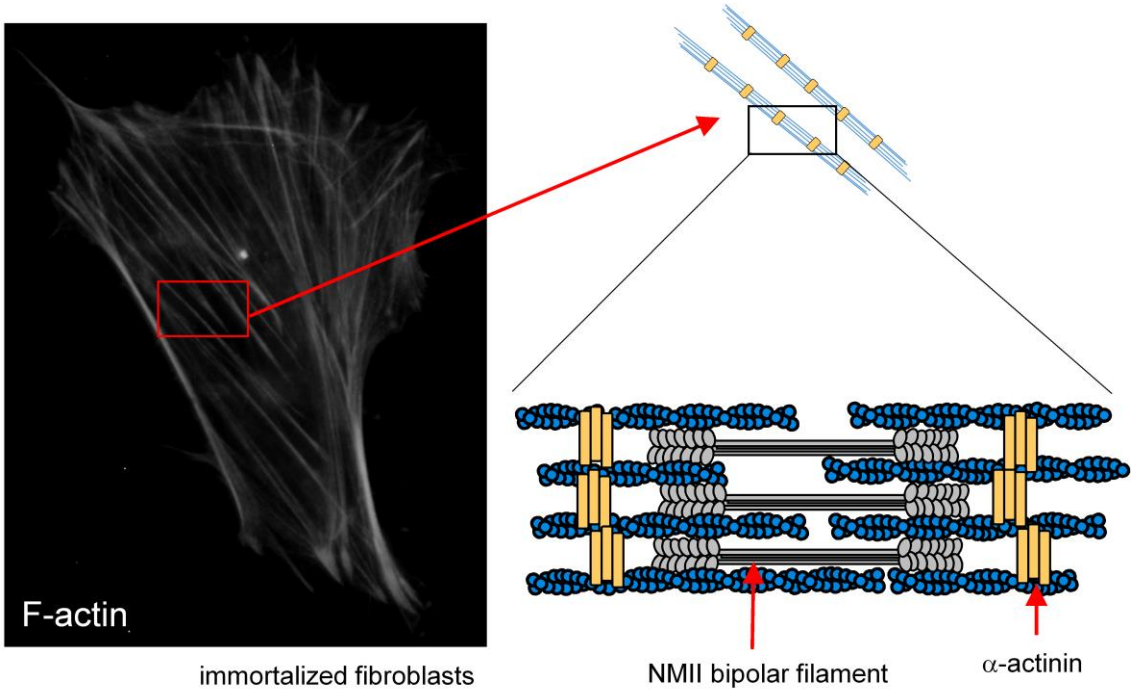

Figure 5. Structure of SFs.

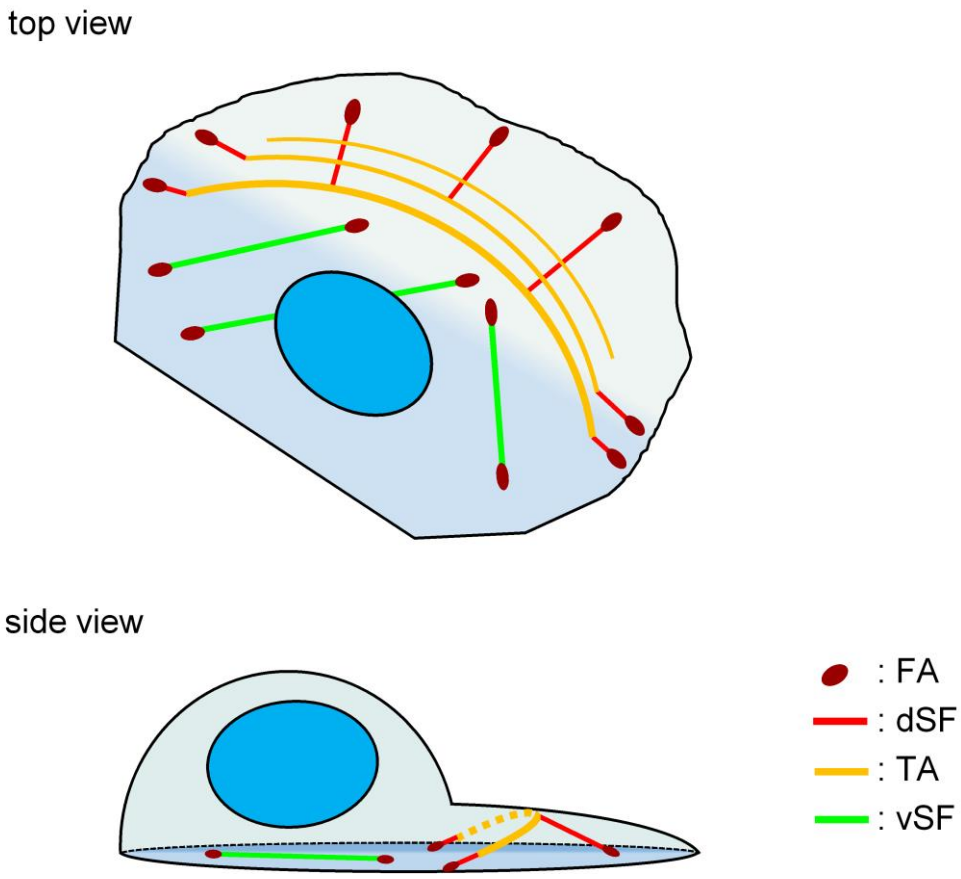

Figure 6. Three subtypes of SF.
Schematic representation of the SF subtypes in protrusive cells. In the side view, only one of each SF subtype is illustrated for simplification.

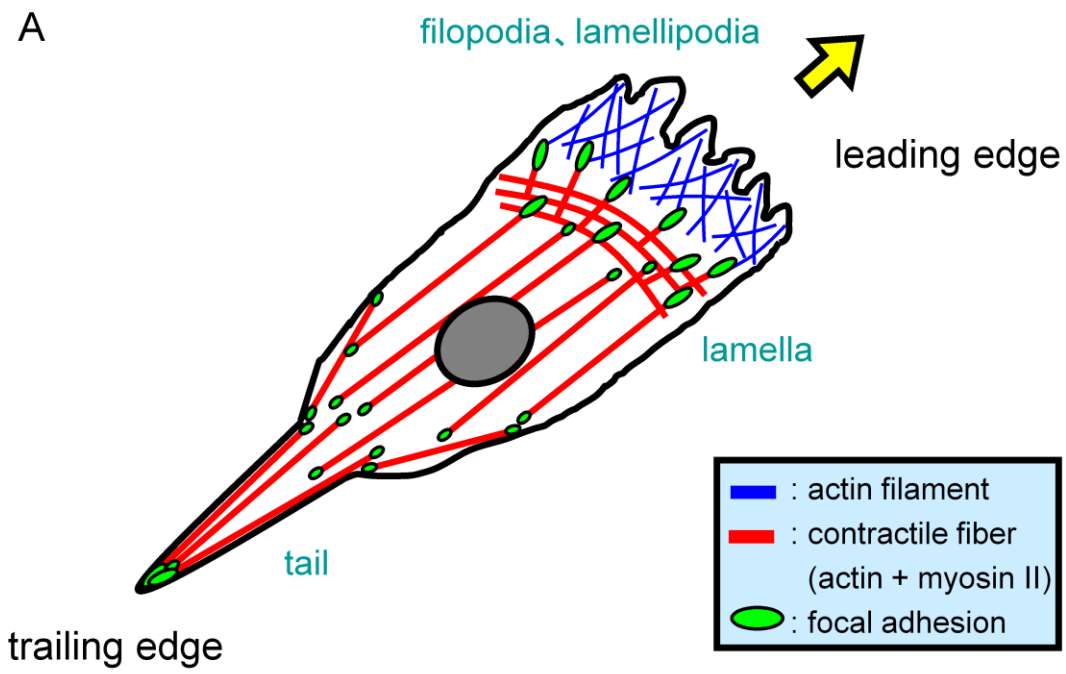

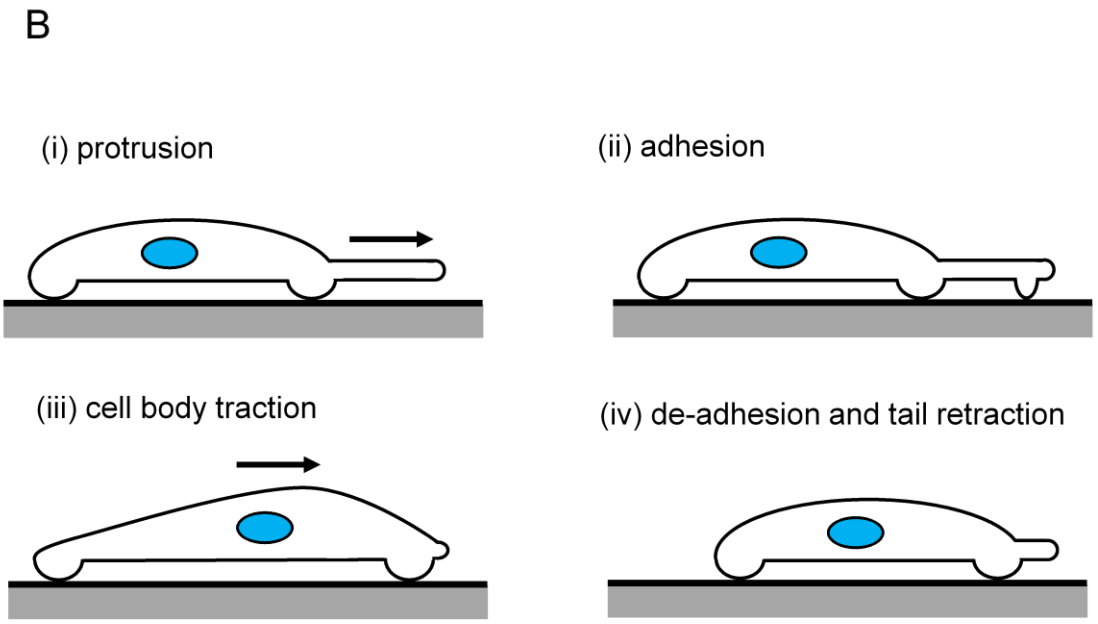

Figure 7. Model of migrating fibroblasts.

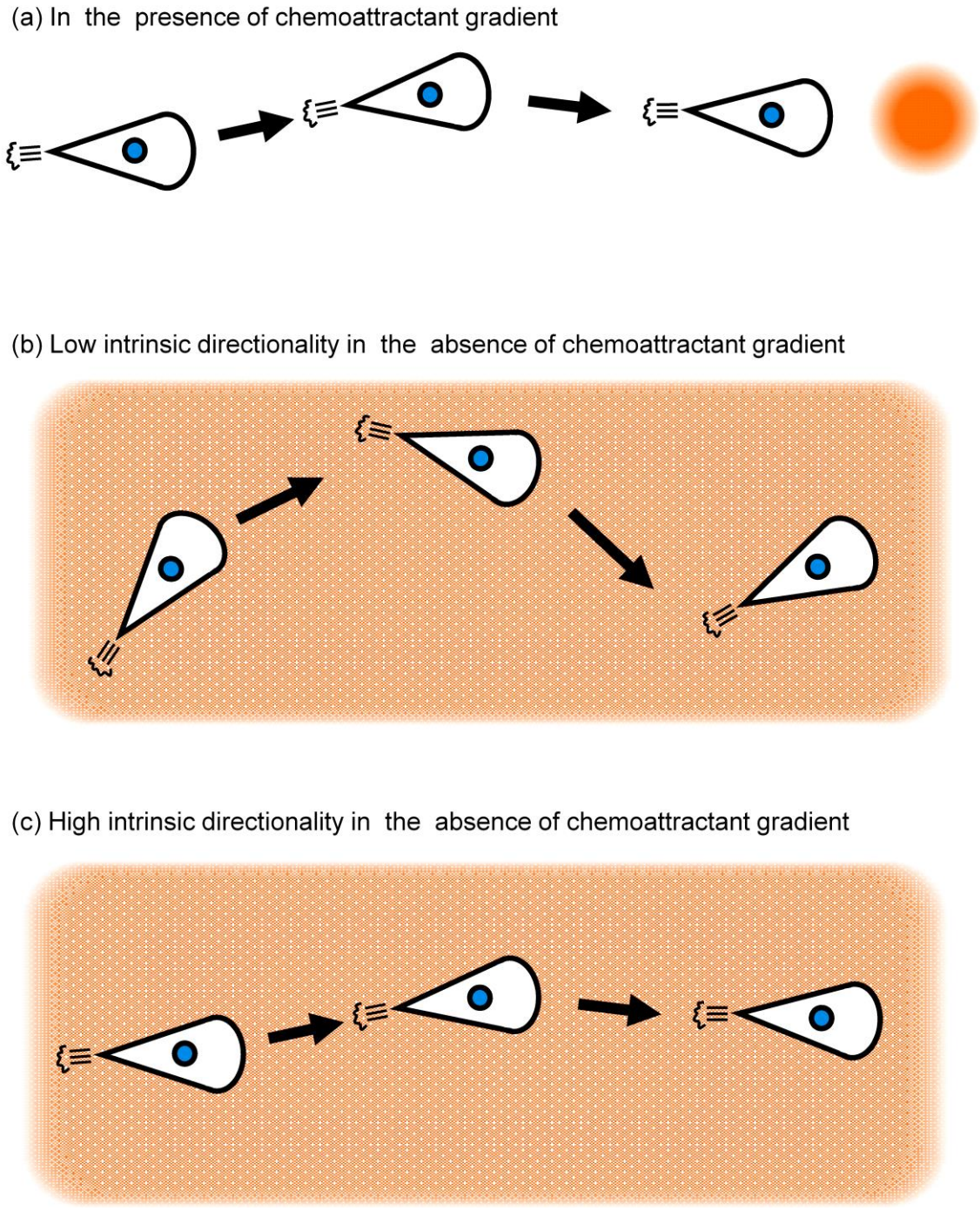

Figure 8. Mechanism of directional migration.

Materials and Methods

1: Cell culture

MRC-5 SV1 TG1 cells (SV40-transformant of human embryonic lung fibroblast MRC-5 cells; SV-1 cells) and MRC-5 cells (RCB0211) were obtained from the RIKEN Cell Bank (Tsukuba, Japan). TIG-1 cells (JCRB0501, TIG-1-20; human embryonic lung fibroblast), WI-38 cells (IFO50068), COS-7 cells (IFO50075), and HeLa cells (JCRB9004) were obtained from the Health Science Research Resources Bank (Osaka, Japan). U-2 OS cells were kind gifts from Dr. Keiju Kamijo (Tohoku Medical and Pharmaceutical University, Sendai, Japan). SV1, MRC-5, TIG-1, and WI-38 cells were maintained in MEM alpha (GIBCO/Life Technologies, Carlsbad, CA, USA). COS-7 cells were maintained in DMEM (Dulbecco's modified Eagle's medium) (GIBCO/Life Technologies). U-2 OS cells were maintained in McCoy's medium (GIBCO/Life Technologies). All culture media were supplemented with 10% fetal bovine serum (FBS), 50 U/mL penicillin, and 50 μg/mL streptomycin (GIBCO/Life Technologies). Cells were cultured at 37°C in humidified air containing 5% CO_2.

2: Antibodies and reagents

An anti-vinculin monoclonal antibody (hVIN-1) and fluorescein isothiocyanate (FITC) - and tetramethylrhodamine (TRITC) -conjugated phalloidin were purchased from Sigma-Aldrich (St. Louis, MO, USA). Anti-NMHC-IIB and anti-NMHC-IIA polyclonal antibodies targeting the carboxyl terminus of NMHC-IIB and NMHC-IIA, respectively, were used as previously described [9,56]. An anti-1P-RLC monoclonal antibody was prepared from hybridoma cells gifted by Drs. Yasuharu Sasaki (Kitasato University, Tokyo, Japan), Hiroshi Hosoya (Hiroshima University, Higashihiroshima, Japan), and Keiju Kamijo (Tohoku Medical and Pharmaceutical University). An anti-2P-RLC polyclonal antibody was purchased from Cell Signaling Technology (Danvers, MA, USA). Alexa Fluor 350-labeled phalloidin was purchased from Molecular Probes (Eugene, OR, USA). Cy3- and FITC-conjugated anti-rabbit IgG (H+L), FITC-conjugated anti-mouse IgG (H+L) were purchased from Jackson ImmunoResearch Laboratories (West Grove, PA, USA). Anti-GFP rabbit polyclonal serum (A6455) was purchased from Molecular Probes. An anti-α-tubulin monoclonal antibody (B-5-1-2) and 4',6-diamidino-2-phenylindole (DAPI) were purchased from Sigma-Aldrich. An anti-GAPDH monoclonal antibody (6C5) was purchased from EMD Millipore (Billerica, MA, USA). An anti-α-actinin polyclonal antibody (HPA006035) was a kind gift from Dr. Keiju Kamijo. The anti-RLC polyclonal antibody, MLC-2 (FL-172) was purchased from Santa Cruz Biotechnology (Santa Cruz, CA, USA). Horseradish peroxidase-labeled anti-rabbit and anti-mouse IgGs were purchased from Bio-Rad Laboratories (Hercules, CA, USA). Blebbistatin (BBS) was purchased from EMD Millipore Calbiochem (Billerica, MA,

USA). Fibronectin purified from human plasma was purchased from Roche Diagnostics (Basel, Switzerland).

3: Plasmids

penhanced green fluorescent protein (EGFP)-C1 was purchased from Takara Bio USA (formerly Clontech Laboratories, Mountain View, CA, USA). pEGFP-vinculin (plasmid no. 50513) was purchased from Addgene (Cambridge, MA, USA). pEGFP-NMHC-IIB [33] was a kind gift from Dr. Robert S. Adelstein (National Institutes of Health, Bethesda, MD, USA). pmCherry-NMHC-IIA was prepared as previously described [57]. pEGFP-NMHC-IIA* and pEGFP-NMHC-IIB* encoding the siRNA-insensitive form of NMHC-IIA and NMHC-IIB were generated using a two-step process, as follows: First, the fragments obtained by restriction digestion of pEGFP-NMHC-IIA with EcoRI-SalI and pEGFP-NMHC-IIB with EcoRI were subcloned into the pBluescript II SK^{+} (Stratagene, La Jolla, CA, USA). The fragments of NMHC-IIA and NMHC-IIB with siRNA insensitive mutation were generated by inverse PCR using pBluescript II SK^{+} containing the respective fragments as templates and primers listed in Table S1, respectively. Next these plasmids containing the siRNA insensitive sequences were digested with EcoRI-SalI and EcoRI, and the digestion products were subcloned into the same sites of pEGFP-NMHC-IIA-wild type (WT) and pEGFP-NMHC-IIB-WT, respectively. pmCherry-actin, pEGFP-tubulin, and pmCherry-tubulin were a kind gift from Dr. Keiju Kamijo. pmCherry-nuclear localization signal (NLS) was a kind gift from Dr. Toshiaki Imagawa (Hokkaido University, Sapporo, Japan). The chimeric pEGFP-NMHC-IIA/IIB-tail and pEGFP-NMHC-IIB/IIA-tail were constructed using a QuikChange II XL Site-Directed Mutagenesis Kit (Stratagene) according to the manufacturer's protocol as described previously [56]. In brief, first PCRs were performed using pEGFP-ARF296 or pEGFP-BRF305 as templates and the appropriate mutagenic primer sets described in Table S1. The mutagenic primers were designed to anneal cDNA of one isoform with additional sequence for another. Then second PCRs were performed using the products from the first PCR as megaprimers and either pEGFP-ARF296 NMHC-IIA or pEGFP-NMHC-IIB as a template for an inverse PCR following the QuikChange protocol [56]. pEGFP-NMHC-IIB*/IIA*-tail, which encodes the siRNA-insensitive form of NMHC-IIB/IIA-tail, was constructed as follows. First, the fragment obtained by restriction digestion of pEGFP-NMHC-IIB/IIA-tail with EcoRI-SacII was subcloned into the pBluescript II SK^{+} (Stratagene). Fragments of NMHC-IIB/IIA-tail with a siRNA-insensitive mutation of NMHC-IIA were generated by inverse PCR using pBluescript II SK^{+}. The primer sequences were listed in Table S1. Second, the plasmid containing the siRNA-insensitive NMHC-IIA sequence was digested with XmaI-SacII, and the digestion product was subcloned into the same sites of pEGFP-NMHC-IIB/IIA-tail to generate pEGFP-NMHC-IIB/IIA*-tail. Third, pEGFP-NMHC-IIB* was digested with EcoRI, and the digestion product

containing the siRNA-insensitive NMHC-IIB sequence was subcloned into the same sites of pEGFP-NMHC-IIB/IIA*-tail to generate pEGFP-NMHC-IIB*/IIA*-tail. The regions encoding S1, which contained the motor domain and the lever arm, of NMHC-IIB and NMHC-IIA were amplified from pEGFP-NMHC-IIB and pEGFP-NMHC-IIA as templates by PCR using the primer pairs listed in Table S1, respectively. The PCR products encoding NMIIB-S1 and NMIIA-S1 were subcloned into the BglII-KpnI and HindIII-KpnI sites of pEGFP-N3 (Takara Bio USA) to generate pNMIIB-S1-EGFP and pNMIIA-S1-EGFP, respectively. The plasmids encoding NMIIB-S1 and NMIIA-S1 point mutants were generated by inverse PCR using pNMIIB-S1-EGFP and pNMIIA-S1-EGFP as templates, respectively. pNMIIB*-S1-R709C-EGFP encoding the siRNA-insensitive form of NMIIB-S1-R709C was generated by inverse PCR using pNMIIB-S1-R709C-EGFP as a template and primers listed in Table S1. The nucleotide sequences of the DNA fragments amplified by PCR were verified by sequencing using an ABI PRISM 310 DNA sequencer (Applied Biosystems, USA).

4: Immunofluorescence

Cells were fixed with 3.7% formaldehyde prepared in phosphate-buffered saline (PBS) for 15 min and permeabilized with 0.1% Triton X-100 prepared in PBS for 10 min. Fixed cells were pre-incubated with blocking solution (3% bovine serum albumin prepared in PBS) for 30 min. Thereafter, cells were incubated with primary antibodies diluted in blocking solution for 60 min, washed with three times with PBS, incubated with the appropriate secondary antibodies diluted in blocking solution for 60 min, and subsequently washed three times with PBS. To stain actin filaments, Alexa Fluor 350-, FITC-, or TRITC-conjugated phalloidin (0.5 μg/mL) was added to the secondary antibody solution. The antibodies used for indirect immunofluorescence were as follows: anti-vinculin monoclonal antibody (1:5,000), anti-1P-RLC monoclonal antibody (1:200), anti-2P-RLC polyclonal antibody (1:200), Cy3-conjugated goat anti-rabbit IgG (H+L) (1:500), Cy3-conjugated goat anti-mouse IgG (H+L) (1:500), FITC-conjugated goat anti-rabbit IgG (H+L) (1:200), FITC-conjugated goat anti-mouse IgG (H+L) (1:200). For direct immunofluorescence, the antibodies were labeled with Alexa Fluor 488 or Alexa Fluor 596 using the Zenon Antibody Labeling Kit (Molecular Probes), according to the manufacturer's protocol. To simultaneously stain NMHC-IIB and NMHC-IIA, samples were incubated with Alexa Fluor 596-conjugated anti-NMHC-IIA (1:2,000) and Alexa Fluor 488-conjugated anti-NMHC-IIB (1:2,000) antibodies for 60 min. Thereafter, cells were fixed with 3.7% formaldehyde prepared in PBS for 15 min and incubated with Alexa Fluor 350-labeled phalloidin (0.5 μg/mL) for 60 min. Images were captured using a conventional fluorescence microscope (BX50WI; Olympus, Tokyo, Japan) equipped with a single-chip color charge coupled device (CCD) camera (DP70; Olympus) and an objective lens (UPlanApo 20×/0.70 NA; UPlanApo 60×/0.90 NA; UPlanFl 100×/1.30 NA

Oil; Olympus) together with DP Controller software (Olympus). All procedures were performed at room temperature. Immunofluorescence images were analyzed using ImageJ software (NIH, Bethesda, MD). The Fission yeast, *Schizosaccharomyces pombe,* was concentrated by centrifugation, washed in PBS, and stained with 1 μg/ml DAPI for 30 min at room temperature. Images were captured using a conventional fluorescence microscope (BX50WI; Olympus, Tokyo, Japan) equipped with a single-chip color CCD camera (DP70; Olympus) and an objective lens (UPlanApo 60×/0.90 NA; Olympus) together with DP Controller software (Olympus). Nucleus were counted using the analysis tool of the ImageJ software (NIH, Bethesda, MD).

5: Transfection

Cells were transfected with plasmid DNA using Xfect Transfection Reagent (Takara Bio USA) in FBS-free and antibiotic-free OPTI-MEM (GIBCO/Life Technologies) according to the manufacturer's protocol. Transfected cells were replated onto coverslips (Matsunami, Kishiwada, Japan) or glass-bottom dishes (IWAKI, ASAHI GLASS, Tokyo, Japan) precoated with 10 μg/mL fibronectin for immunofluorescence or time-lapse observation, respectively.

6: Time-lapse observation

Time-lapse images were captured with an inverted microscope (IX71; Olympus) equipped with a single-chip color CCD camera (DP70; Olympus) and an objective lens (LCPlanFl 20×/0.40 NA; UPlanApo 60×/0.90 NA; UPlanFl 100×/1.30 NA Oil; Olympus). During observation, the cells were maintained in DMEM/F12 (1:1) (GIBCO/Life Technologies) supplemented with 10% FBS and warmed on a thermoplate heated to 37°C (MATS-U55R30; Tokai Hit, Fujinomiya, Japan). Images were captured every 5 min and analyzed using DP Controller software (Olympus). Images of cells expressing mCherry-NMHC-IIA and EGFP-NMHC-IIB were captured using an inverted microscope (Ti-E; Nikon, Tokyo, Japan) equipped with an oil-immersion objective lens (Plan Apo-VC 60×/1.40 NA; Nikon). Cells were maintained in DMEM/F12 (1:1) (GIBCO/Life Technologies) supplemented with 10% FBS and were warmed in an incubation chamber heated to 37 °C (INUBG2H-TIZB; Tokai Hit) during observation. Images were captured and were analyzed using NIS-Elements C software (Nikon)

7: Confocal laser scanning microscopy

Live cell images were captured using an inverted microscope (Ti-E; Nikon, Tokyo, Japan) and a confocal laser microscope system (A1R; Nikon) equipped with an oil-immersion objective lens (Plan Apo VC 60×/1.40 NA Oil; Nikon). Cells were maintained in DMEM/F12 (1:1) (GIBCO/Life Technologies) supplemented with 10% FBS and warmed in a chamber set at 37°C (INUBG2H-TIZB; Tokai Hit) during observation. Z-stack images were oversampled by taking

230 nm z-steps between acquired images. Images were captured and analyzed using NIS-Elements C software (Nikon).

8: KD of NMHC-IIA and NMHC-IIB

Human NMHC-IIA-specific (GGCCAAAGAGAACGAGAAGUU), human NMHC-IIB-specific (GGAUCGCUACUAUUCAGGAUU), and nonsense (GCGCGCUUUGUAGGAUUCGUU) siRNAs were purchased from Thermo Scientific Dharmacon (Waltham, MA, USA). siRNAs were transfected using Lipofectamine RNAiMAX Transfection Reagent (Invitrogen, Carlsbad, CA, USA), according to the manufacturer's protocol. After transfection for 72 h, immunofluorescence or time-lapse observation was performed. To express exogenous proteins, the cells were transfected again with the respective expression vector at 24 h after siRNA transfection.

9: Cell stretching

A stretch device was constructed by using the universal plate set (No.98, TAMIYA, INC, Sizuoka, Japan) as a base board. The plate was equipped with a silicone soft mold (Plate G; Kameshima Co., Ltd., Osaka, Japan) as a cell culture chamber. One edge of the silicone chamber was fixed to an immobile bar attached to the plate, and the opposite edge was connected to a movable bar for stretching. Cells were plated on the silicon chamber precoated with 50 μg/mL fibronectin. During observation, the cells were maintained in DMEM/F12 (1:1) (GIBCO/Life Technologies) supplemented with 10% FBS at 25°C. Live cell images were captured using a conventional fluorescence microscope (BX50WI; Olympus) equipped with a single-chip color CCD camera (DP70; Olympus) and a water immersion objective lens (LUMPlanFl 60×/0.90 NA; Olympus).

10: Immunoprecipitation

Cells were lysed with lysis buffer (300 mM NaCl, 1 % IGEPAL CA-630, 20 mM Tris-HCl, pH 7.5, 1 mM DTT, 1 mM PMSF) supplemented with PhosSTOP and cOmplete, EDTA-free (Roche Diagnostics) were used as phosphatase and protease inhibitors, respectively. After centrifugation (22,000 × g) for 15 min at 4°C, anti-NMHC-IIA pAb, anti-NMHC-IIB pAb was added to the supernatant, which was followed by incubation for 30 min at 4°C. The immunocomplexes were captured by protein A Sepharose beads (GE Health-care) and then collected by centrifugation (1,000 × g) for 5 s. The beads were washed three times in a PBS. Then, beads were collected by centrifugation (10,000 × g) for 5 min. For SDS-polyacrylamide gel electrophoresis (PAGE), the immunoprecipitates were eluted in SDS lysis buffer with boiling for 3 min.

11: SDS-PAGE and immunoblotting

SDS-PAGEwas performed using standard techniques. For separation of phosphorylated RLC,

Mn^{2+}-Phos-tag SDS-PAGE was performed according to a previously described protocol [11]. The concentrations of Phos-tag acrylamide (NARD Institute, Amagasaki, Japan) and $MnCl_2$ in the gel were both 100 μM. Separated proteins were transferred to Immobilon-P membranes (EMD Millipore). The membranes were blocked with blocking buffer [5% skimmed milk and 0.05% Tween-20 in Tris-buffered saline (TBS)] for 30 min at 25°C. The membranes were incubated with primary antibodies overnight at 4°C, and then labeled with secondary antibodies for 60 min at 25°C. The following antibodies were diluted in blocking buffer as follows: anti-GFP rabbit polyclonal serum (1:10,000), anti-GAPDH monoclonal antibody (1:40,000), and appropriate secondary antibodies (1:10,000). Chemiluminescent signals were developed using Immobilon Western Chemiluminescent HRP Substrate (EMD Millipore) and detected using a LAS-3000 system (Fujifilm, Tokyo, Japan) and analyzed with MULTIGAUGE Version 2.2 software (Fujifilm).

12: Statistical analysis

All statistical analyses were performed with EZR (Saitama Medical Center, Jichi Medical University, Saitama, Japan), which is a graphical user interface for R (The R Foundation for Statistical Computing, Vienna, Austria). More precisely, it is a modified version of R commander designed to add statistical functions frequently used in biostatistics. The results are presented as standard deviation of the mean and number of experiments denoted as n. Values of $P < 0.05$ were considered statistically significant. For each box plot, the central line is the group median, the box edges are the 25th and 75th percentiles, and the whiskers extend to the 1.5 times interquartile range.

Table S1. Primers used for PCR mutagenesis

Construct		Primer
NMIIB-S1-WT	Forward	5'-agatctgccaccatggcgcagagaactggact-3'
	Reverse	5'-ggtacccttcacctttgtgaagactc-3'
NMIIB-S1-R709C	Forward	5'-agatcccttccaggacacc-3'
	Reverse	5'-ctatctgtcgccagggcttc-3'
NMIIB-S1-N97K	Forward	5'-ttcaagcatgtcaattctgc-3'
	Reverse	5'-ggaagcttccgttttacat-3'
NMIIB*-S1-R709C[a]	Forward	5'-ctatagtagcgatccttcaga-3'
	Reverse	5'-cggactaatctatacttattc-3'
EGFP-NMHC-IIA[b]	Forward	5'-attctccttggcctgggccag-3'
	Reverse	5'-gagaagaagctgaagagcatg-3'
EGFP-NMHC-IIB[c]	Forward	5'-ctatagtagcgatccttcaga-3'
	Reverse	5'-cggactaatctatacttattc-3'
EGFP-NMHC-IIA/IIB-tail	Forward	5'-gacacccgcgcctctcgtgaggagatc-tttgctcaatccaaagag-3'
	Reverse	5'-ggctgattatgatcagttatctagatccgg-3'
EGFP-NMHC-IIB/IIA-tail	Forward	5'-gaagctcgtgcatccagagatgagatt-**ctggcccaggccaaagag**-3'
	Reverse	5'- ggctgattatgatcagttatctagatccgg-3'

Letters with an underscore and boldface letters with an underscore indicate sequences annealing to pEGFP-BRF305 and pEGFP-ARF296 in first step PCR, respectively.

[a]siRNA-insensitive form of NMIIB-S1-R709C.

[b]siRNA-insensitive form of EGFP-NMHC-IIA.

[c]siRNA-insensitive form of EGFP-NMHC-IIB.

Chapter 1: Development of a novel tension probe using NMII head domain, S1

1-1: Abstract

Various experimental methods have been developed to measure cellular tension mediated by the actomyosin contractility. In general, cellular tension is measured by traction force microscopy (TFM) and FRET-based sensors. However, these methods cannot detect the tension level applying to SFs. In this chapter, I tried to develop a novel tension probe using the human nonmuscle myosin II head domain, S1. I assessed the localization of S1 mutants and their solubility using SV1 cells. Consequently, only NMIIB-S1-R709C displayed the clear localization in selected stress fibers and the contractile ring of dividing cell. These results suggest that NMIIB-S1-R709C, which spends most of time in the strong- binding state to actin filaments during ATPase cycle, can bind to SFs in the regions escalating tension by recognizing the stretched actin filaments. We propose NMIIB-S1-R709C is a novel tension probe.

1-2: Results

1-2-1: NMIIB-S1-R709C-EGFP is selected as a tension probe

It has been brought to attention that actin filaments undergo conformational changes to function as a tension sensor [58–61]. Uyeda *et al*. reported that the myosin II motor domain, S1 can bind to actin filaments localizing in stretched regions of *Dictyostelium discoideum* cells [58]. Further, Tang and Ostap reported that S1 of NMIIB can bind to selected SFs in mammalian cells [62]. These reports prompted me to investigate stretch-induced conformational differences of actin filaments in each SF subtype by examining NMII-S1 binding. In *Dictyostelium* cells, S1 mutants with a high affinity for actin filaments bind to stretched actin filaments in the presence of physiological ATP concentrations [58]. Thus, I examined the cellular localization of several S1 mutants of human NMII to identify the best probe for actin filaments in selected SFs. The R702C and N93K mutations in human NMHC-IIA, which are associated with certain genetic disorders, inhibit actin-activated Mg^{2+}-ATPase activity and actin filaments translocation *in vitro* [63]. R709C and N97K in human NMHC-IIB are artificial mutationss that correspond to R702C and N93K in NMHC-IIA, respectively [64]. I prepared S1-EGFP constructs containing one of these mutations, in addition to the wild type, and performed live cell imaging of S1-EGFP expressing cells to avoid possible artifacts caused by fixation and permeabilization during immunofluorescence staining (Figure 9). None of the NMIIA-S1 constructs localized to SFs. Among the NMIIB-S1 constructs, NMIIB-S1-WT-EGFP slightly localized to specific SFs and NMIIB-S1-R709C-EGFP clearly localized there. The organization of SF subtypes was not affected by expression of NMIIB-S1-R709C-EGFP. Thus, this mutant is not likely to prevent the binding of endogenous NMII to actin filaments. NMIIB-S1-R709C-EGFP did not localize to

regions in which SFs were lost by treatment with BBS or Y-27632 (Figure 10). Then I assessed the ability of the NMIIB-S1-R709C-EGFP to associate with the actin cytoskeleton in the cell, using a Triton X-100 solubility assay, in which S1 associated with the actin cytoskeleton separates into the insoluble fraction, and S1 diffused into the cytoplasm separates into the soluble fraction. NMIIB-S1-R709C-EGFP remained bound to Triton-insoluble fraction (Figure 11). NMIIB-R709C heavy meromyosin (HMM; a soluble fragment consisting of two heads and a part of the rod) displays very slow ADP release, indicating that it spends in a strong actin-binding state predominantly during the ATPase cycle [64]. This inherent property of the R709C mutant might be useful to detect distinct SFs with a higher affinity for the motor domain of NMIIB.

1-2-2: NMIIB-S1-R709C-EGFP can be used as a probe for stretched actin filaments

Next, I performed cell stretch experiments by using a stretch device to test whether NMIIB-S1-R709C can recognize a specific conformational feature of stretched actin filaments in mammalian cells. I measured the fluorescence intensities of NMIIB-S1-R709C-EGFP in SFs before and after stretching and normalized it with respect to that of mCherry-actin. Figure 12A shows the SV1 cells expressing NMIIB-S1-R709C-EGFP and mCherry-actin before and after 14% stretching. Cell stretching increased the relative fluorescence intensity of EGFP, indicating that it promoted binding of NMIIB-S1-R709C to the SFs was promoted by stretching (Figure 12, B and C). These results suggest that NMIIB-S1-R709C can recognize a conformational change of actin filaments and preferentially binds to the stretched actin filaments. Therefore, I selected NMIIB-S1-R709C-EGFP as the probe for stretched actin filaments in actin cytoskeletons. Concerning the study of properties of actin cytoskeletons using this probe, I described in Chapter 2 and Chapter 3 of this dissertation.

1-2-3: NMIIB-S1-R709C-EGFP can detect actin filaments in a contractile ring

To elucidate whether NMIIB-S1-R709C is localized in the other contractile structure containing stretched actin filaments such as a contractile ring [58,65], we examined localization of NMIIB-S1-R709C in the contractile ring of SV1 cell. NMIIB-S1-R709C-EGFP showed accumulation to the cleavage furrow from the onset of anaphase (Figure 13A). During telophase, NMIIB-S1-R709C-EGFP was strongly localized in the contractile ring and exhibited a tube-like structure (Figure 13B). This tube-like structure was separated at the center of the midbody in the final stage of cytokinesis. The other S1 constructs mentioned above were not localized in the contractile ring (data not shown). These results indicate NMIIB-S1-R709C-EGFP can recognize the stretched actin filaments of contractile ring, confirming the usefulness of NMIIB-S1-R709C-EGFP as a tension probe.

1-3: Discussion

In general, cellular tension is measured by TFM, a method to determine the traction force by observing the displacement of the elastic culture substrate fabricated pillar arrays [66] or fluorescent beads embedded in gel [67,68]. FRET-based probe to detect conformational change of vinculin in focal adhesion was also reported [69]. However, these techniques cannot visualize and judge the level of tension applied to the cytoskeletal structure itself. In this chapter, I demonstrated that NMIIB-S1-R709C was localized in selected SFs and the contractile ring by the observation of living cells. In addition, I assessed that the solubility of NMIIB-S1 R709C using Triton X-100 solubility assay and revealed that this S1 mutant to associate with the actin cytoskeleton. Then, the binding of NMIIB-S1 R709C to SFs was increased after 14% stretching. These results indicate NMIIB-S1-R709C recognizes and preferentially associates the stretched actin cytoskeleton in human fibroblast cells (Figure 14).

Distinct motor properties of NMIIA and NMIIB were revealed by *in vitro* studies [16–19]. NMIIB exhibits slower ADP release and higher ADP affinity, resulting in a higher duty ratio than NMIA. Further, the ADP release rate of both isoforms, especially NMIIB, is decreased by the resisting load, suggesting that NMIIB has a role to maintain tension [16,19]. Therefore, NMIIB-S1 is likely to be more suitable for visualization of actin-filament than NMIIA-S1 in the living cells.

Mutations, N93K and R702C in human NMHC-IIA, display distinct kinetic properties [63]. N93K mutation of NMIIA-HMM displays very slow Pi release and it cannot translocate actin filaments *in vitro*. The equivalent mutant, N97K of NMIIB is likely to have similar kinetic properties with N93K of NMIIA. The steady-state intermediate of N97K of NMIIB-HMM during ATPase cycle is thought to be in the weak-binding state to actin filaments [64]. I demonstrated that NMIIA-S1-N93K and NMIIB-S1-N97K were not localized to any SFs. Particularly NMIIB-S1-N97K was excluded from SFs (Figure 9). The intermediate species of these S1 constructs are likely to be insufficient to associate with actin filaments in living cells. On the other hand, R709C mutant of NMIIB-HMM exhibits very slow ADP release so that it spends most of time in the strong-binding state to actin filaments during ATPase cycle [64]. This mutation reduces actin-activated Mg^{2+}-ATPase activity and actin filament translocation speed *in vitro*. The intermediate species of NMIIB-S1-R709C in the strong-binding state could be required for the association with actin filaments in living cells.

Uyeda *et al*. proposed a three-component positive feedback loop in *Dictyostelium* cells [58]. This positive feedback loop consists of (1) stretch-induced conformational change of actin filaments, (2) binding of the NMII filaments to stretched actin filaments, and (3) NMII-dependent tension generation. As shown in Figure 12, we demonstrated that the stretching of cells promotes the binding of NMIIB-S1-R709C in SFs. There could be a similar positive feedback loop in SFs

of fibroblasts. Binding of NMIIB-S1-R709C to stretched actin filaments was evaluated by assessing fluorescence intensity of the EGFP fused to the C-terminus after normalization against that of mCherry-actin; therefore, the increase in the binding of this probe was not due to the increase in the density of actin filaments in SFs. Certain actin-filament-binding proteins, such as tropomyosin isoforms, can bind to different SF subtypes in an isoform-dependent manner [70–72]. Although we cannot exclude the possibility that binding of these proteins mediates the preferential binding of the NMIIB-S1-R709C-EGFP (hereafter referred to as the S1 probe) to stretched actin filaments, we conclude that S1 probe can recognize certain qualitative changes of stretched actin filaments in loaded SFs.

1-4: Conclusion

In this chapter, I demonstrated that the S1 probe was localized in the stretched SFs and the contractile ring in living fibroblasts. The S1 probe would be a valuable tool to directly distinguish stretched SFs in mechanobiology studies. In the future, it is desirable to improve the probe by further modification of NMIIB-S1-R709C, for example, mutants in which Arg at position 709 replacing with other amino acids besides Cys. Furthermore, the probes based on two-headed HMM could be effective.

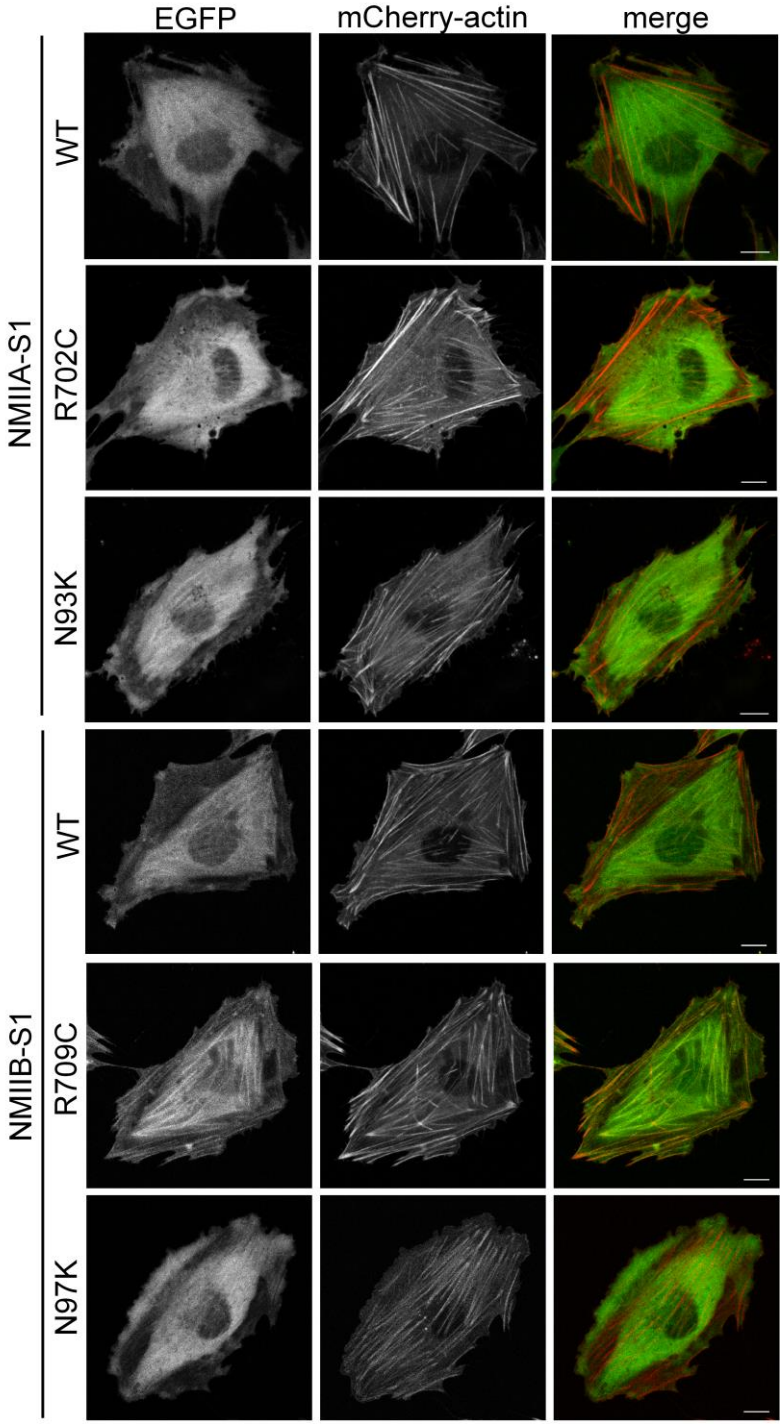

Figure 9. Localization of the NMII-S1-EGFP mutants.
Localization of NMIIA-S1-EGFP constructs (WT, R702C and N93K) and NMIIB-S1-EGFP constructs (WT, R709C and N97K) in SV1 cells. The indicated NMII-S1-EGFP constructs were expressed with mCherry-actin. Live cell images were captured with a confocal microscope. Bar, 10 μm.

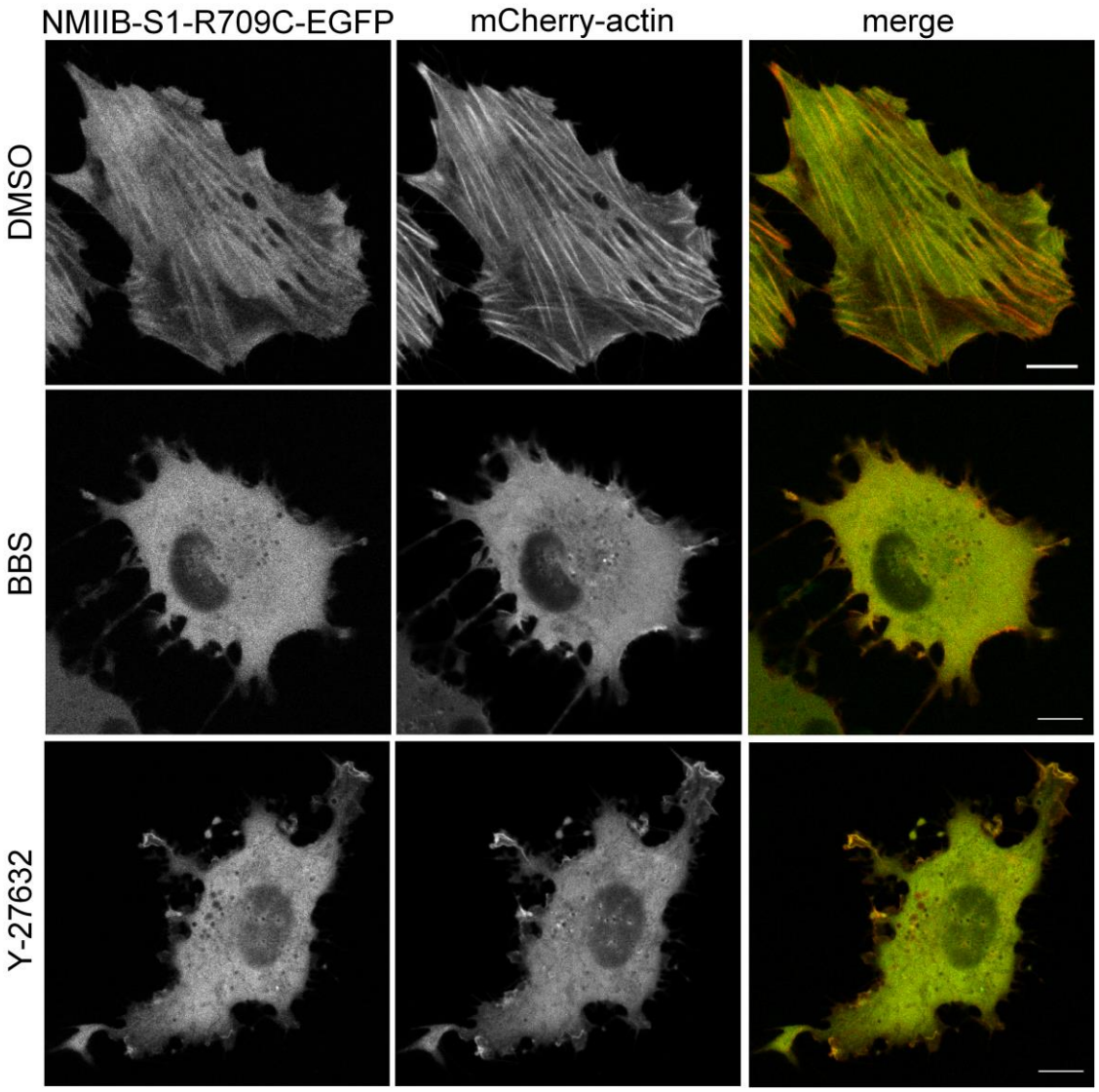

Figure 10. Effects of BBS and Y-27632 on the localization of NMIIB-S1-R709C-EGFP in SV1 cells
SV1 cells expressing NMIIB-S1-R709C-EGFP and mCherry-actin were treated with 0.1% DMSO, 50 μM BBS, or 20 μM Y-27632 for 60 min. Live cell images were captured with a confocal microscope. Bar, 10 μm.

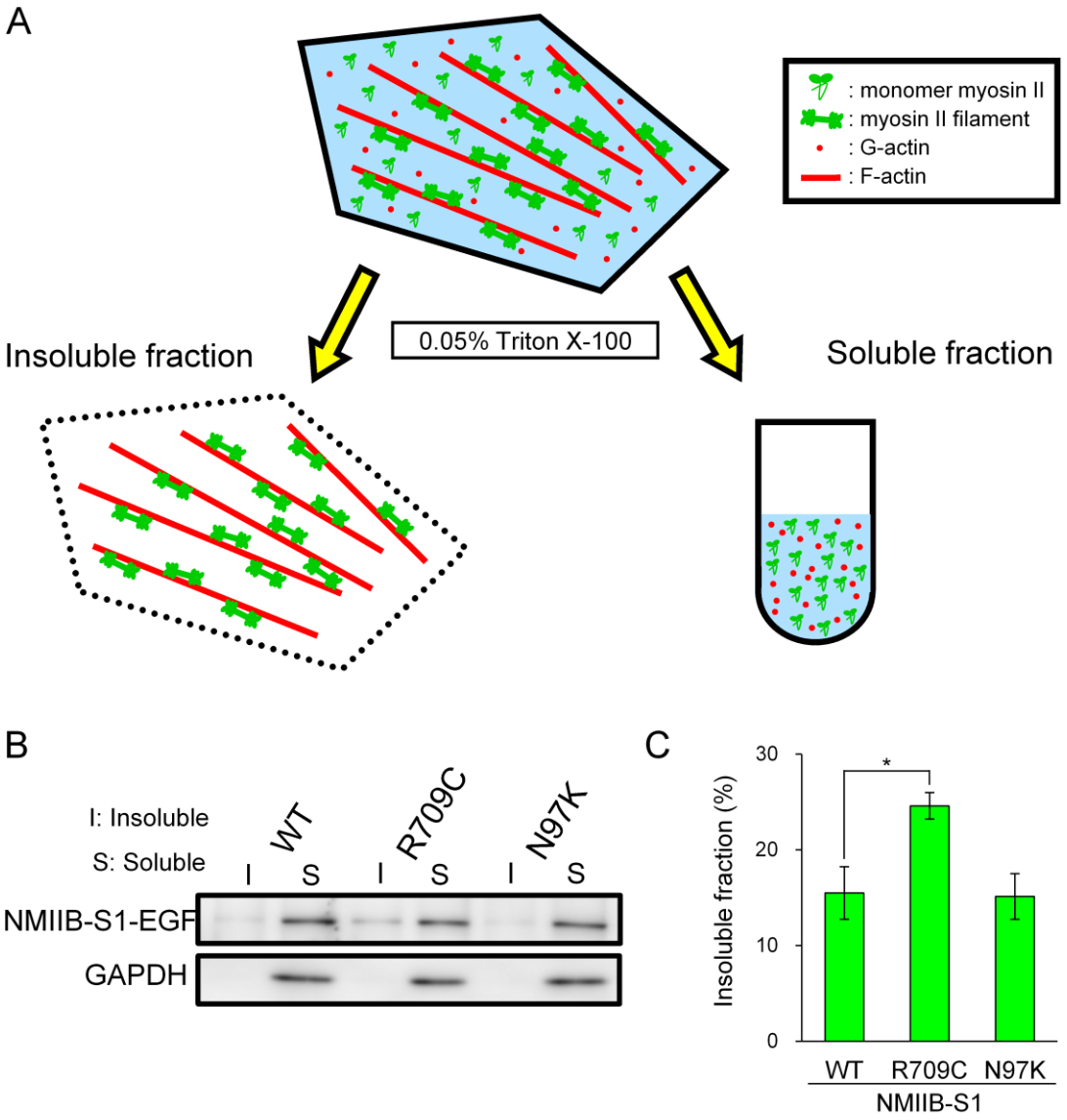

Figure 11. Properties of the NMIIB-S1-EGFP probes.
(A) Diagram of Triton-100 solubility assay. The cells were treated with extraction buffer containing 0.05% Triton X-100. Under this condition, cytoskeletal proteins are not extracted. As a result, the cytoplasmic soluble fraction and cytoskeletal fraction is able to be separated. (B) Immunoblots of insoluble (I) and soluble (S) fractions of SV1 cells expressing the indicated NMIIB-S1-EGFP constructs in the Triton X-100 solubility assay. The blots were probed with an anti-GFP (top) or anti-GAPDH (bottom) antibody. (C) The percentage of NMIIB-S1-EGFP remained to the insoluble fraction. Data represent the mean ± SD from three independent experiments. *$P < 0.05$.

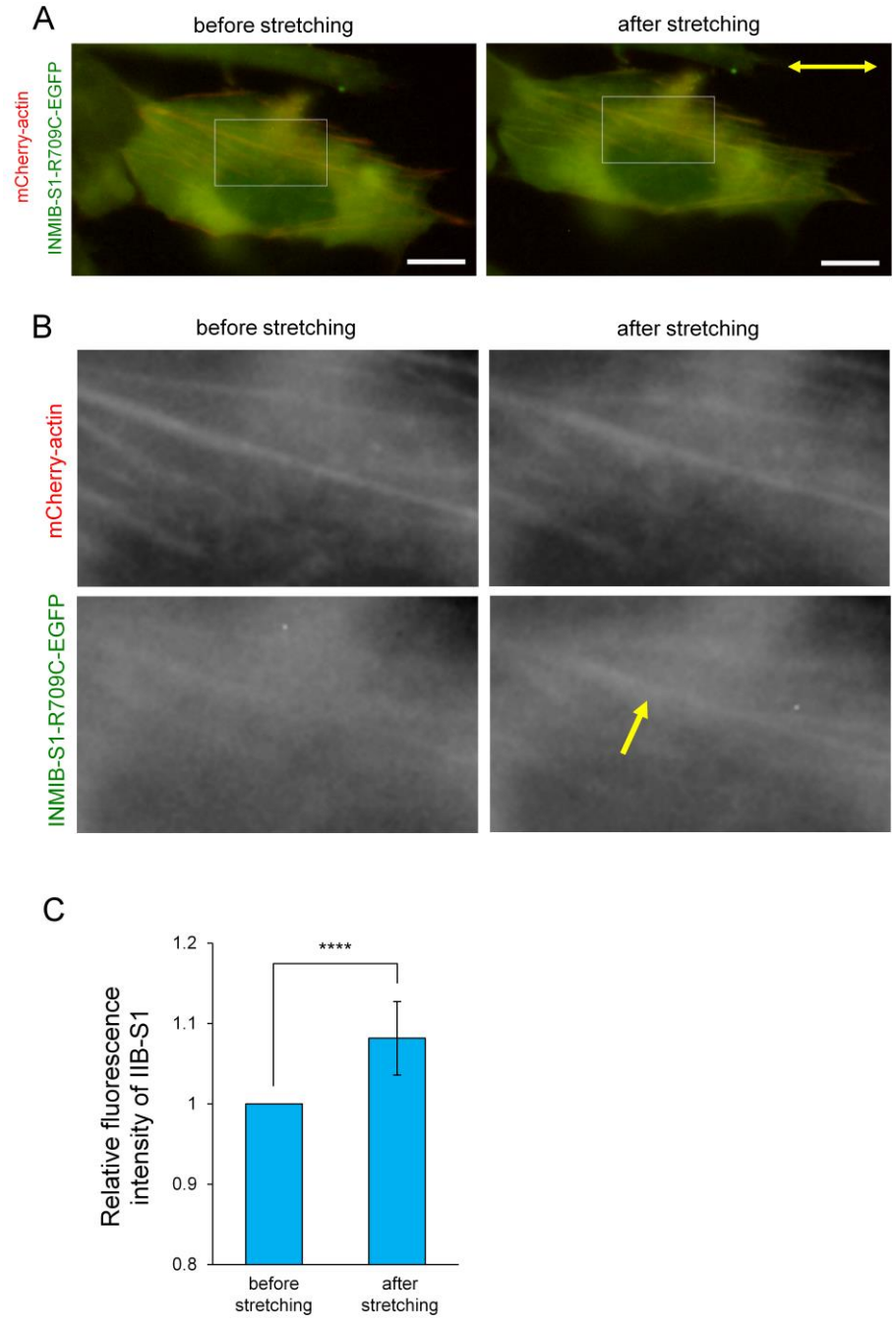

Figure 12. NMIIB-S1-R709C-EGFP can be used as a probe for stretched actin filaments.
(A) Images of live SV1 cell expressing NMIIB-S1-R709C-EGFP and mCherry-actin before and after stretching. The silicone chamber was stretched by 14% in the direction indicated by the two-way arrow. (B) Enlarged images of the boxed regions in panel A showing some SFs. The yellow arrow indicates a representative SF in which the fluorescence intensity of NMIIB-S1-R709C-EGFP was increased after stretching. (C) Fluorescence intensities of NMIIB-S1-R709C-EGFP in the control and SF areas were quantified using the RGB Measure plugin of ImageJ software. The relative fluorescence intensity of NMIIB-S1-R709C-EGFP in the SF area versus the control area was calculated for each image and normalized by that of mCherry-actin. Data represent the mean ± SD from nine independent experiments. ****$P < 0.00005$.

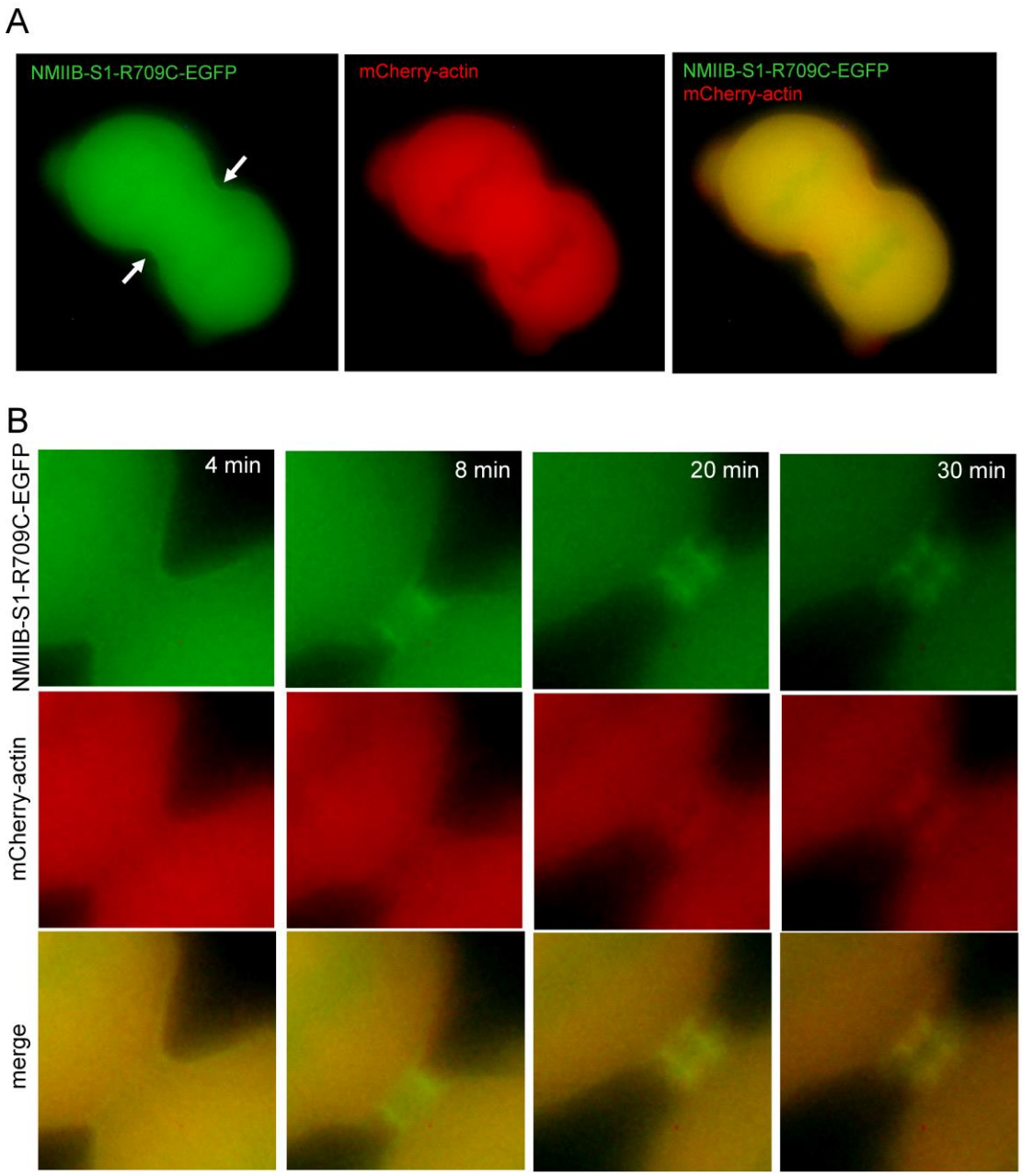

Figure 13. Dynamics of NMIIB-S1-R709C-EGFP in diving SV1 cell. (A) Images of cytokinesis of live SV1 cell. White arrows indicate the accumulation of NMIIB-S1-R709C in the cleavage furrow. (B) Time series of images showing the dynamics of NMIIB-S1-R709C in the contractile ring. Note that NMIIB-S1-R709C formed tube-like structure from 8min to 20 min.

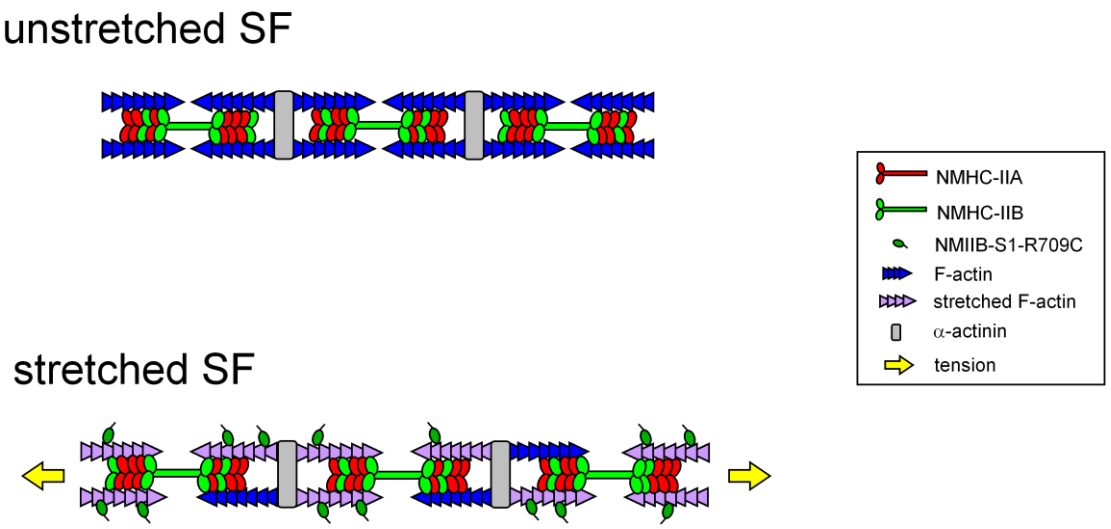

Figure 14. Model of association with S1 and stretched actin filaments
NMIIB-S1-R709C recognized state of actin filaments and preferentially associates tension-increased region.

Chapter 2: Distinct functions of NMIIA and NMIIB in organization of SF subtypes

2-1: Abstract

SFs are contractile, force-generating bundled structures that can be classified into three subtypes, namely, ventral SFs (vSFs), transverse arcs (TAs), and dorsal SFs. NMII is the main component of SFs. This study examined the roles of the NMII isoforms NMIIA and NMIIB in the organization of each SF subtype in immortalized fibroblasts. KD of NMIIA (a major isoform) resulted in loss of TAs from the lamella and caused the lamella to lose its flattened shape. Exogenous expression of NMIIB rescued this defect in TA formation. However, the TAs that formed upon exogenous NMIIB expression in NMIIA-KD cells and the remaining TAs in NMIIB-KD cells, which mainly consisted of NMIIB and NMIIA, respectively, failed to rescue the defect in lamellar flattening. These results indicate that both isoforms are required for the proper function of TAs in lamellar flattening. KD of NMIIB resulted in loss of vSFs from the central region of the cell body, and this defect was not rescued by exogenous expression of NMIIA, indicating that NMIIA cannot replace the function of NMIIB in vSF formation. Moreover, we raised the possibility that actin filaments in vSFs are in a stretched conformation.

2-2: Results

2-2-1: Dynamics of each SF subtype in SV1 cells

To investigate the involvement of NMIIA and NMIIB in the organization of SF subtypes, we used SV1 cells because they contain each SF subtype as described below (Figure 15A). The level of NMHC-IIC was below the detection limit of immunoblotting in this cell line (data not shown). In addition, SV1 cells migrate very slowly, which allows cytoskeletal dynamics to be easily studied via time-lapse observation. Immunofluorescence revealed that vSFs, TAs, and dSFs were present in SV1 cells (Figure 15B). We next analyzed the dynamics of each SF subtype in SV1 cells expressing mCherry-actin and EGFP-vinculin (Figure 15C). TAs exhibited dynamic centripetal flow in lamellae, whereas vSFs were less mobile in cell bodies (Figure 15D). As demonstrated by Heath [27], TAs disappeared from regions near the proximal end of lamellae (Figure 16). Based on these results, we confirmed the presence of all three SF subtypes and their dynamic properties in SV1 cells.

2-2-2. NMIIA and NMIIB localize to SF subtypes differently

Next, I visualized endogenous NMIIA and NMIIB in the three SF subtypes and demonstrated NMIIA localized to SFs throughout cells, whereas NMIIB was excluded from the peripheral region of cells (Figure 17A). The localization patterns of NMIIA and NMIIB in SV1 cells were

similar to those observed in other cells [9,20,52,54,73,74]. Focusing on the lamellar region, NMIIA localized in all TAs as puncta, whereas NMIIB predominantly localized to proximal TAs. This difference in the localization patterns of NMIIA and NMIIB in TAs was similar to that observed in U-2 OS cells [23,73]. I next examined the dynamics of NMIIA and NMIIB in cells expressing mCherry-NMHC-IIA and EGFP-NMHC-IIB (Figure 17B). Both isoforms localized in TAs exhibited dynamic centripetal flow in lamellae, whereas those localized in vSFs were less dynamic in cell bodies. Kymographs indicated that NMIIB was gradually incorporated into TAs that already contained NMIIA during centripetal flow (Figure 17C). These results suggest that nascent distal TAs are formed by only NMIIA and that gradual incorporation of NMIIB is associated with the maturation of TAs in fibroblasts.

2-2-3: NMIIA and NMIIB are required for formation of TAs and vSFs, respectively

To assess the involvement of NMIIA and NMIIB in the formation of the SF subtypes, I investigated the effects of KD of each NMHC-II isoform using isoform-specific siRNAs. Immunoblot analysis confirmed that transfection of siRNAs targeting NMHC-IIA and NMHC-IIB reduced endogenous expression of the corresponding isoform (Figure 18). Sato *et al*. previously demonstrated that expression of NMIIA is about 15-fold higher than that of NMIIB in SV1 cells [56]. Therefore, it should be noted that the total amount of NMII in SV1 cells was greatly decreased by KD of NMIIA, but was not markedly affected by KD of NMIIB.

Figure 19A shows representative images of the siRNA-treated cells stained with an anti-vinculin antibody and FITC-phalloidin. The three SF subtypes were observed in control siRNA-treated cells. NMIIA KD resulted in loss of TAs, as well as dSFs connecting to TAs at right angles, from the lamella and the formation of aberrant protrusions at the extending edge of cells. Although vSFs were observed in the cell body upon NMIIA KD, some were abnormally branched. On the other hand, NMIIB KD resulted in loss of vSFs from the cell body and the formation of relatively straight SFs in the lamella. We considered these relatively straight SFs to be TAs connecting to dSFs at both ends because they aligned and oriented toward the extending edge in parallel and exhibited centripetal flow, as mentioned later. In addition, almost all dSFs connecting to TAs at right angles disappeared in NMIIB-KD cells. Then, I quantified the percentages of NMIIA-KD and NMIIB-KD cells exhibiting each SF subtype. Only 12% of NMIIA-KD cells formed TAs (Figure 19B), whereas only 30% of NMIIB-KD cells formed vSFs (Figure 19C). The percentage of cells displaying dSFs connecting to TAs at right angles was decreased upon KD of NMIIA or NMIIB (Figure 19D). These results indicate that KD of each NMII isoform has distinct effects on the organization of SF subtypes. Specifically, NMIIA and NMIIB are required for the formation of TAs and vSFs, respectively. I confirmed that the phenotypes of siRNA-treated cells were caused by KD of each isoform (Figure 20). vSFs in

NMIIA-KD cells were immunoreactive for only NMIIB, whereas TAs in NMIIB-KD cells were immunoreactive for only NMIIA.

2-2-4: NMIIA and NMIIB are required for proper dynamics of TAs and vSFs, respectively

To assess the properties of the remaining SFs in NMIIA-KD and NMIIB-KD cells, we analyzed the dynamics of exogenously expressed mCherry-actin and EGFP-vinculin (Figure 21). The remaining vSFs became mobile in NMIIA-KD cells (Figure 21, A and B). The remaining TAs in NMIIB-KD cells exhibited centripetal flow; however, the flow rate was slower than in control cells (Figure 21), suggesting that these relatively straight TAs also have defects.

Next, I tried to establish a method for quantifying the size of FAs in SV-1 cells. To evaluate quantitative analysis using ImageJ, I used the nuclei of fission yeast *Schizosaccharomyces pombe* as a model. Because the outline of the fission yeast nuclei can be easily discriminated, it would be suitable for investigating quantitative analysis method. The nuclei of fission yeast were stained with DAPI (Figure 22A, left). The images were analyzed by the analysis tool of ImageJ, Analyze particle. We were able to obtain the reliable quantitative data, the area ($1.5 \pm 0.42\ \mu m^2$, n = 466 cells) of nuclei, using ImageJ (Figure 22A, right). Similarly, I quantified the area of FAs in SV-1 cells (Figure 22B). FAs connected to the ends of vSFs were smaller in NMIIA-KD cells than in control cells (Figure 22 C).

The formation and maturation of SFs and FAs are dependent on the tension applied to them [75,76]; therefore, vSFs in NMIIA-KD cells might be unable to generate normal contractile force.

2-2-5: Formation of vSFs is dependent on NMIIB

To test whether the alteration of SF subtypes organization in NMIIA-KD and NMIIB-KD cells is due to the lack of the specific isoform, we performed KD-rescue experiments using siRNA-insensitive EGFP-NMHC-II isoforms that were expressed under the regulation of a CMV promoter. Immunoblot analysis confirmed the expression of exogenous EGFP-NMHC-IIA and EGFP-NMHC-IIB (Figure 23). As expected, expression of exogenous EGFP-NMHC-IIA and EGFP-NMHC-IIB rescued the defects of NMIIA-KD and NMIIB-KD cells, respectively (Figure 24). Specifically, TAs formed in NMIIA-KD cells expressing EGFP-NMHC-IIA and vSFs formed in NMIIB-KD cells expressing EGFP-NMHC-IIB. EGFP-NMHC-IIB was able to localize in the distal region of the lamella and rescue the TA formation defect in NMIIA-KD cells. This indicates that NMIIB can form TAs when it is present in excess and localizes in the distal region of the lamella. However, exogenous EGFP-NMHC-IIA failed to rescue the defects of NMIIB-KD cells. Specifically, vSFs did not form in NMIIB-KD cells, even in the presence of excess exogenous EGFP-NMHC-IIA. This result indicates that the formation of vSFs is dependent on NMIIB.

2-2-6: Proper activation of NMII isoforms is required for the formation of TAs and vSFs

Activation of NMII by phosphorylation of its RLC subunit is critical for the formation of SFs [75,77]. We examined the effects of KD of each NMHC-II isoform on the phosphorylation status of the RLC (Figure 25). Levels of both 1P-RLC and 2P-RLC were decreased in NMIIA-KD cells. This decrease in RLC phosphorylation could be explained by a reduction in the total amount of NMII or by a loss of motor activity specific to NMIIA. Levels of 1P-RLC and 2P-RLC were also decreased in NMIIB-KD cells, despite the fact that most NMII molecules (i.e., NMIIA) remained, indicating that NMIIB is required for proper phosphorylation of the RLC. These results illustrate that proper activation of NMII isoforms is required for the formation of TAs and vSFs.

2-2-7: Both NMIIA and NMIIB are required to maintain lamellar flattening

Burnette *et al*. recently provided new insights into the function of TAs. They showed that TAs are required to maintain the thin and flattened shape of the lamella by mechanically coupling with dSFs [32] and also indicated that NMIIA is important for this lamellar flattening. However, NMIIB also localized to proximal TAs, in addition to NMIIA (Figure 17), which prompted us to investigate the involvement of NMIIB in lamellar shape. We compared the height of the peripheral region in each siRNA-treated cell using confocal microscopy (Figure 26). TAs, as well as vSFs, were observed in the ventral plane close to the basal region in control siRNA-treated cells, indicating that these cells had very thin and flattened lamellae. Although super-resolution 3D microscopy can separate the dorsal surface from the ventral surface of the lamella [32], the conventional confocal microscope used in this study produced images that showed these surfaces within the same plane of control cells. In NMIIA-KD cells, TAs were not observed and the peripheral region was thicker. These results demonstrate that TAs are required for lamellar flattening in SV1 cells, consistent with findings in U-2 OS cells [32]. In NMIIB-KD cells, however, the peripheral region was thicker even in the presence of TAs. Although both ends of TAs were observed in the ventral plane of lamellae, the central region of TAs was observed in the dorsal plane approximately 2 μm above the ventral plane (see the NMIIB-KD cell in Figure 26A). This result indicates that TAs lacking NMIIB cannot function properly in lamellar flattening.

Next, we performed KD-rescue experiments to determine whether the observed effects are due to the lack of the specific NMII isoform (Figure 27). We measured the height of lamellae in cells treated with each siRNA and expressing exogenous EGFP-NMHC-IIA or EGFP-NMHC-IIB. Lamella height in NMIIA-KD and NMIIB-KD cells was decreased to a level comparable to that in control cells upon expression of EGFP-NMHC-IIA and EGFP-NMHC-IIB, respectively. On the other hand, lamella height was not decreased in NMIIA-KD and NMIIB-KD cells upon exogenous expression of EGFP-NMHC-IIB and EGFP-NMHC-IIA, respectively, even though

TAs formed in these cells. In summary, the defects were not rescued by expression of the other isoform, suggesting that TAs lacking NMIIA or NMIIB cannot function in lamellar flattening. Although dSFs formed in NMIIA-KD and NMIIB-KD cells expressing exogenous NMIIB and NMIIA, respectively, a flattened lamella still failed to form. The presence of dSFs itself is probably not enough for lamellar flattening. Therefore, the presence of both NMIIA and NMIIB in TAs is necessary to maintain the thin and flattened shape of lamellae.

2-2-8: Both NMIIA and NMIIB are required for maintaining contracted state of TAs

To investigate TA defects in NMIIB-KD cells, we examined the arrangement of NMII filaments in TAs during centripetal flow. NMII filaments in TAs align at regular intervals, and the distance between the respective filaments decreases upon contraction of TAs during centripetal flow [32]. Furthermore, NMII filaments form a stack by aligning their long axes parallel to the extending edge in lamellae during centripetal flow [29,32,78,79]. Immunofluorescence staining of NMIIA showed periodic lines emanating from the stacks of NMII filament spots in the distal or proximal region of lamellae (Figure 28A). The distance between the stacks of NMII filaments was decreased in the proximal region of control cells (Figure 28, B and C). Moreover, TAs became less curved during centripetal flow. These results indicate that the length of TAs was shortened by contraction. However, there was no change in the distance between the stacks of NMII filaments in NMIIB-KD cells during centripetal flow (Figure 28, A–C), suggesting that the defect in lamellar flattening in these cells is due to the inability of TAs to contract.

Next, to determine the significance of each NMII isoform in proper contraction of TAs, we measured the distances between NMII filaments in cells treated with each siRNA and expressing exogenous EGFP-NMHC-IIA and EGFP-NMHC-IIB (Figure 28C). The distance between NMII filaments in the proximal region of NMIIA-KD and NMIIB-KD cells decreased to a level comparable to that in control cells upon exogenous expression of EGFP-NMHC-IIA and EGFP-NMHC-IIB, respectively. On the other hand, it was not decreased in NMIIA-KD and NMIIB-KD cells expressing exogenous EGFP-NMHC-IIB and EGFP-NMHC-IIA, respectively. In summary, the contraction defects were not rescued by expression of the other isoform. These results indicate that TAs containing only NMIIA or NMIIB are unable to contract properly. Both isoforms are required for the normal contraction of TAs during lamellar flattening (Figure 29).

2-2-9: Actin filaments in vSFs are in a stretched conformation

In chapter 1, I demonstrated that S1 probe (NMIIB-S1-R709C-EGFP) can recognize the conformational change of actin filaments and bind to the stretched actin filaments preferentially. To observe the behavior of S1 probe in live cells, I acquired time-lapse images of SV1 cells expressing S1 probe and mCherry-actin. S1 probe was observed in less mobile vSFs but not in

mobile TAs (Figure 30). I then investigated the involvement of each NMII isoform in the different actin filament conformational states using S1 probe (Figure 31). In control cells, S1 probe clearly localized along straight SFs, such as vSFs. In NMIIA-KD cells, binding of S1 probe to the remaining vSFs was decreased, demonstrating that actin filaments in vSFs lacking NMIIA are not highly stretched. However, we cannot conclude whether the decrease in S1 probe binding is due to the loss of total NMII molecules or the reduction in NMIIA-specific motor activity. Owing to the loss of vSFs in NMIIB-KD cells, we were unable to determine if S1 probe localizes along vSFs in the absence of NMIIB. S1 probe weakly localized to both ends of relatively straight TAs in lamellae of NMIIB-KD cells.

Moreover, the slight binding of S1 probe to the actin filaments in NMIIA-KD might be caused by cooperative binding of NMIIB heads, as suggested in the study of *Dictyostelium* myosin II [58,80]. Localization of exogenously expressed mCherry-NMHC-IIB showed good correlation with that of S1 probe in vSFs (Figure 32). This could support the cooperative binding of NMIIB heads. Because vSFs were disappeared in NMIIB-KD cell, S1 probe was not localized particular region at cell body. Indeed, I did not observe that S1 probe was localized at any particular sites in the cells losing SFs by treated with BBS or Y-27632 (Figure 10). Taken together, these results suggest that the actin filaments in straight SFs such as less mobile vSFs, but not those of mobile TAs, are in the stretched conformation (Figure 33).

2-3: Discussion

In this chapter, I found that NMIIA and NMIIB are required for the formation of TAs and vSFs in fibroblasts, respectively. Moreover, I demonstrated that both isoforms are necessary for the proper organization and function of each SF subtype (Figure 34).

SFs are dynamic structures that are organized in a spatiotemporally regulated manner in cells, and the turnover of NMII by assembly/disassembly of filaments is important for this organization [2,3,81]. TAs form at the interface between lamellipodia and lamella [28,30]. NMIIA filaments are turned over more rapidly than NMIIB filaments in cells, and consequently NMIIA arrives at newly formed lamellae prior to NMIIB [53,55,82]. This is consistent with the notion that NMIIA is involved in the formation of TAs (Figure 19) [28,32,83]. The expression level of NMIIB is only about one-fifteenth of that of NMIIA in SV1 cells [56]. Therefore, the low level of remaining NMIIB molecules in NMIIA-KD cells might prevent delivery of this isoform to the distal region of the lamella; most molecules would form vSFs in the cell body. Exogenously expressed NMIIB rescued the formation of TAs in NMIIA-KD cells; however, excess exogenous NMIIB did not localize to the distal region of the lamella in NMIIB-KD cells, in which endogenous NMIIA was expressed (Figure 24). We speculate that excess exogenous NMIIB can reach the distal region of the lamella and form TAs in this region when endogenous NMIIA, which

normally forms nascent TAs and occupies the position of NMIIs in those TAs, is depleted. Therefore, regarding the formation of TAs, NMIIB can functionally compensate for the loss of NMIIA if it can reach the region where nascent TAs form.

A distinctive morphological feature of the lamella is its extremely thin and flattened shape. Burnette *et al*. proposed that mechanical coupling exists between TAs and dSFs and that TA contractility generates the force needed to pull dSFs inward and to flatten lamellae [32]. They showed that the flattened shape of lamellae is not maintained in COS-7 cells (NMIIA-null) and NMIIA-KD U-2 OS cells and that this defect is rescued by exogenous expression of NMIIA. Based on these findings, they proposed that NMIIA is indispensable for lamellar flattening. In this study, we found that NMIIB-KD cells lacked flattened lamellae, even though TAs, which consisted only of NMIIA, formed (Figure 24). TAs consisting only of NMIIB, which formed in NMIIA-KD cells expressing excess exogenous NMIIB, were also unable to flatten the lamella. We speculate that loss of TA contractility (Figures 27 and 28) is the main cause of the lamellar flattening defect. To maintain the uniformly thin and flattened shape of the lamella, a greater contractile force may be required in the proximal region than in the distal region due to the thickness of the cell body. NMIIB predominantly localizes to proximal TAs, whereas NMIIA localizes along all TAs in U-2 OS cells [23,73] and SV1 cells (Figure 17). It was recently demonstrated that NMIIA and NMIIB co-assemble into hetero-filaments in cells [73,74]. The incorporation of NMIIB into pre-formed filaments consisting of NMIIA during centripetal flow was directly observed by live cell imaging using super-resolution microscopy [73]. Although the underlying molecular mechanism that explains why both NMIIA and NMIIB are required for lamellar flattening is unclear, we speculate that TAs might be able to generate tension via the incorporation of NMIIB into pre-formed NMIIA filaments. NMIIB is a relatively high duty ratio motor [16,18]. Moreover, the ADP release rate of both isoforms, especially NMIIB, is decreased by the resisting load, suggesting that NMIIB plays a role in the maintenance of tension [19]. In addition to the high motor activity of NMIIA, this unique property of NMIIB (tension-bearing role) might help to maintain actin filaments in the contracted state in TAs.

Less is known about the organizational properties of vSFs than about those of TAs. In particular, the mechanism via which vSFs form at the ventral surface in the central region of the cell body remains obscure [22,24]. It has been proposed that some vSFs are generated via the fusion of TAs with dSFs [30]. Consequently, these vSFs are arch-like structures with their central regions localizing beneath the dorsal surface and both their ends linking to FAs in the ventral surface and orienting parallel to the leading edge [43,84]. However, typical vSFs formed in the central region are unlikely to be generated via this mechanism because their orientation and location differ from the arched vSFs formed from TAs and dSFs. Beach *et al*. recently observed the formation of TAs and typical vSFs simultaneously using super-resolution 3D microscopy [83].

Their findings suggest that typical vSFs do not form via the fusion of TAs with dSFs. Thus, hereafter we refer to typical vSFs simply as vSFs. vSFs can form in COS-7 cells [32,85] and NMIIA-KD SV1 cells (Figure 19). Moreover, vSFs almost completely disappeared in NMIIB-KD cells and exogenous expression of NMIIA failed to rescue this defect (Figures 19 and 23). The disappearance of SFs and FAs from the central region of the cell body upon NMIIB KD has been reported in other cell types [35,40,41]. Thus, it is assumed that NMIIB is indispensable for the organization of vSFs and that NMIIA cannot replace the function of NMIIB in this context. The unique tension-bearing role of NMIIB might be necessary for the organization of vSFs. In this study, we referred to arch-like SFs, which formed via the fusion of TAs with dSFs in the proximal region of the lamella, as TAs rather than vSFs based on the localization of their central portion at the dorsal surface [32,43] and their function in lamellar flattening. However, this terminology may be confusing because the ends of these SFs link to FAs, which could be derived from dSFs [30]. Consequently, this SF may need to be renamed in the future.

TAs are transient structures; they undergo centripetal flow and eventually disappear near the end of the lamella [27–29]. FHOD1, a member of the formin protein family, promotes SF formation when phosphorylated by ROCK/Rho-kinase [86]. The constitutively active form of FHOD1 can induce the formation of TAs, followed by the conversion of TAs to stable-arched vSFs, which results in the alignment of straight and arched vSFs throughout cells [43]. In other word, FHOD1 can stop the disappearance of TAs. The other formin, DAAM1, might have a function similar to FHOD1 because overexpression of DAAM1 promotes the alignment of vSFs, which are enriched in NMIIB [87]. Here, I propose that the increase of NMIIB as well as 2P-RLC in mature TAs associates with the Rho-GEF-dependent positive feedback loop (Figure 35). This loop might stop rotating near the proximal end of lamellae by an unidentified mechanism, resulting in the disappearance of mature TAs before the conversion to stable arched vSFs was achieved (Figure 16). In this chapter, I used cells exhibiting the three SF subtypes and showed the disappearance of mature TAs. However, I also observed different cells showing aligned straight SFs (probably stable-arched vSFs) containing NMIIB and 2P-RLC (Figure 36). I suppose that when the positive feedback loop is not terminated, mature TAs would convert to stable-arched vSFs, and cells exhibit aligned SFs. The reason why the positive feedback loop continues to rotate in certain cases is unclear. Perhaps, the suppression of the activity of myosin light chain phosphatase negatively regulating NMII might be involved in the formation of aligned SFs.

In addition to their mechanisms of formation, the dynamics of vSFs and TAs also significantly differ. TAs can shorten in length during centripetal flow, probably because they have a curved shape. By contrast, the length of vSFs remains constant, in association with their less dynamic movement, because they are linked to FAs at both ends and have a straight shape (Figure 15). Therefore, tension would be high in vSFs in the so-called isometric contraction state [25,88].

In this chapter, we showed that S1 probe bound to relatively straight SFs such as vSFs (Figures 29 and 30). This binding was increased by external stretching of cells (Figure 12 in chapter 1). Traction force microscopy, which images displacement of a substrate by cells, revealed that NMIIA-KD cells cannot generate proper traction force [41,42,89]. This correlates well with our finding that binding of the S1 probe to vSFs was decreased in NMIIA-KD cells (Figure 31).

Recently, a related paper to this study was published, which reports that NMIIA and NMIIB favor formation of TAs and vSFs, respectively [90]. The authors demonstrated that the expression ratio between NMIIA and NMIIB is important for the organization of SF subtypes. Specifically, TAs and vSFs predominantly form in NMIIA-enriched and NMIIB-enriched cells, respectively. They also showed that NMIIA can accelerate NMIIB dynamics in SFs by forming hetero-filaments. Consequently, the localization of NMIIB is dependent on the expression level of NMIIA in REF52 and COS-7 cells; NMIIB localizes to the distal region of the lamella and forms TAs in cells expressing a high level of NMIIA, but not in cells lacking NMIIA. By contrast, exogenous NMIIB localized in the distal region of the lamella and formed TAs in NMIIA-KD SV1 cells (Figure 24). In the other case, I found that NMIIB localizes to the posterior region in the migrating TIG-1 cells (human normal fibroblasts that have a polarized shape during migration) and that exogenously expressed NMIIB is still restricted to the posterior region in the NMIIA-KD cells as described below (Chapter 3). These differences in the behavior of NMIIB might be due to differences in intracellular signaling pathways between the cell lines.

2-4: Conclusion

Taken together, I demonstrated that NMIIA and NMIIB contribute differently to the organization of SF subtypes in fibroblasts. It should be noted that KD of NMIIB significantly affects the organization of SF subtypes even though its expression level is much lower than that of NMIIA. NMIIB would maintain the contraction state of the actomyosin structure, which is hardly performed by NMIIA. Further studies on the ultrastructure of the three SF subtypes by taking into account their three-dimensional features to the organization and on the contribution of ratio of endogenous NMII isoforms to regulation of SF subtypes will provide more insights on the roles of the NMII isoforms in cellular functions.

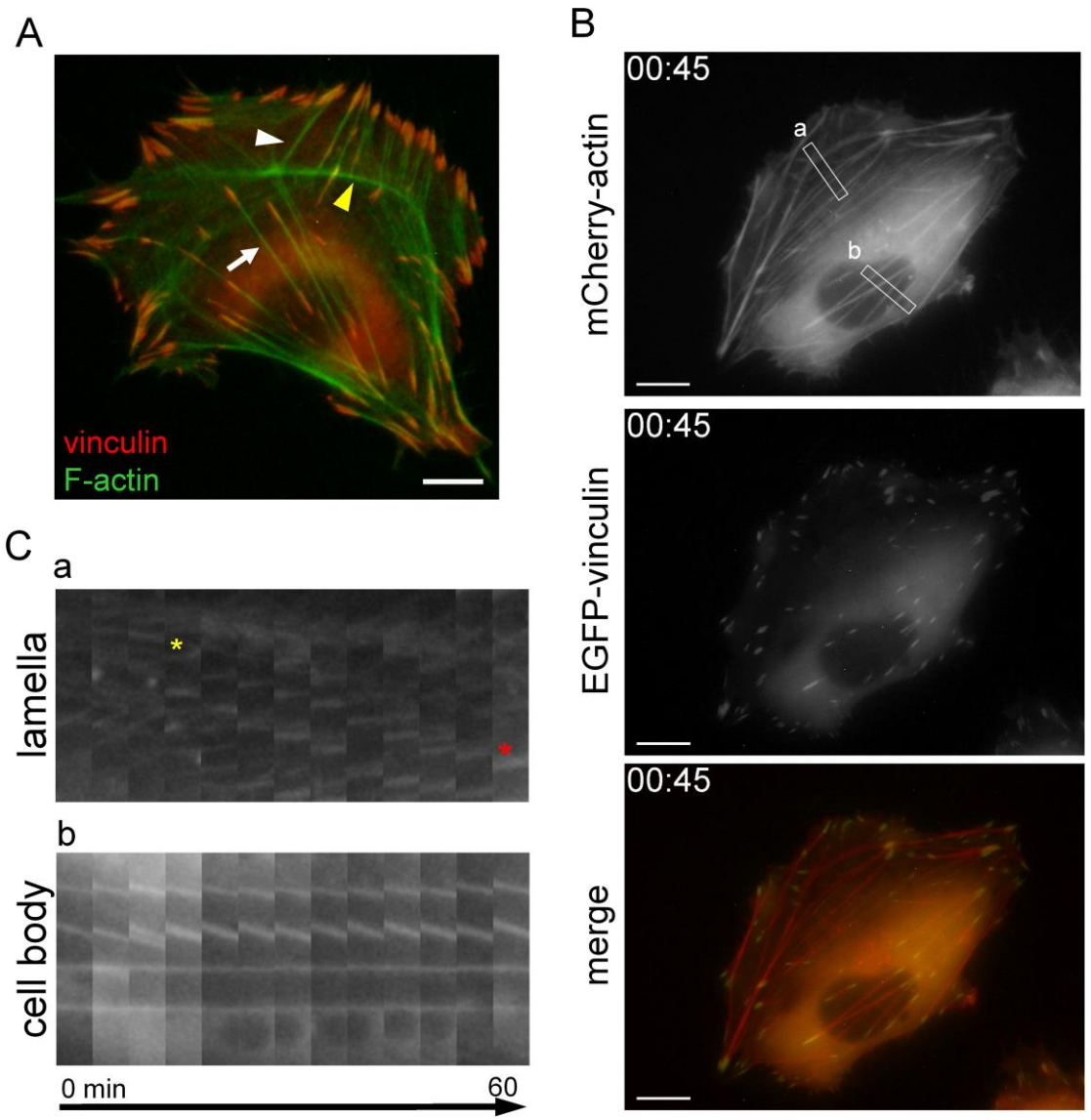

Figure 15. Organization and dynamics of SF subtypes.
(A) SV1 cells were fixed and stained with an anti-vinculin monoclonal antibody (red) and FITC-phalloidin (green). The white arrow and white arrowhead point to a representative vSF and dSF, respectively. The yellow arrowhead points to a representative TA. (B) Still image showing exogenous mCherry-actin (top) and EGFP-vinculin (middle) fluorescence in a live SV1 cell. (C) Kymographs generated from the boxed regions in panel C. Boxes a and b show the centripetal flow of TAs in lamella and the static behavior vSFs in cell body, respectively. Yellow and red asterisks indicate the first and the last tracks of the representative TA, respectively. All images were captured using a conventional fluorescence microscope. Bar, 10 μm.

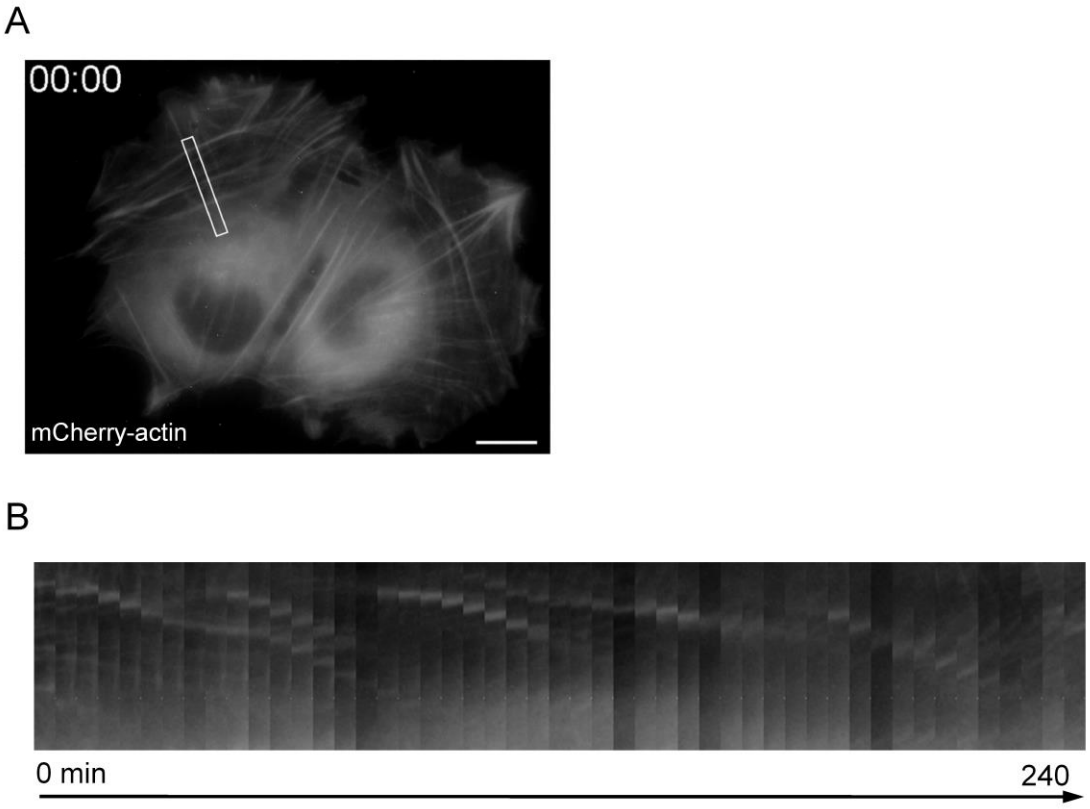

Figure 16. Disappearance of transverse arcs in proximal region of lamellae.
(A) Still image showing exogenous mCherry-actin fluorescence in live SV1 cells. (B) Kymograph generated from the boxed region in panel A. Note that mature TAs were transiently generated in the same region and disappeared from the proximal region in lamellae. Bar, 10 μm. All images were captured using a conventional fluorescence microscope.

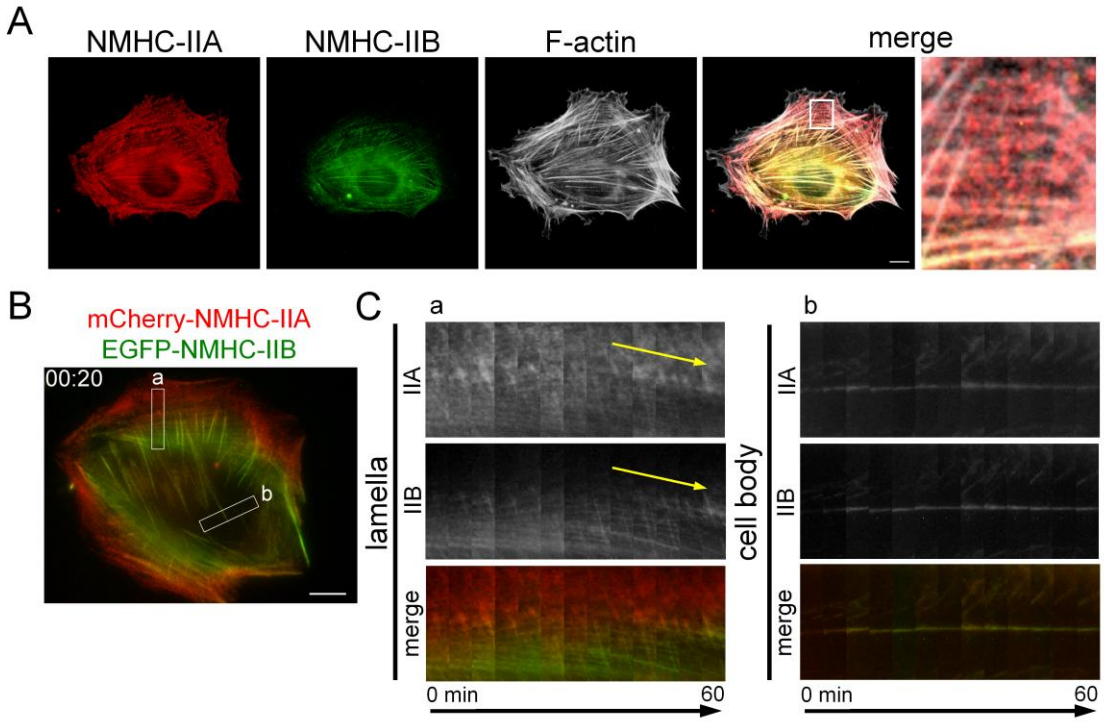

Figure 17: Localization and dynamics of NMII isoforms in SF subtypes
(A) SV1 cells were fixed and stained with an Alexa Fluor 596-conjugated anti-NMHC-IIA polyclonal antibody (red), Alexa Fluor 488-conjugated anti-NMHC-IIB polyclonal antibody (green), and Alexa Fluor 350-phalloidin (gray). The enlarged image of boxed region in the merged image shows the lamellar region. Note that the red puncta corresponding to NMIIA were distributed in the TAs. (B) Still image showing exogenous mCherry-NMHC-IIA and EGFP-NMHC-IIB fluorescence in a live SV1 cell. (C) Kymographs generated from the boxed regions in panel B. Left (box a) and right (box b) panels exhibit the centripetal flow of TAs in lamella and the less mobile vSFs in cell body, respectively. Yellow arrows emphasize the slopes indicating the centripetal flow of TAs. All images were captured using a conventional fluorescence microscope. Bar, 10 μm.

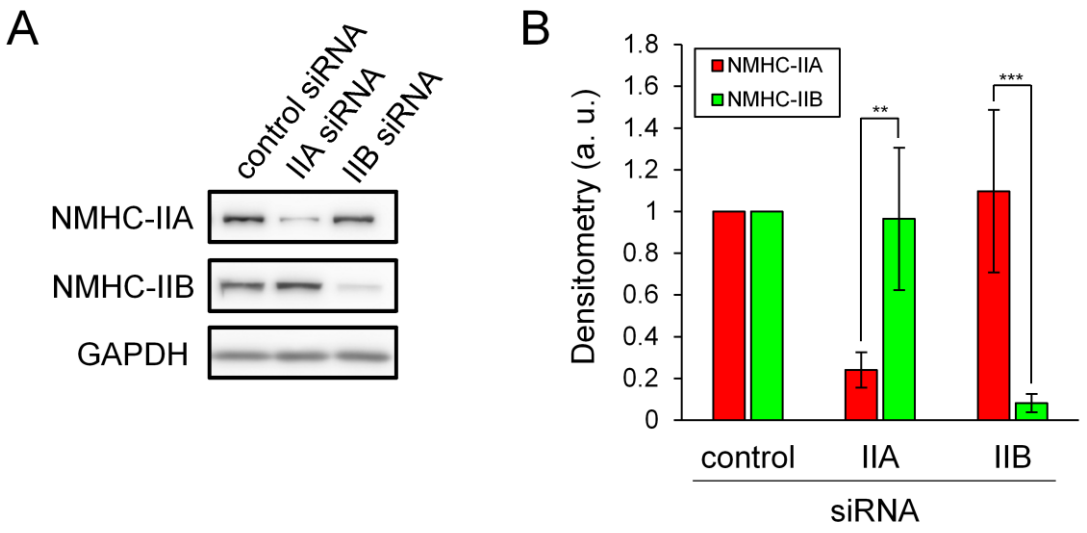

Figure 18. Confirmation of knockdown of NMIIA or NMIIB

(A) Immunoblot analyses of the expression levels of each NMII isoform in siRNA-treated cells. GAPDH was used as a loading control. (B) Quantification of the expression level of each NMII isoform. Data represent the mean ± SD from four independent experiments. $^{**}P < 0.005$. $^{***}P < 0.0005$.

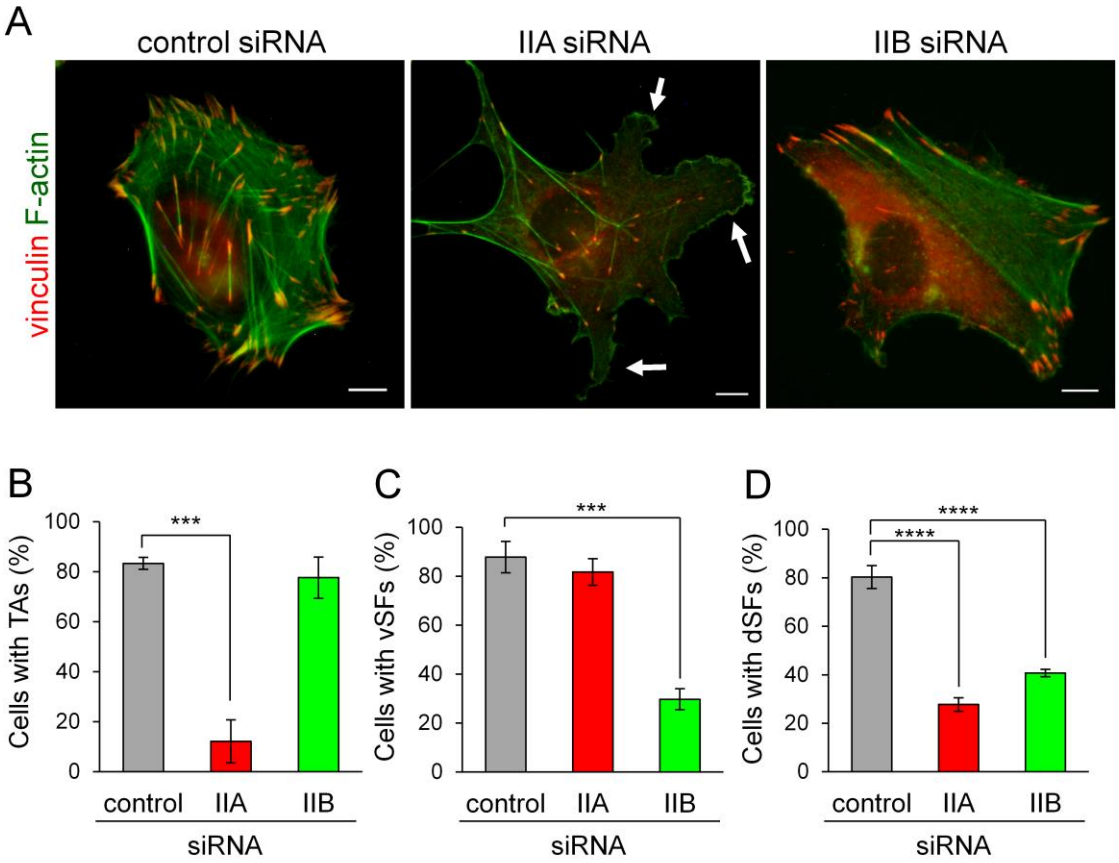

Figure 19. Formation of SF subtypes in NMIIA-KD or NMIIB-KD cells.
(A) SV1 cells treated with the indicated siRNA were fixed and stained with an anti-vinculin monoclonal antibody (red) and FITC-phalloidin (green). White arrows point to aberrant protrusions at the leading edge. Note that TAs in lamella and vSFs in cell body disappeared in NMIIA-KD and NMIIB-KD cells, respectively. (B–D) Percentages of cells exhibiting TAs (B), vSFs (C), and dSFs connecting to TAs at right angles (D) upon treatment with the indicated siRNAs. Data represent the mean ± SD from three independent experiments with n > 30 cells per experiment. ***$P < 0.0005$, ****$P < 0.00005$. (E) Box plot of the FA area in each of the siRNA-treated cells (n > 130 FAs from > 4 cells/condition). Note that the FA size in NMIIA-KD cells was significantly smaller than that of control cells. ***$P < 0.0005$.

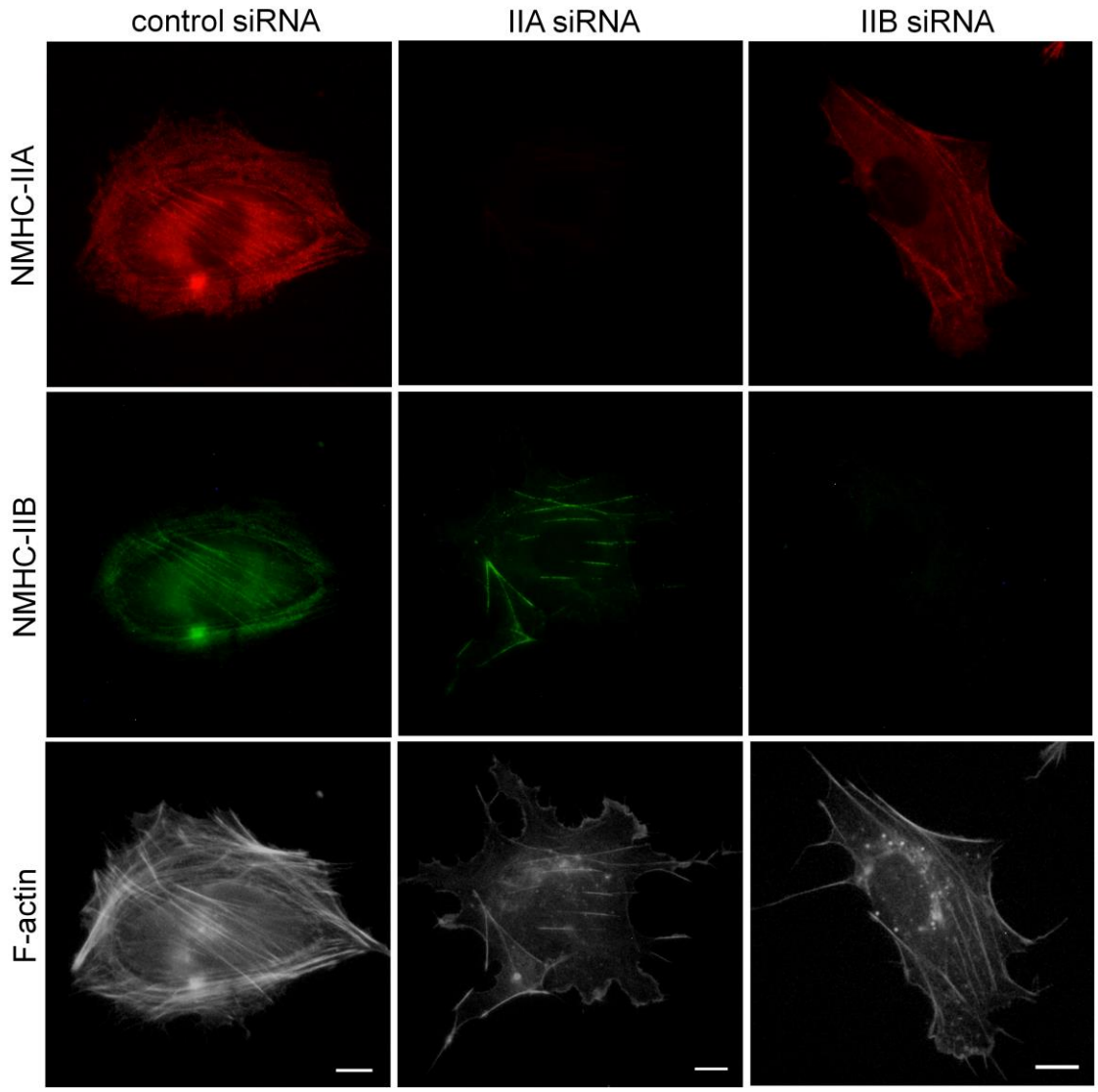

Figure 20. Confirmation of corresponding NMII isoform KD in phenotype of each KD cell.
SV1 cells treated with the indicated siRNAs were fixed and stained with an Alexa Fluor 596-conjugated anti-NMHC-IIA polyclonal antibody (red), an Alexa Fluor 488-conjugated anti-NMHC-IIB polyclonal antibody (green), and Alexa Fluor 350-labeled phalloidin (gray). vSFs in NMIIA-KD cells (forming aberrant protrusions at the extending edge) were immunoreactive for only NMIIB, whereas TAs in NMIIB-KD cells (relatively slender) were immunoreactive for only NMIIA. NMIIA-KD and NMIIB-KD cells displaying these morphological phenotypes were analyzed in this study. All images were captured using a conventional fluorescence microscope. Bar, 10 μm.

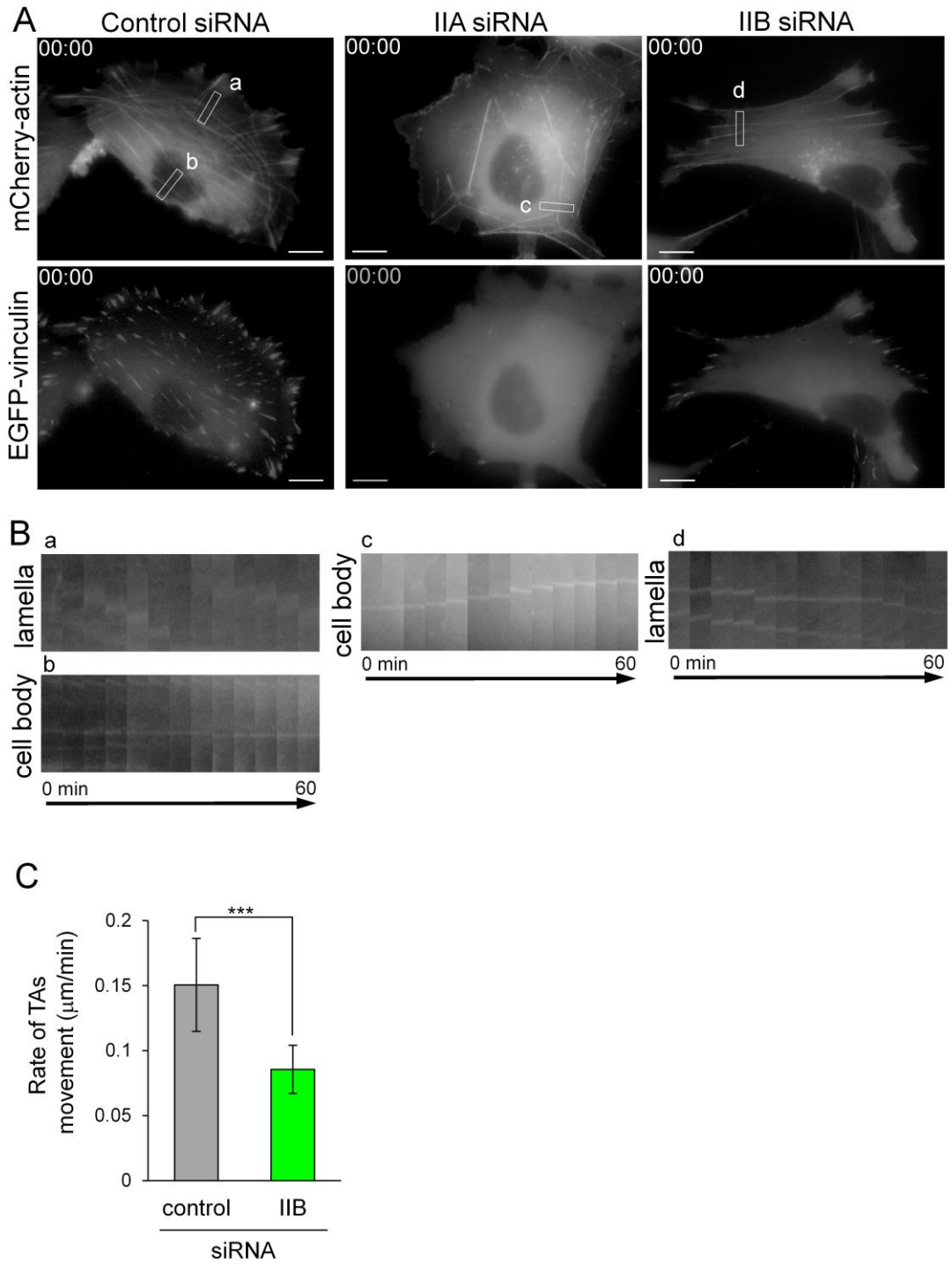

Figure 21. Dynamics of each SF subtype in siRNA-treated cells.
(A) Still images of the indicated siRNA-treated live cells expressing mCherry-actin (top) and EGFP-vinculin (bottom). All images were captured using a conventional fluorescence microscope. Bar, 10 μm. (B) Kymographs generated from the boxed regions in panel A. Boxes a and d show the TAs in the lamella and boxes b and c show the vSFs in the cell body. (C) Centripetal flow rates of TAs in control and NMIIB-KD cells. (n > 9 TAs from > 5 cells/condition). ***$P <$ 0.0005.

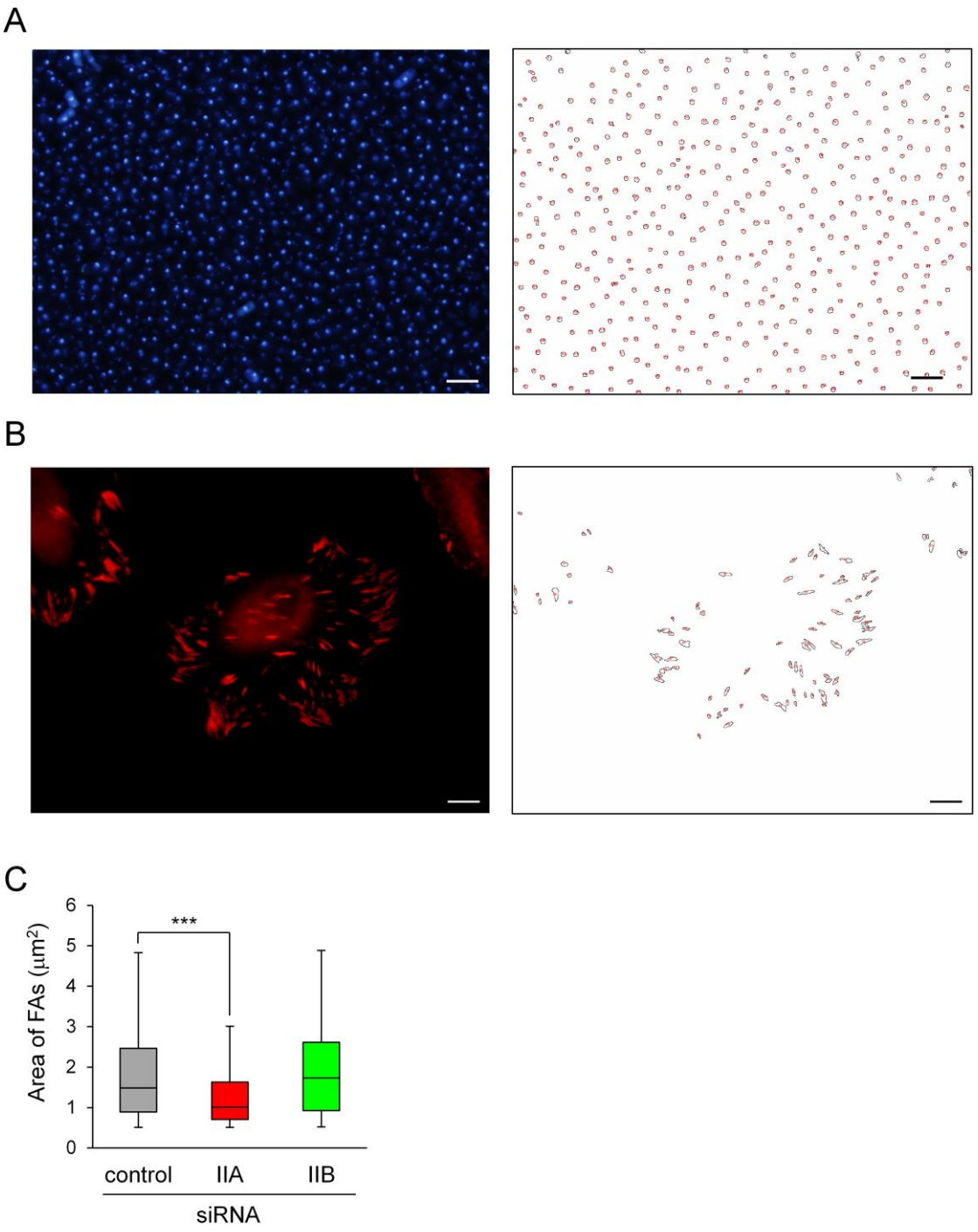

Figure 22. Quantification of the size of FAs in siRNA-treated cells.
(A) Fission yeast cells were stained with DAPI (left). The outline of nuclei was determined using analysis tool of ImageJ, Analyze particle (right). (B) Quantification of the size of FAs. Fluorescent image of FAs in control siRNA-treated cell (left). The outline of FAs was determined using analysis tool of ImageJ (right). Bar, 10 μm. (C) A box plot of the FA area in the indicated siRNA-treated cells (n > 130 FAs from > 4 cells/condition). ***$P < 0.0005$.

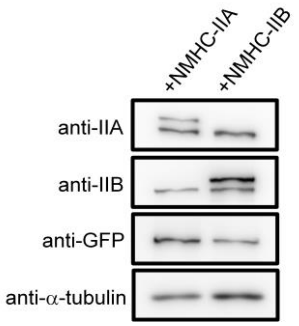

Figure 23. Confirmation of EGFP-NMHC-IIA and EGFP-NMHC-IIB expression in SV1 cells.
Expression of EGFP-NMHC-IIA and EGFP-NMHC-IIB was confirmed by immunoblotting with anti-NMHC-IIA, anti-NMHC-IIB, and anti-GFP antibodies. The slow migrating bands in the anti-NMHC-IIA and anti-NMHC-IIB panels correspond to EGFP-NMHC-IIA and EGFP-NMHC-IIB, respectively. An anti-α-tubulin antibody was used as a loading control. The anti-NMHC-IIA and anti-NMHC-IIB antibodies did not cross-react with EGFP-NMHC-IIB and EGFP-NMHC-IIA, respectively, confirming their specificity.

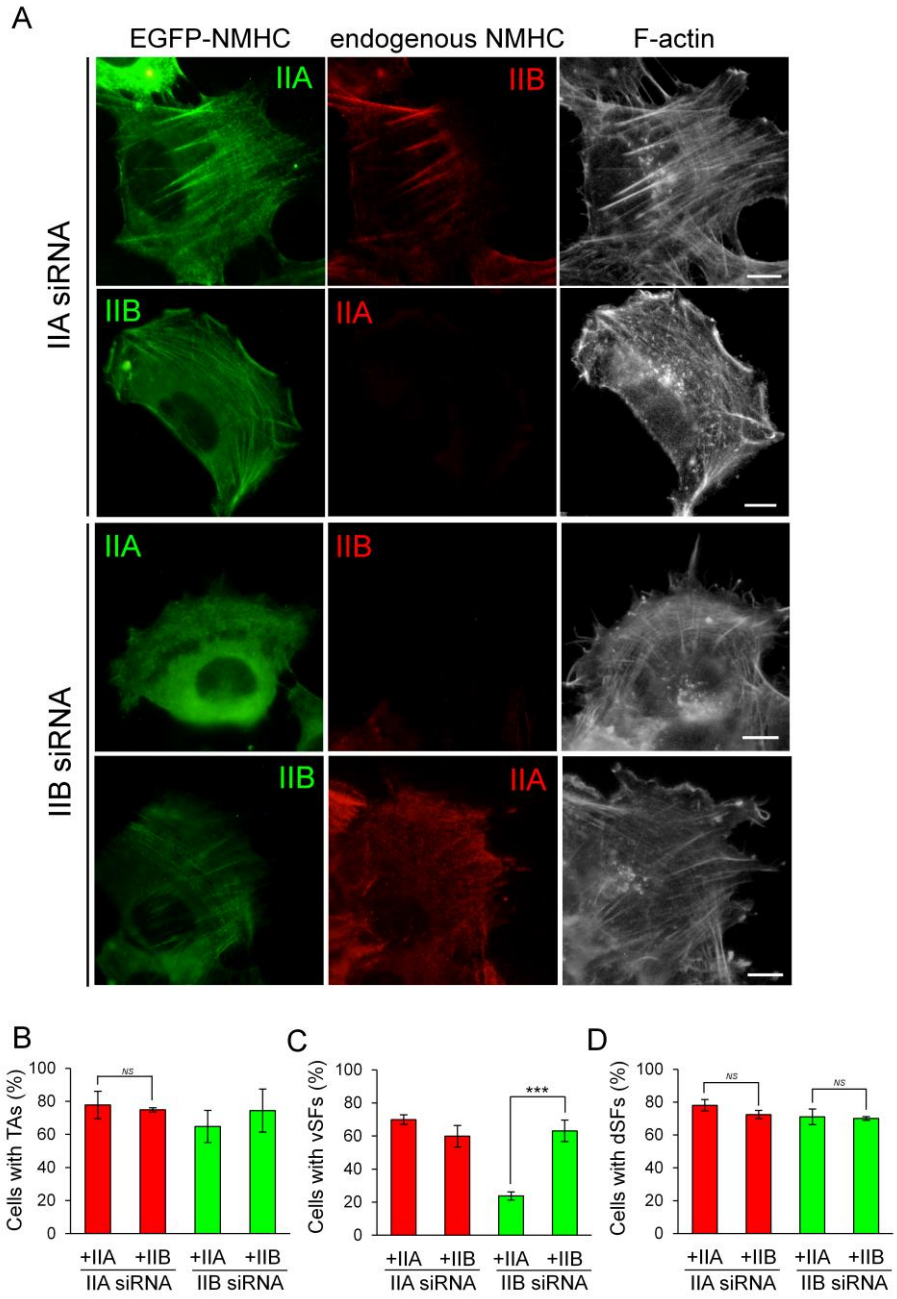

Figure 24. Rescue experiments of the SF formation defect in NMIIA-KD and NMIIB-KD cells by exogenous expression of each NMII isoform.

(A) Representative images of NMIIA-KD and NMIIB-KD cells expressing siRNA-insensitive EGFP-NMHC-IIA or EGFP-NMHC-IIB. The cells were fixed and stained with the indicated NMHC-II antibodies (red) and Alexa-Fluor 350-phalloidin (gray). Note that exogenous EGFP-NMHC-IIB localized throughout the lamella in NMIIA-KD cells, but did not localize to the distal region of the lamella in NMIIB-KD cells, which expressed endogenous NMIIA. All images were captured using a conventional fluorescence microscope. Bar, 10 μm. (B–D) Percentage of cells exhibiting TAs (B), vSFs (C), and dSFs connecting to TAs at right angles (D). Note that NMHC-IIB rescued the defect in TA formation in NMIIA-KD cells, but NMHC-IIA failed to rescue the defect in vSF formation in NMIIB-KD cells. Data represent the mean ± SD from three independent experiments with n > 30 cells in each experiment. ***$P < 0.0005$.

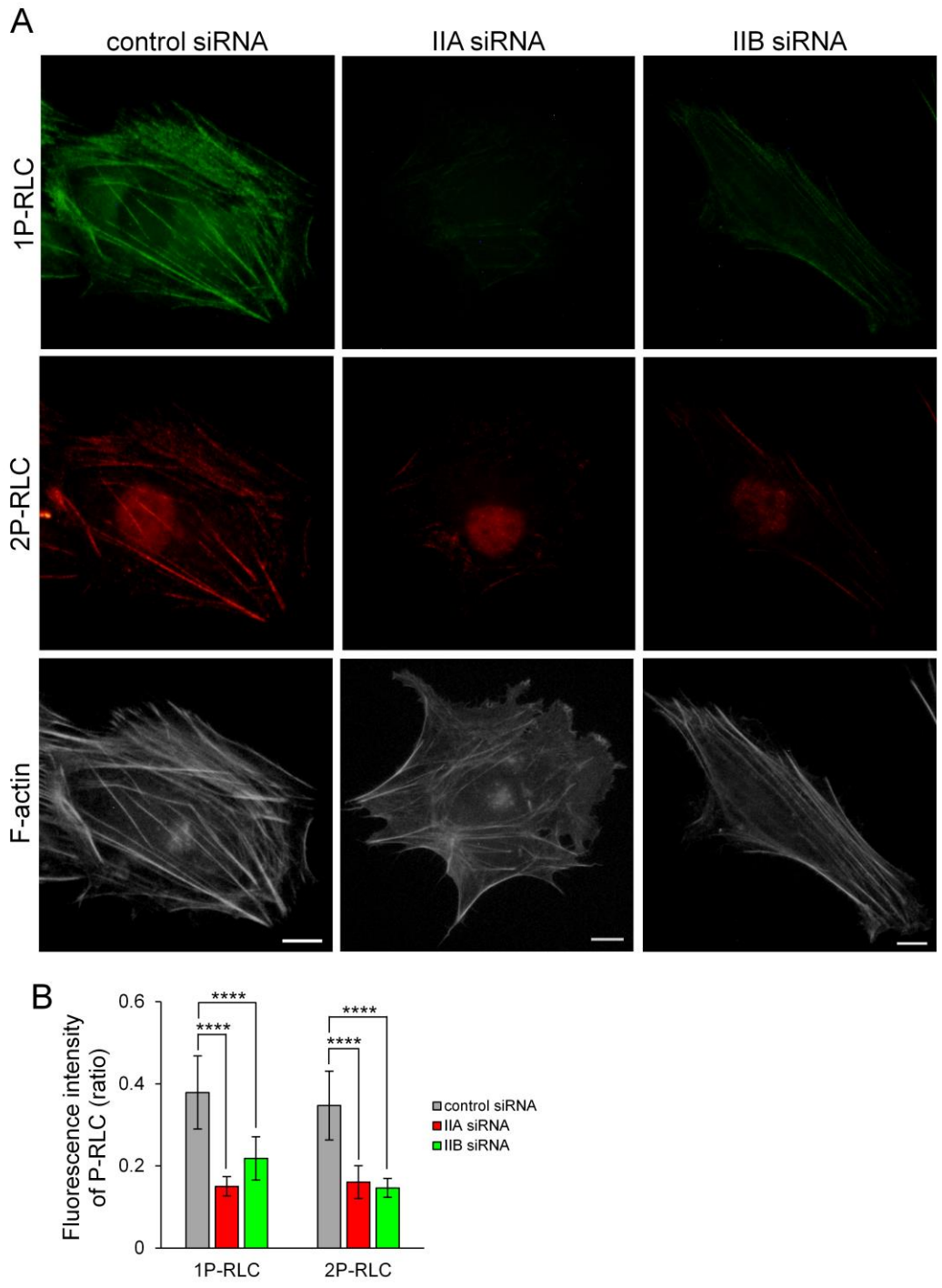

Figure 25. Phosphorylation of RLC in NMIIA-KD and NMIIB-KD cells.
(A) SV1 cells treated with the indicated siRNAs were fixed and stained with an anti-1P-RLC monoclonal antibody (green), an anti-2P-RLC polyclonal antibody (red), and Alexa Fluor 350-phalloidin (gray). Note that levels of both 1P-RLC and 2P-RLC were markedly decreased upon KD of each NMII isoform. Bar, 10 μm. All images were captured using a conventional fluorescence microscope. (B) Fluorescence intensities of 1P-RLC and 2P-RLC relative to that of F-actin throughout cells were quantified using the RGB Measure plugin of ImageJ software. Data represent the mean ± SD from n > 50 cells/condition. ****$P < 0.00005$.

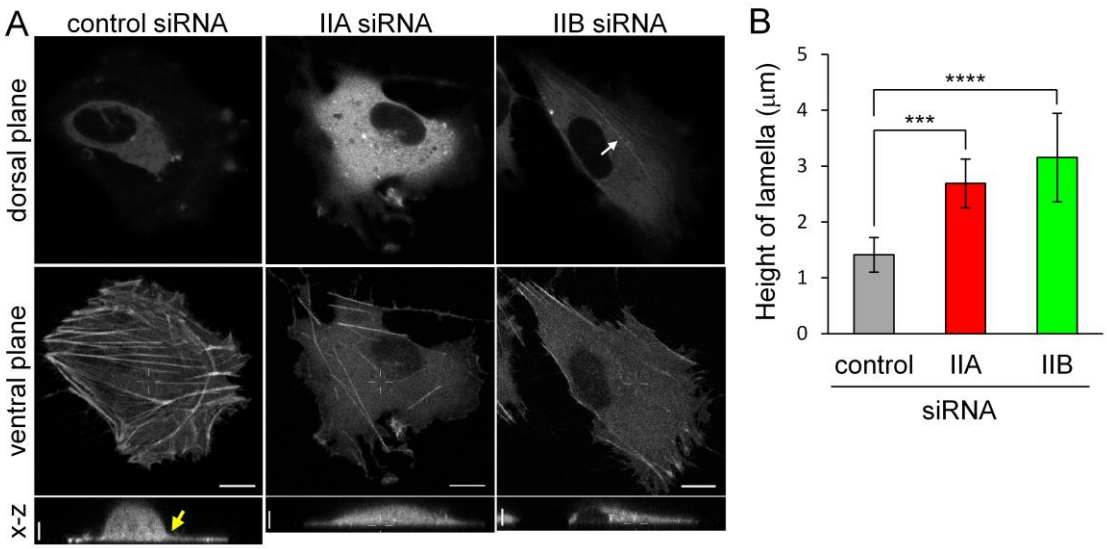

Figure 26. Both NMIIA and NMIIB are required for the normal lamellar flattening.
(A) SV1 cells expressing mCherry-actin were treated with the indicated siRNAs. The dorsal planes are 2 μm above the ventral planes. The white arrow in the dorsal plane of the NMIIB-KD cell points to a remaining TA. Side views are x-z maximum intensity projections of the white lines in each ventral plane. The yellow arrow in the side view of the control siRNA-treated cell indicates the boundary between the lamella and cell body. Note that this boundary was clear in the control cell, but not in NMIIA-KD and NMIIB-KD cells. (B) Height of lamellae in NMII-KD cells. The portion corresponding to the lamella was defined as that between the highest portion of the cell body and the extending edge of the cell in the side view, and its height was measured by ImageJ software. Data represent the mean ± SD from n > 8 cells. ***$P < 0.0005$. ****$P < 0.00005$.

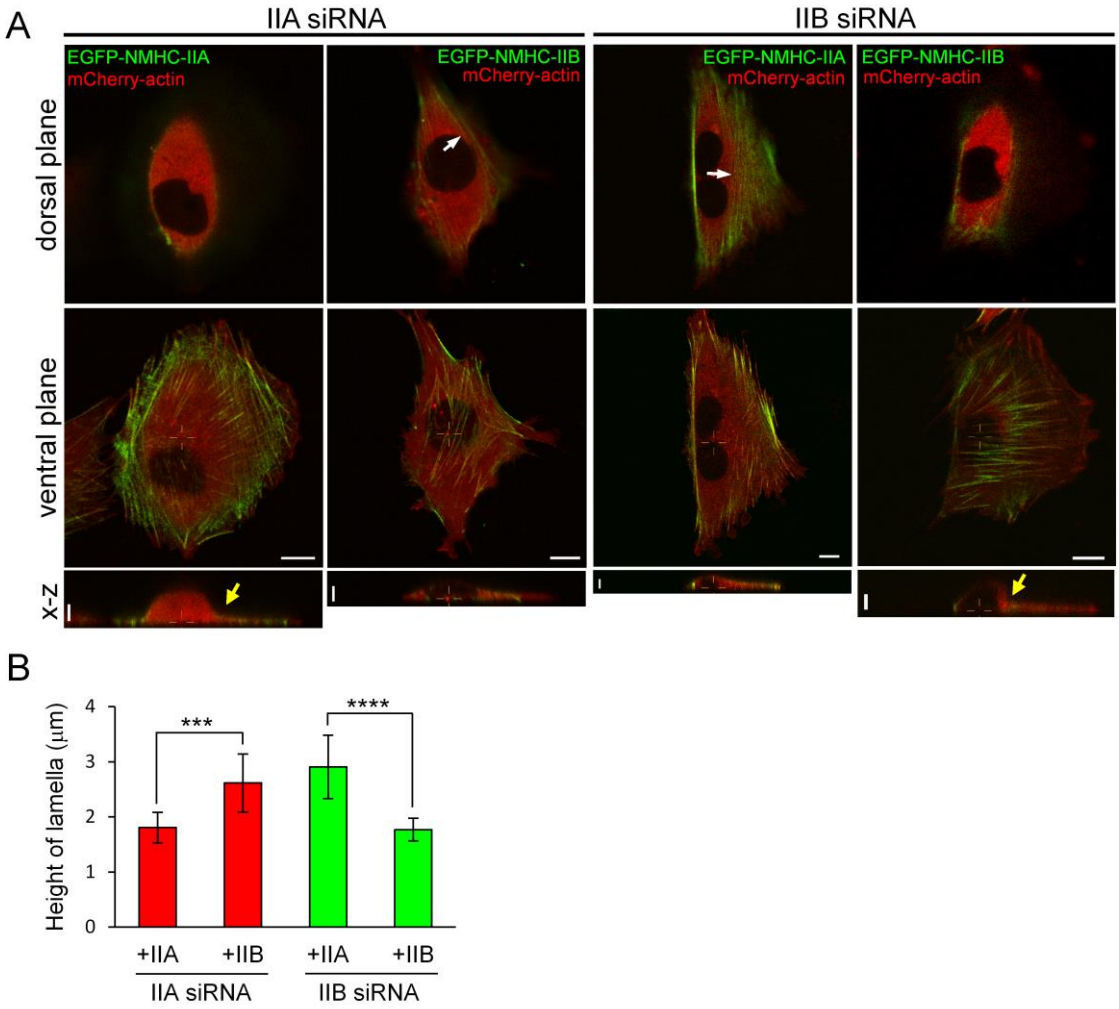

Figure 27. Rescue of lamellar flattening in each NMII KD cell by re-expressing respective NMII isoform.
(A) SV1 cells treated with the indicated siRNAs were transfected with the indicated siRNA-insensitive EGFP-NMHC-II isoform and mCherry-actin. White arrows in the dorsal plane point to TA. Yellow arrows in the side views indicate the boundary between the lamella and cell body. Note that this boundary is clear in NMIIA-KD and NMIIB-KD cells expressing exogenous NMIIA and NMIIB, respectively. Also note that exogenously expressed NMIIB localized to the distal region of the lamella in NMIIA-KD cells, but not in NMIIB-KD cells. (B) Height of lamella in NMII isoform KD cells expressing the indicated EGFP-NMHC-II isoform and mCherry-actin. Data represent the mean ± SD from n > 11 cells. ***$P < 0.0005$. ****$P < 0.00005$. All live cell images were captured using a confocal microscope. X-Y views; bar, 10 μm. X-Z views; bar, 5 μm.

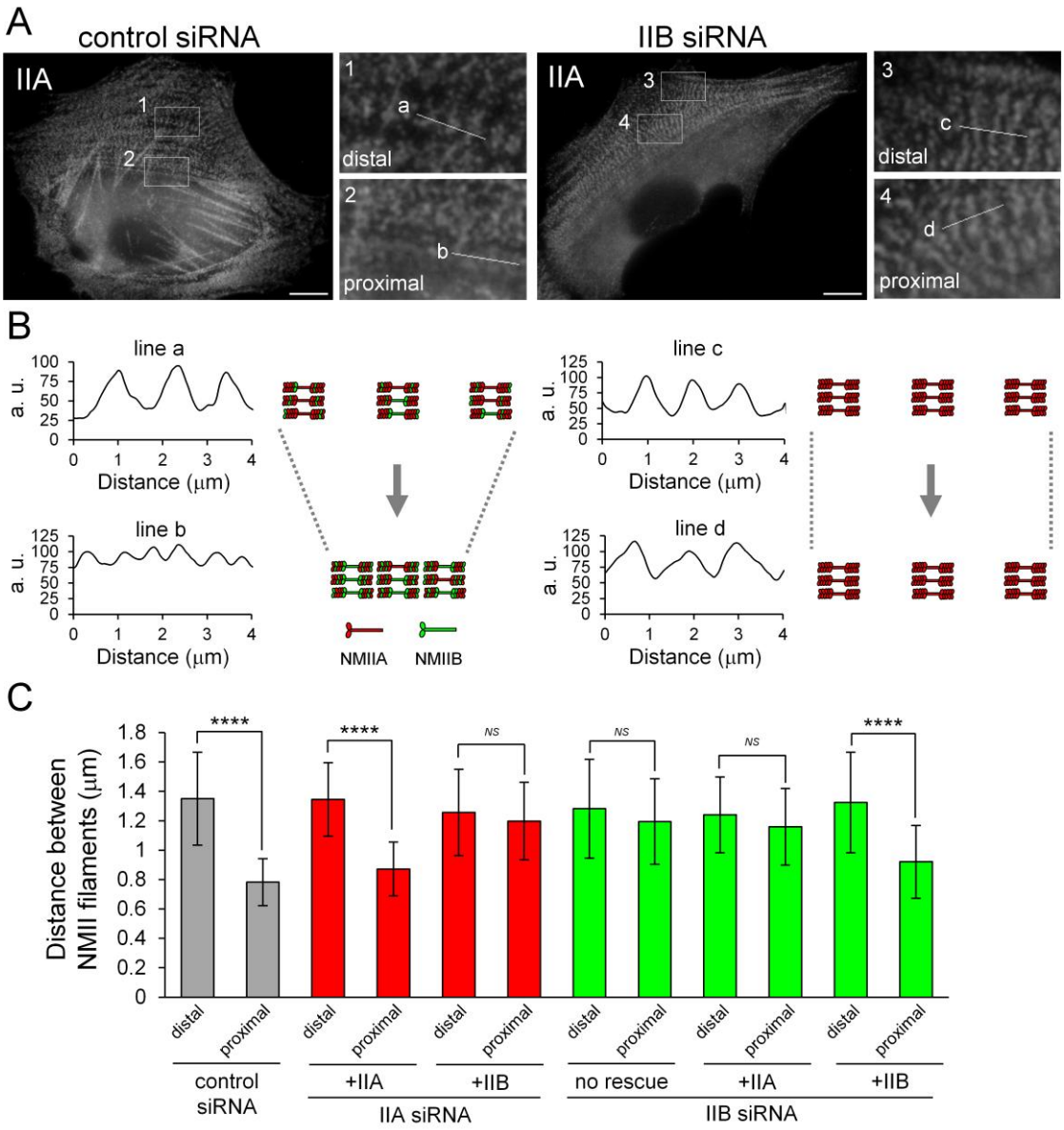

Figure 28. Both NMIIA and NMIIB are required for normal contraction of TAs.
(A) SV1 cells treated with the indicated siRNAs were fixed and stained with an Alexa Fluor 596-conjugated anti-NMHC-IIA polyclonal antibody. Enlarged images of the boxed regions in the overall image showing the central portion of TAs. Images were captured using a conventional fluorescence microscope. Bar, 10 μm. (B) Scans along the white lines in panel A showing the distances between the stacks of NMII filaments in TAs. The schematic illustrations indicate the contraction process of TAs in each condition. (C) Quantification of the distance between NMII filaments in each condition (n > 30 pitches from > 5 cells/condition). The distances between NMII filaments were measured by the RGB Profile plot plugin of ImageJ software. ****$P < 0.00005$. Note that the distance between stacks was not decreased in NMIIB-KD cells during centripetal flow.

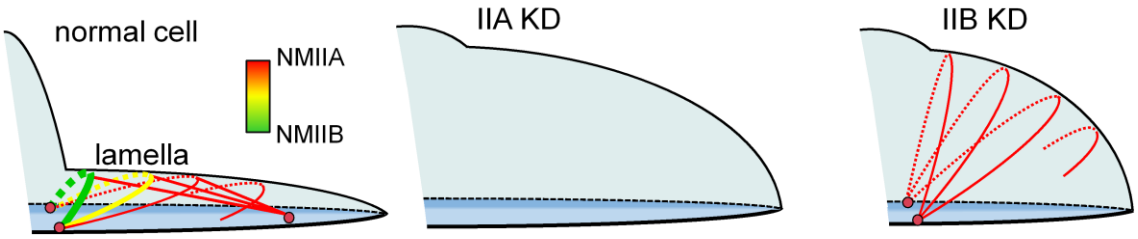

Figure 29. Model for the role of TAs in lamellar flattening.
Schematic illustration depicting the lamellar shape of each siRNA-treated cell. Arcs, straight lines, and pink circles indicate TAs, dSFs connecting to TAs at right angles, and FAs, respectively. Red and green correspond to NMIIA and NMIIB in the SF subtypes, respectively. TAs form via the association of NMIIA with actin filaments in the distal region of the lamella and are then transferred to the cell body. During centripetal flow, TAs link to FAs derived from the distal end of dSFs at both ends [30], as well as to dSFs connecting to TAs at right angles, and then NMIIB is incorporated into TAs. TAs do not form in NMIIA-KD cells. The flattened lamella is maintained by the contraction of TAs. The tension generated by this contraction is transmitted to FAs at the distal end of dSFs [32]. Thus, lamellar flattening is affected in both NMIIA-KD and NMIIB-KD cells due to the lack of TAs and the absence of functional TAs, respectively.

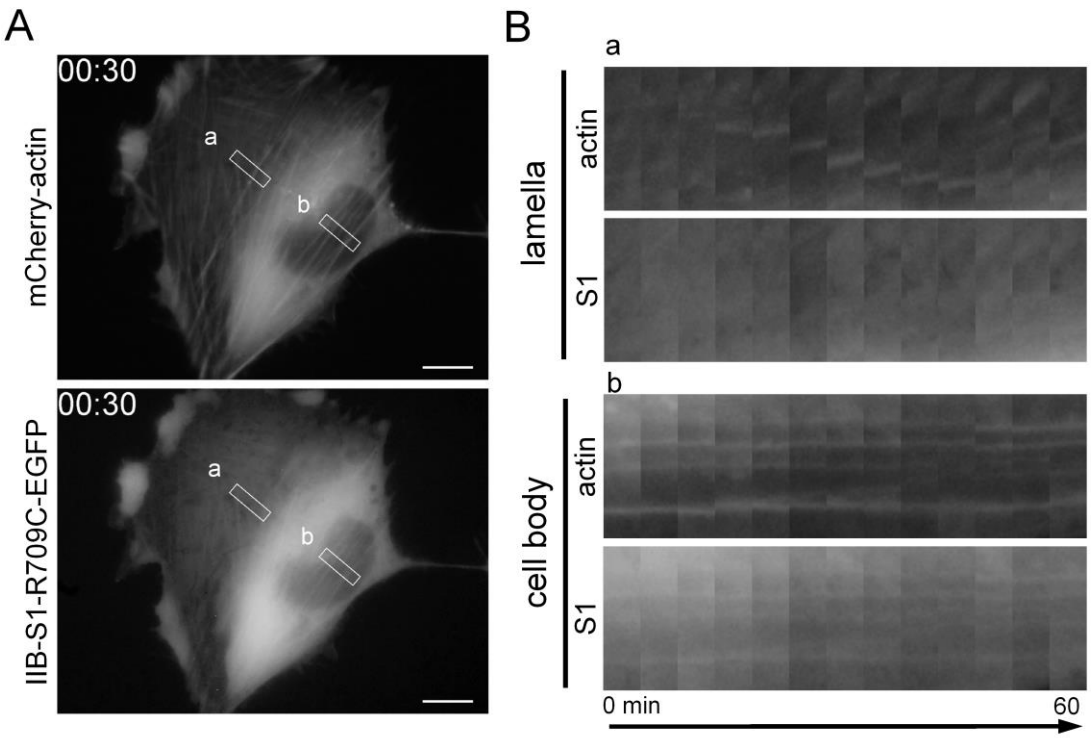

Figure 30. S1 probe binds to less mobile vSFs but not to mobile TAs.
(A) Still images showing exogenous mCherry-actin and S1 probe fluorescence in a live SV1 cell. (B) Kymographs generated from the boxed regions in panel A. Boxes a and b indicate the regions of TAs in the lamella and vSFs in the cell body, respectively. All images were captured using a conventional fluorescence microscope. Bar, 10 μm.

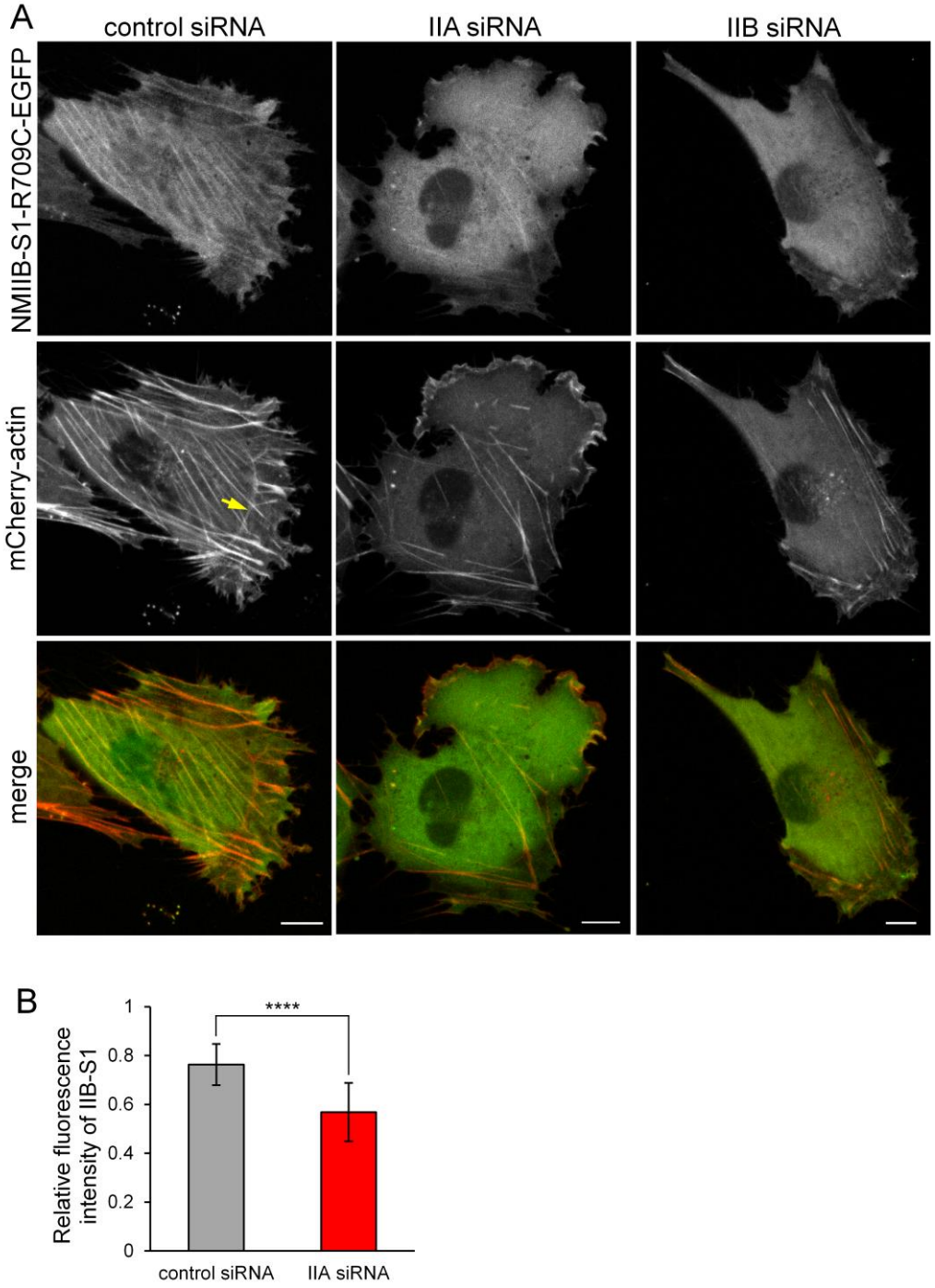

Figure 31. Both NMIIA and NMIIB are required for the normal organization of vSFs.
(A) SV1 cells treated with the indicated siRNAs were transfected with siRNA-insensitive S1 probe and mCherry-actin. Live cell images were captured using a confocal microscope. Bar, 10 μm. The yellow arrowhead points to a curved TA. Note that S1 probe did not bind to curved TAs. The fluorescence intensity of S1 probe relative to that of mCherry-actin in vSFs was lower in NMIIA-KD cells than in control cells. (B) The ratio of the fluorescence intensity of S1 probe to that of mCherry-actin in vSFs in control and NMIIA-KD cells. The relative fluorescence intensity of S1 probe in the SF area versus the control area was quantified and normalized by that of mCherry-actin using the RGB Measure plugin of ImageJ software. Data represent the mean ± SD from n = 25 SFs from five cells. ****$P < 0.00005$.

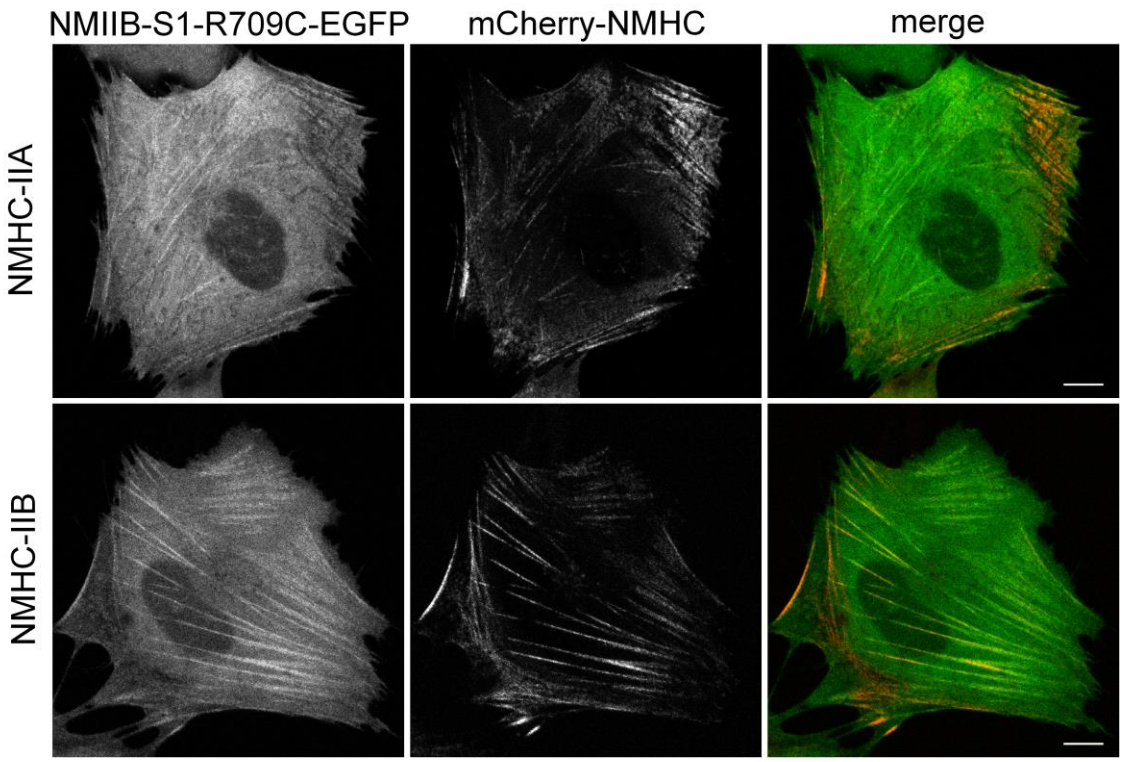

Figure 32. Distribution of mCherry-NMHC-IIs and S1 probe in SV1 cells.
SV1 cells were expressed with S1 probe and either mCherry-NMHC-IIA or mCherry-NMHC-IIB. Live cell images were captured using a confocal microscope. Bar, 10 μm.

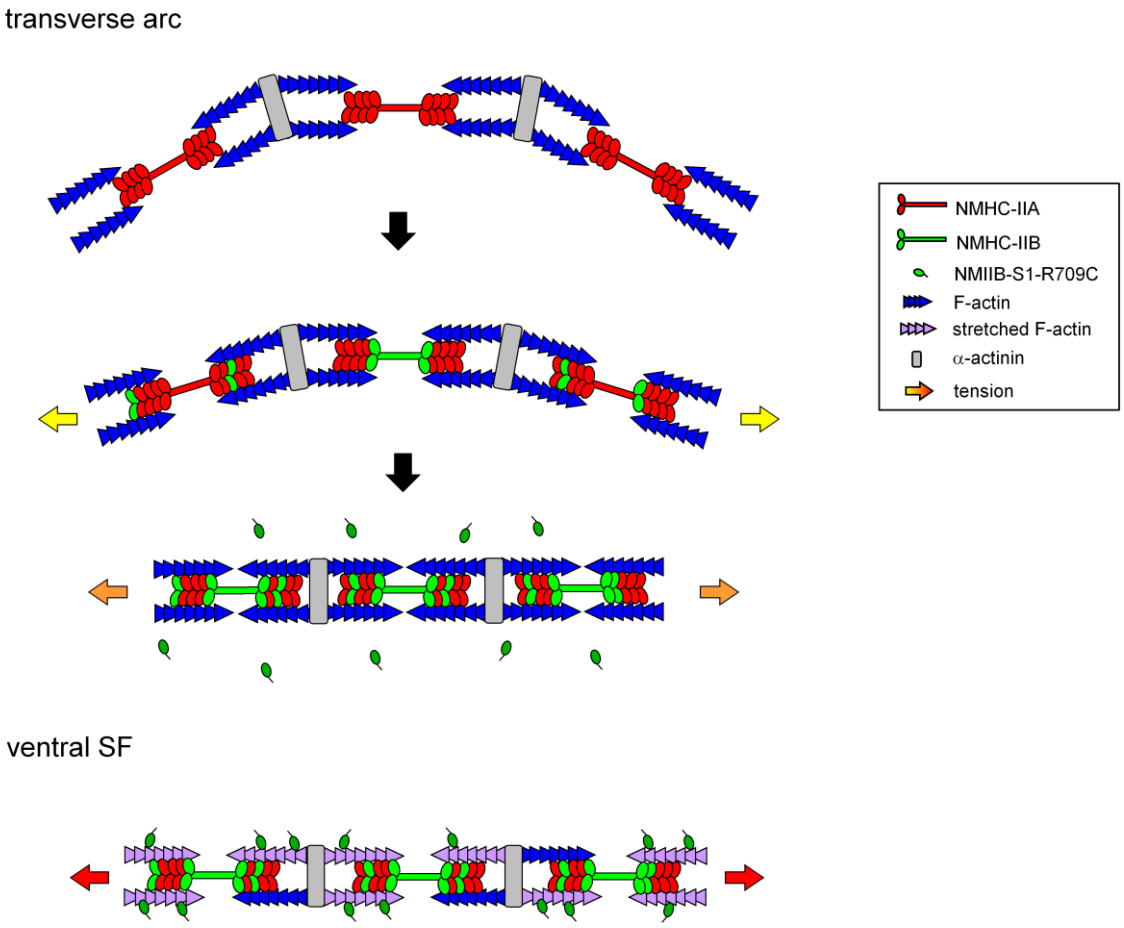

Figure 33. Schematic model of the organization of SF subtypes.
The key difference between TAs and vSFs is their contraction mode. Specifically, vSFs undergo isometric contraction (length remains constant), whereas TAs are shortened during centripetal flow. Therefore, if an equal load is applied to these structures, vSFs generate greater tension than TAs, resulting in the stretching of actin filaments, which is recognized by S1 probe.

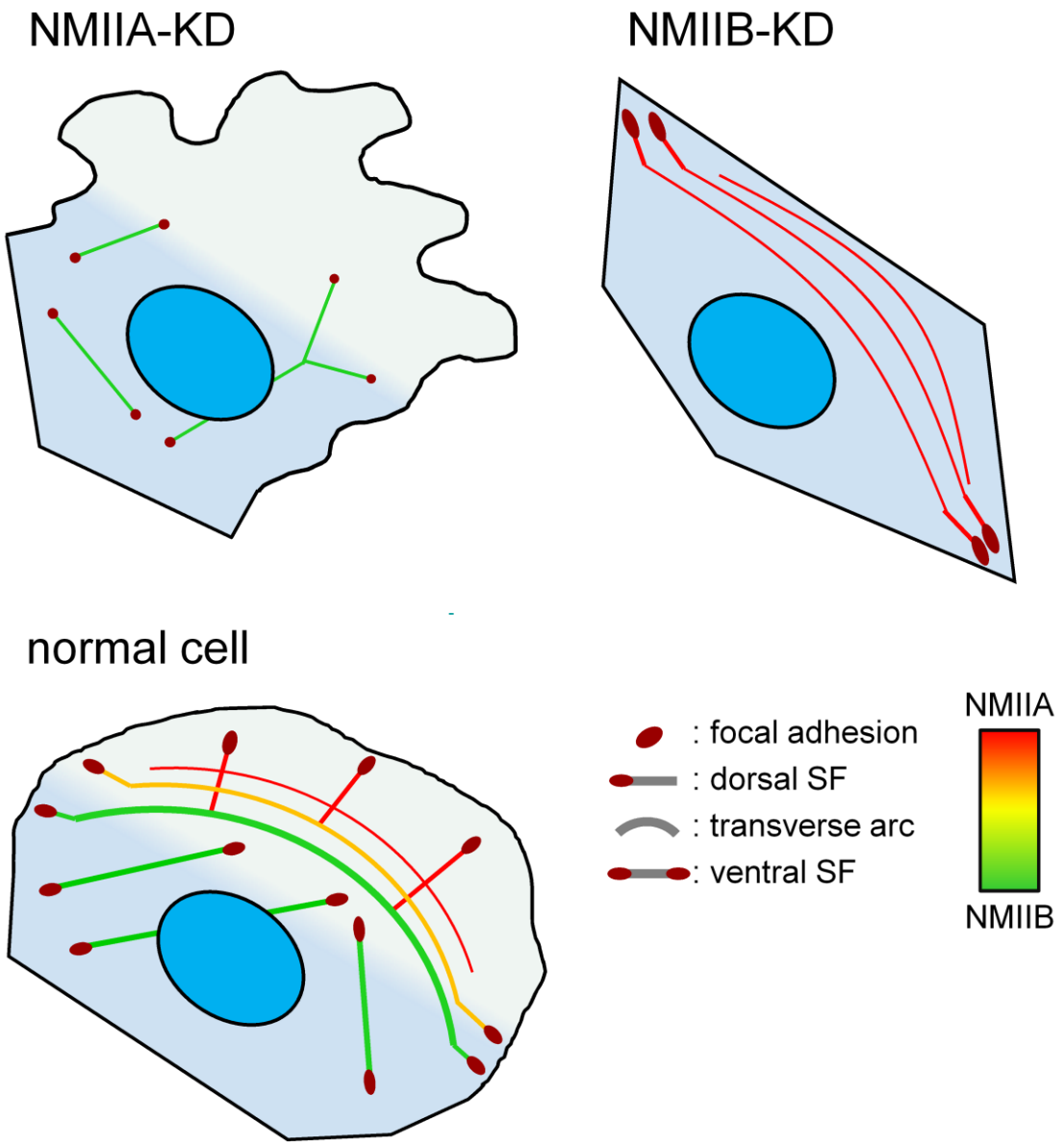

Figure 34. Localization of NMII isoforms in the SF subtypes.
Red and green line indicate regions where NMIIA and NMIIB preferentially localize, respectively. NMIIA KD caused loss of TAs in the lamella. The remaining vSFs were not likely to be proper structure. On the other hand, NMIIB KD caused loss of vSFs in the cell body and showed relatively uncurved TAs in the lamella.

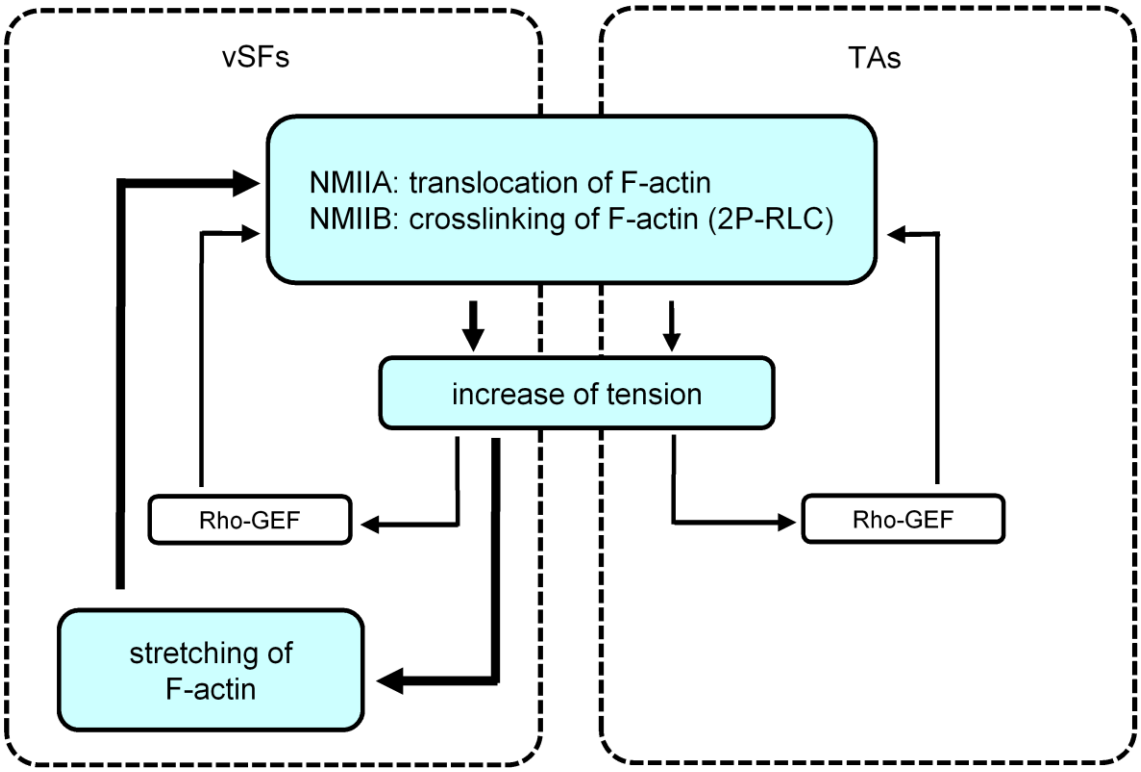

Figure 35. Proposed schematic model of the positive feedback loops of tension generated by the SF subtypes. In addition to the positive feedback loop regulated by Rho-GEF activation, there is another feedback loop that involves stretch-induced conformational changes of actin filaments in vSFs in cell bodies.

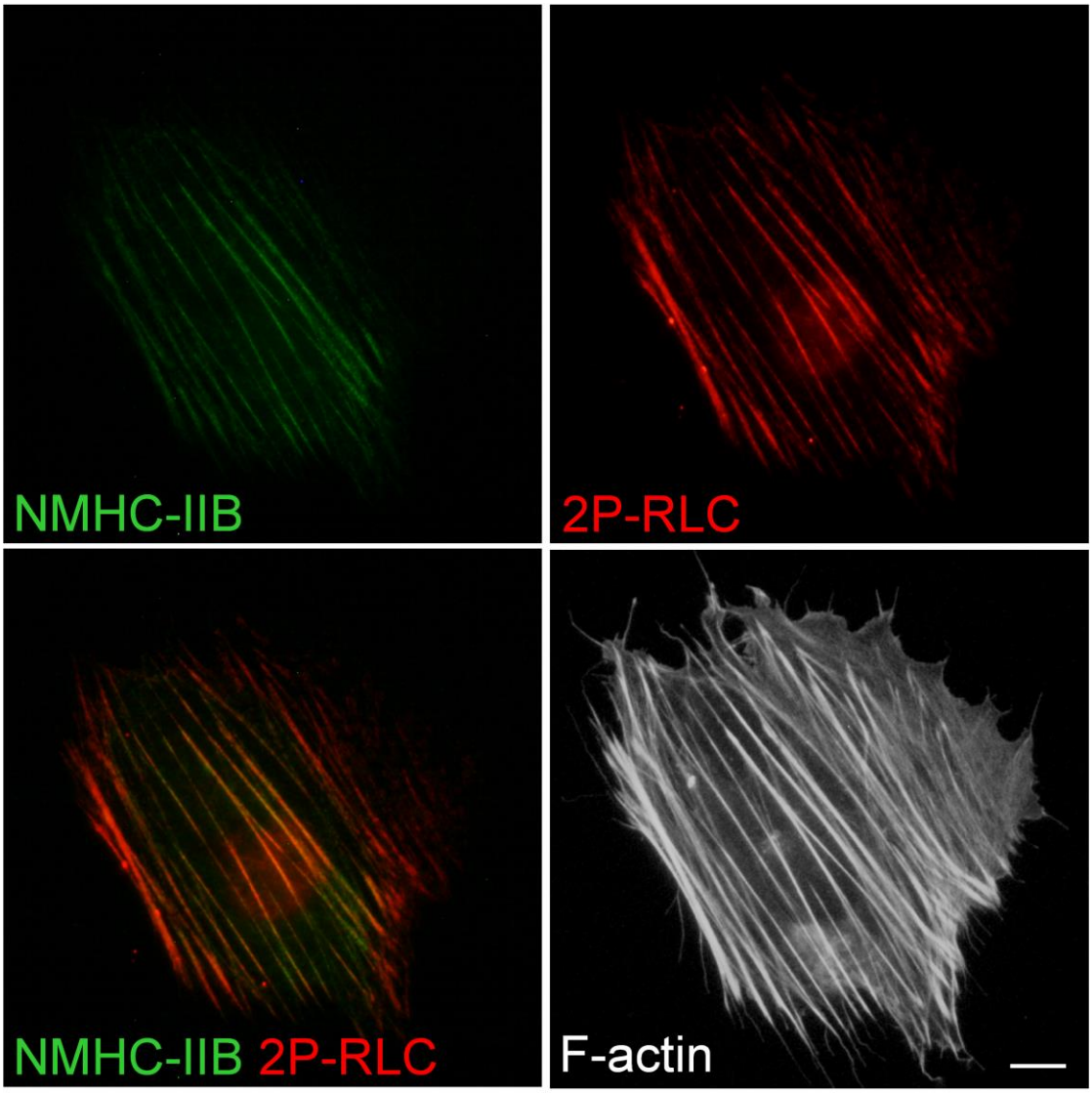

Figure 36. Another type of SV1 cells showing straight aligned SFs.
SV1 cells were fixed and stained with an Alexa Fluor 488-conjugated anti-MNHC-IIB polyclonal antibody (green), anti-2P-RLC polyclonal antibody (red), and Alexa Fluor 350-phalloidin (gray). Bar, 10 μm. The image was captured using a conventional fluorescence microscope. Note that NMIIB and 2P-RLC colocalized at straight aligned SFs.

Chapter 3: Distinct functions of NMIIA and NMIIB in intrinsic and directed migration of human embryonic lung fibroblasts

3-1: Abstract

NMII plays an essential role in directional cell migration. In this study, we investigated the roles of NMII isoforms (NMIIA and NMIIB) in the migration of human embryonic lung fibroblasts, which exhibit directionally persistent migration in an intrinsic manner. NMIIA-KD cells migrated unsteadily, but their direction of migration was approximately maintained. By contrast, NMIIB-KD cells occasionally reversed their direction of migration. Lamellipodium-like protrusions formed in the posterior region of NMIIB-KD cells prior to reversal of the migration direction. Moreover, NMIIB KD led to elongation of the posterior region in migrating cells, probably due to the lack of load-bearing stress fibers in this area. These results suggest that NMIIA plays a role in steering migration by maintaining stable protrusions in the anterior region, whereas NMIIB plays a role in maintenance of front-rear polarity by preventing aberrant protrusion formation in the posterior region. These distinct functions of NMIIA and NMIIB might promote intrinsic and directed migration of normal human fibroblasts.

3-2: Results

3-2-1: Normal human fibroblasts exhibited intrinsic and directed migration

While studying the migration of several types of fibroblasts, I noticed that normal fibroblasts, human lung embryonic fibroblasts (MRC-5, WI-38 and TIG-1 cells), were able to migrate in a directionally persistent manner for quite a long time (> 6 hours) compared to immortalized cells (MEF and SV1 cells) and cancer cells (U-2 OS cells) (Figure 37). These results imply normal human fibroblasts have some sort of mechanism to keep the high intrinsic directionality unlike immortalized cells.

3-2-2: NMII is required for directionally persistent migration

To elucidate the underlying molecular mechanism, we investigated the involvement of NMII using TIG-1 cells. Upon treatment with BBS, a NMII ATPase inhibitor, aberrant protrusions formed throughout TIG-1 cells and a long tail remained in the posterior region. (Figure 38, A and B). I studied migratory behavior of these cells by tracking the location of the nucleus marked with mCherry-tagged nuclear localization signal (NLS). Directional persistence was calculated as a ratio of D (distance between first point and last point) to T (total migration length). As this value is closer to 1, the cells have a tendency to maintain the direction of migration. Compared to DMSO-treated control cells, BBS-treated cells exhibited a decrease of directional persistence and an increase of migration rate (Figure 38, C and D). DMSO-treated control cells exhibited a proper

retraction of tail region, whereas BBS-treated cells failed to retract the tail and left the elongated tail in the posterior region (Figure 38F). These results indicate that ATPase activity of NMII is necessary for directionally persistent migration.

3-2-3: NMIIA and NMIIB play distinct roles for directionally persistent migration

Next, to elucidate how NMII isoforms contribute to this directional persistence, we knocked down each isoform individually. The level of NMHC-IIC was below the detection limit of immunoblotting in TIG-1 cells and other types of human embryonic lung fibroblasts (MRC-5 and WI-38 cells) (Figure 39A). Therefore, we examined the effects of KD of NMIIA and NMIIB. Immunoblot analysis confirmed the reduction of endogenous NMHC-IIA and NMHC-IIB isoform, resulting from the corresponding specific siRNA treatments (Figure 39, B and C). Based on the immunoblotting results, I roughly estimated that expression of NMHC-IIA was about 2.6-fold higher than that of NMHC-IIB in TIG-1 cells.

Control siRNA-treated cells exhibited intrinsic and directed migration (IDM) for a long duration (Figure 40, A and B). NMIIA-KD cells migrated unsteadily, but their direction of migration was approximately maintained (Figure 40, A and B). Unstable protrusions formed in the anterior region of NMIIA-KD cells. On the other hand, NMIIB-KD cells showed IDM, at least for a short duration, but they suddenly reversed their direction of migration (Figure 40, A and B), resulting in a decrease in directional persistence compared with control and NMIIA-KD cells (Figure 40C). These results suggest that NMIIA and NMIIB contribute to IDM of fibroblasts by steering migration and maintaining front-rear polarity, respectively. NMIIB-KD cells migrated about 2-fold faster than control cells (Figure 40D). This increase is comparable to that observed for embryonic fibroblasts derived from NMIIB-knockout mice [54]. The increased migration speed of TIG-1 cells upon BBS treatment (Figure 38E) is likely due to the inhibition of NMIIB activity. NMIIB might play a role in deceleration of cell migration.

3-2-4. NMIIB prevents formation of lamellipodium-like protrusions in the posterior region

Focusing on the tail region of migrating cells, we found that the tail could retract in NMIIA-KD cells (Figure 41A), but not in BBS-treated cells (Figure 38F). This is probably because adhesion to the substrate is weakened in the tail region [37] and active NMIIB is present in this region, as mentioned later. Lamellipodium-like protrusions formed in the posterior region of NMIIB-KD cells prior to reversal of the migration direction (Figure 41). Positioning of the microtubule-organizing center (MTOC) at the anterior side of the nucleus establishes front-rear polarity in migrating fibroblasts on a 2D surface [91]. The positioning of the MTOC in migrating TIG-1 cells was consistent with this finding (Figure 42A). Even during the unsteady migration of NMIIA-KD cells, the MTOC reoriented to the anterior side of the nucleus (Figure 42B). However, when the

migration direction of NMIIB-KD cells was reversed, the MTOC did not reorient toward the new anterior side (Figure 42B). These results imply that formation of lamellipodium-like protrusions in the posterior region, rather than MTOC repositioning, triggers the reversal of front-rear polarity in NMIIB-KD cells. NMIIB can likely maintain front-rear polarity by preventing formation of lamellipodium-like protrusions in the posterior region.

3-2-5: NMIIA and NMIIB maintain the shapes of the anterior and posterior regions, respectively

Migrating TIG-1 cells had a highly polarized shape reminiscent of a broom (e.g., see control siRNA-treated cells in Figure 43A). This polarized shape could be important for IDM of fibroblasts. Next, we examined the involvement of the localization of each NMII isoform in the shape of TIG-1 cells. In control cells, NMIIA was mostly localized throughout the cell and NMIIB colocalized with NMIIA, except in the anterior region (Figure 43A), as previously demonstrated in other cell types [9,53,55,82,92]. Both isoforms were particularly enriched at the lateral sides of the cell body, and the level of NMIIA was very low in the thin tail, except at the very end. Similar findings were made in living cells expressing fluorescent NMII isoforms (Figure 43B). NMIIA KD led to the formation of multiple protrusions in the anterior region, resulting in an increase in cell area (Figure 43C). This morphological phenotype is similar to that of NMIIA-null mouse embryonic stem cells [37]. On the other hand, NMIIB KD led to elongation of the posterior cell body and tail, even though NMIIA was localized here, resulting in an increase in the axis ratio (Figure 43D).

3-2-6: Rescue of cell morphology by re-expressing respective NMII isoform

To determine whether the observed defects are due to the lack of the specific NMII isoform, I performed KD-rescue experiments (Figure 44). The morphological defect of NMIIA-KD cells (i.e., formation of aberrant protrusions) was mostly rescued by exogenous NMHC-IIA, but not NMHC-IIB (Figure 44, B and D). On the other hand, the morphological defect of the posterior region (i.e., elongation of the cell body) in NMIIB-KD cell was mostly rescued by NMHC-IIB, but not NMHC-IIA (Figure 44, C and E). These results indicate each morphological defect was rescued by exogenous expression of the knocked down NMII isoform, but not by exogenous expression of the other isoform.

Next, to identify the region of NMII isoforms responsible for this rescue of morphological defects, I examined the effects of exogenous chimeric NMIIs on cell shape (Figure 44). Localization of NMII isoforms in migrating cells is directed by the C-terminal tail region of their heavy chain subunits [82], which contain essential domains for filament formation, such as assembly competence domains [93] and nonhelical tailpieces [94]. NMIIB/IIA-tail, but not

NMIIA/IIB-tail, localized in the anterior region and mostly rescued the morphological defect of the anterior region in NMIIA-KD cells (Figure 44, B and D), indicating that the anterior region has a normal shape if either of the NMII isoforms can localize there. Meanwhile, the morphological defect of the posterior region in NMIIB-KD cells was not completely rescued by either chimeric NMII (Figure 44, C and E), indicating that intact NMIIB is required to maintain the shape of the posterior region.

3-2-7: NMIIB is required for maintenance of 2P-RLC of NMII in posterior region

To determine why the posterior region is elongated in NMIIB-KD cells, we investigated the extent of NMII activation (i.e. phosphorylation status of RLCs). Phosphorylation of RLC at Ser19 (1P-RLC) promotes actin-activated Mg^{2+}-ATPase activity and filament formation, and this is further enhanced by diphosphorylation at Thr18 and Ser19 (2P-RLC) [2,3]. Immunoprecipitation analysis revealed that both NMIIA and NMIIB contained 1P-RLC and 2P-RLC (Figure 45A). NMIIA KD resulted in much decrease of total amount of RLC, probably because the expression of NMHC-IIA is about 2.6-fold higher than that of NMHC-IIB in TIG-1 cells (Figure 45, B and C). The phosphorylation status of RLCs were almost unchanged by NMIIA KD, whereas 2P-RLC was decreased by NMIIB KD. Immunofluorescence showed that both 1P-RLC and 2P-RLC were present at the lateral sides of the posterior region in control cells, and that 2P-RLC, but not 1P-RLC, was absent from this region in NMIIB-KD cells (Figure 46). This suggests that NMIIB is required to maintain 2P-RLC in this region.

3-2-8: Role of NMIIB in tension generation at posterior region

We suspected that elongation of the posterior region might be due to a lack of load-bearing stress fibers. We utilized S1 probe (NMIIB-S1-R709C-EGFP) to detect load-bearing stress fibers, which contain stretched actin filaments, in migrating cells. S1 probe accumulated at lateral sides of the posterior region when this region was elongated during migration (Figure 47), indicating that actin filaments in the posterior region are stretched. Similar findings were made in control siRNA-treated cells and NMIIA-KD cells; however, S1 probe was diffusely distributed in NMIIB-KD cells (Figure 48), suggesting that actin filaments in the posterior region are no longer stretched in the absence of NMIIB. These results suggest that NMIIB generates tension needed to bear load in posterior stress fibers of migrating cells. These load-bearing stress fibers may prevent formation of aberrant protrusions in the posterior region, resulting in IDM (Figure 49).

3-3: Discussion

In this chapter, I examined the roles of NMII isoforms in IDM of normal fibroblasts. KD experiments revealed that NMIIA and NMIIB differentially contribute to IDM by controlling the

shapes of the anterior and posterior regions, respectively.

Cell migration is steered by the proper formation of protrusions at the leading edge [95]. NMII in lamellae is responsible for proper advancement of the leading edge [28]. NMIIA contributes to form proper protrusion in the anterior region by decreasing Rac1 activity [37]. Maintenance of low Rac1 activity induces IDM in a variety of cells [51]. The morphological defect (i.e., aberrant protrusion formation) of NMIIA-KD cells was restricted to the anterior region (Figure 40), whereas aberrant protrusions formed throughout BBS-treated cells (Figure 38). Consequently, directional persistence was decreased less in NMIIA-KD cells than in BBS-treated cells (Figures 37 and 39). In NMIIA-KD cells, active NMIIB remaining in the posterior region could block the formation of membrane protrusions.

The main morphological defect of NMIIB-KD cells was elongation of the posterior region (Figure 43). Actin filaments in lateral stress fibers located in the posterior region would be in a stretched conformation judging based on the binding of the S1 probe (Figure 48), indicating that these stress fibers can bear a high mechanical load and become more elastic upon NMIIB KD. This change might lead to elongation of cell shape in the posterior region. Moreover, this defect was rescued by exogenous expression of NMIIB (Figure 44). NMIIB has a higher duty ratio than NMIIA (i.e., the NMIIB motor head spends longer in the strong actin-binding states during the ATPase cycle), indicating that NMIIB can function in crosslinking (structural property) of actin filaments [2,3,16]. This behavior of NMIIB may be required for resistance against the high mechanical load applied to stress fibers in the posterior region. Uyeda *et al*. proposed that myosin II preferentially binds to stretched actin filaments in a mechanical positive feedback manner in *Dictyostelium* cells [58]. NMIIB might be essential for this positive feedback loop in mammalian cells.

The most surprising result of this study was the reversal of migration direction in NMIIB-KD cells (Figure 40). The first recognizable event in this process was the formation of lamellipodium-like protrusions in the posterior region (Figure 41). Vicente-Manzanares *et al*. reported that NMIIB creates a rear in migrating cells [55] and that exogenous diphosphomimetic RLC (T18D, S19D) prevents Rac1 activation in the area corresponding to the posterior region [39]. Based on these results, they proposed that NMII containing 2P-RLC can prevent formation of abnormal protrusions in the posterior region. Actually, NMIIB can directly bind to Rac-GEFs (βPIX and Tiam1) to suppress their activities [96]. In this study, I directly demonstrated that NMIIB KD reduced the endogenous level of 2P-RLC in the posterior region (Figure 46) and induced the formation of lamellipodium-like protrusions, which supports their hypothesis. Guo and Wang demonstrated that local application of cytochalasin D (an inhibitor of actin polymerization) to the posterior region induces the reversal of migration direction in immortalized fibroblasts (NIH-3T3) on micropatterned strips (i.e., a 1D surface) [97]. This finding strengthens

the hypothesis that the posterior actin cytoskeleton containing NMIIB helps to prevent protrusion formation in the tail. The direction of migration was not reversed in BBS-treated cells (Figure 38), suggesting that active NMIIA remaining in the posterior region is partly responsible for this phenomenon. Indeed, NMIIA containing 1P-RLC remained localized throughout NMIIB-KD cells (Figures 42 and 45). In NMIIB-KD cells, NMIIA may promote formation of protrusions in the posterior region in the same manner as in the anterior region [27,37], and this likely triggers the reversal of migration direction. In other words, NMIIB may play a critical role in IDM by preventing formation of aberrant protrusions. The MTOC was positioned to the anterior side of the nucleus in migrating TIG-1 cells (Figure 42A), consistent with findings in other types of fibroblasts [91]. However, the MTOC did not reorient to the anterior region at the initial stage of the reversal of migration direction in NMIIB-KD cells (Figure 42B). Recently, Zhang *et al*. proposed that the localization of the MTOC relative to the cell centroid, rather than to the nucleus, is important for the migration direction of mesenchymal cells and that positioning of the MTOC in the posterior region establishes front-rear polarity [98]. Similar events may occur during the reversal of the migration direction in NMIIB-KD cells. A proposed scheme for the roles of NMIIA and NMIIB in IDM was represented in Figure 50.

In chapter 2, I showed that exogenous NMIIB was able to localize near the leading edge and rescue the formation of TAs in the NMIIA-KD SV1 cells, but not in NMIIB-KD cells which express the endogenous NMIIA. These results imply that exogenous excess NMIIB could become to reach the distal end of lamella, when the endogenous NMIIA molecules are depleted by KD. However, in this chapter, I showed that exogenous NMIIB was not able to rescue the morphological defect in NMIIA-KD TIG-1 cells due to the restricted localization of exogenous NMIIB to the posterior region. These differences might be due to the differences in cell morphological polarity between normal and immortalized fibroblasts. TIG-1 cells exhibit a highly polarized shape like a broom, whereas SV1 cells exhibit a relatively round shape like a fish scale. Probably because the establishment of front-rear polarity in migrating TIG-1 cells is more obvious than that of in SV1 cells, both of exogenous and endogenous NMIIB was not able to reach the distal region in the cell front and failed to rescue the anterior morphological defect in NMIIA-KD cells. The highly polarized cell shape might affect the dynamics and behavior of NMII molecules. It would be interesting to clarify the reason why normal and immortalized fibroblasts exhibit different shapes and migration styles. However, Shutova *et al*. recently reported that the ratio of expression levels between NMIIA and NMIIB is important for the anterior localization of NMIIB in REF-52 fibroblasts and COS-7 cells: They showed that exogenous expression of NMIIA promotes the dynamics of NMIIB and allowed NMIIB to reach the distal end of lamella via the formation of heterogeneous filaments consisting of both isoforms [90]. This is another case concerning the NMIIB localization in the cell. These differences might be caused by not only cell

polarity level but the different spatio-temporal signaling mechanisms for the activation of NMII isoforms and the formation or stabilization of their filaments among the cell lines. It was reported that Rho-Kinase and MLCK work in the center and periphery of the cell, respectively [77]. It was also suggested that Rho kinase and MLCK preferentially regulate NMIIA and NMIIB, respectively [35,42]. Moreover, the phosphorylation of the nonhelical tailpiece, C-terminal end region of MHC, regulates the filament formation of NMIIs [2,3]. The locations and degrees of RLC and MHC phosphorylation could be different among the cell lines, which would be expected to clarify in future work.

3-4: Conclusion

In this chapter, I clarified the roles of each NMII isoform in the anterior and posterior regions of normal fibroblasts during IDM. We propose that NMIIA controls the proper formation of protrusions in the anterior region to steer migration, whereas NMIIB prevents the formation of protrusions in the posterior region to maintain front-rear polarity (Figure 51).

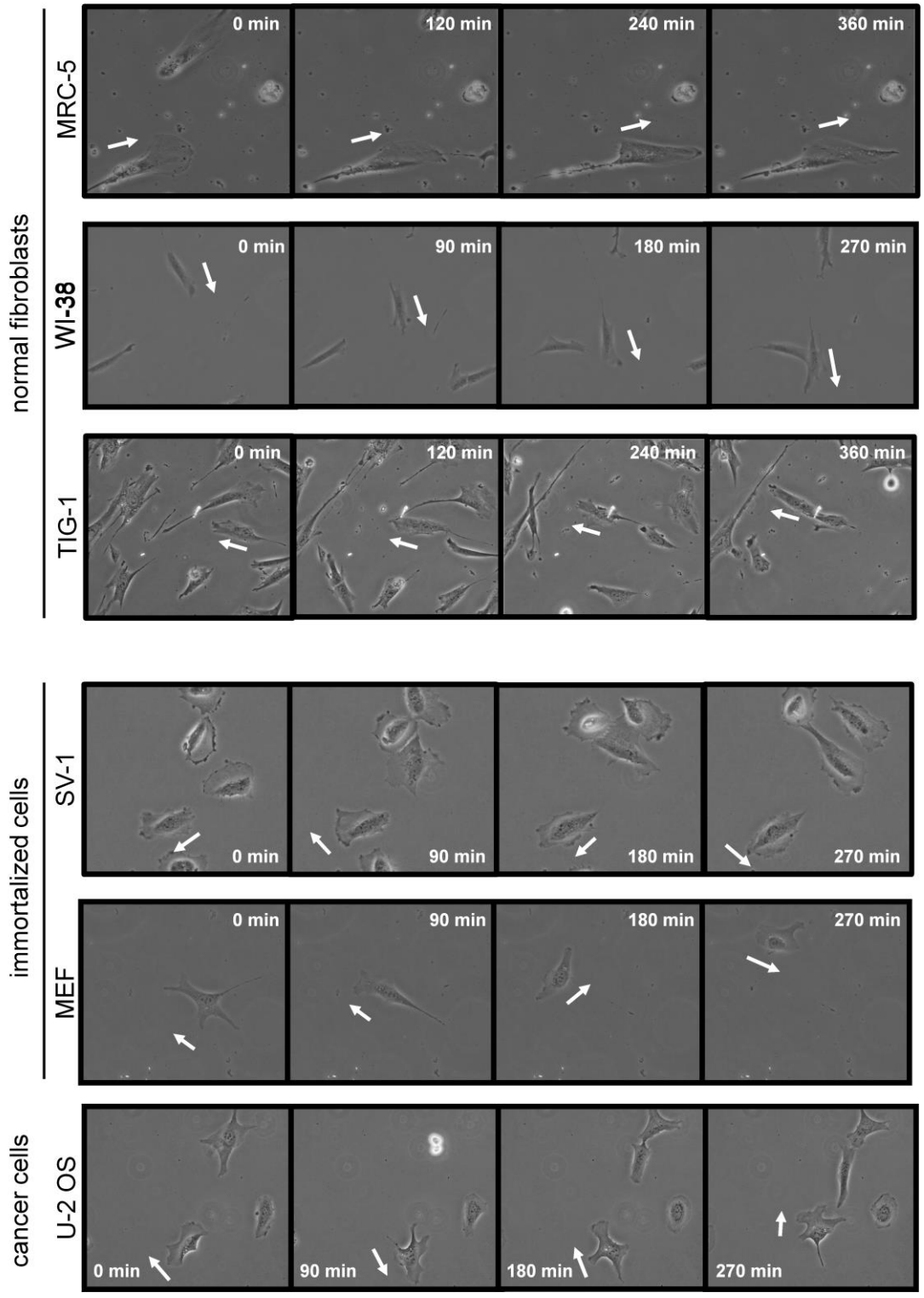

Figure 37. Migration style of various cell types.
Time series of images showing migration style of various cells. Note that immortalized cells (MEF and SV1 cells) and cancer cells (U-2 OS cells) showed random migration, whereas normal human fibroblasts (TIG-1, WI-38 and MRC-5 cells) showed directionally persistent migration.

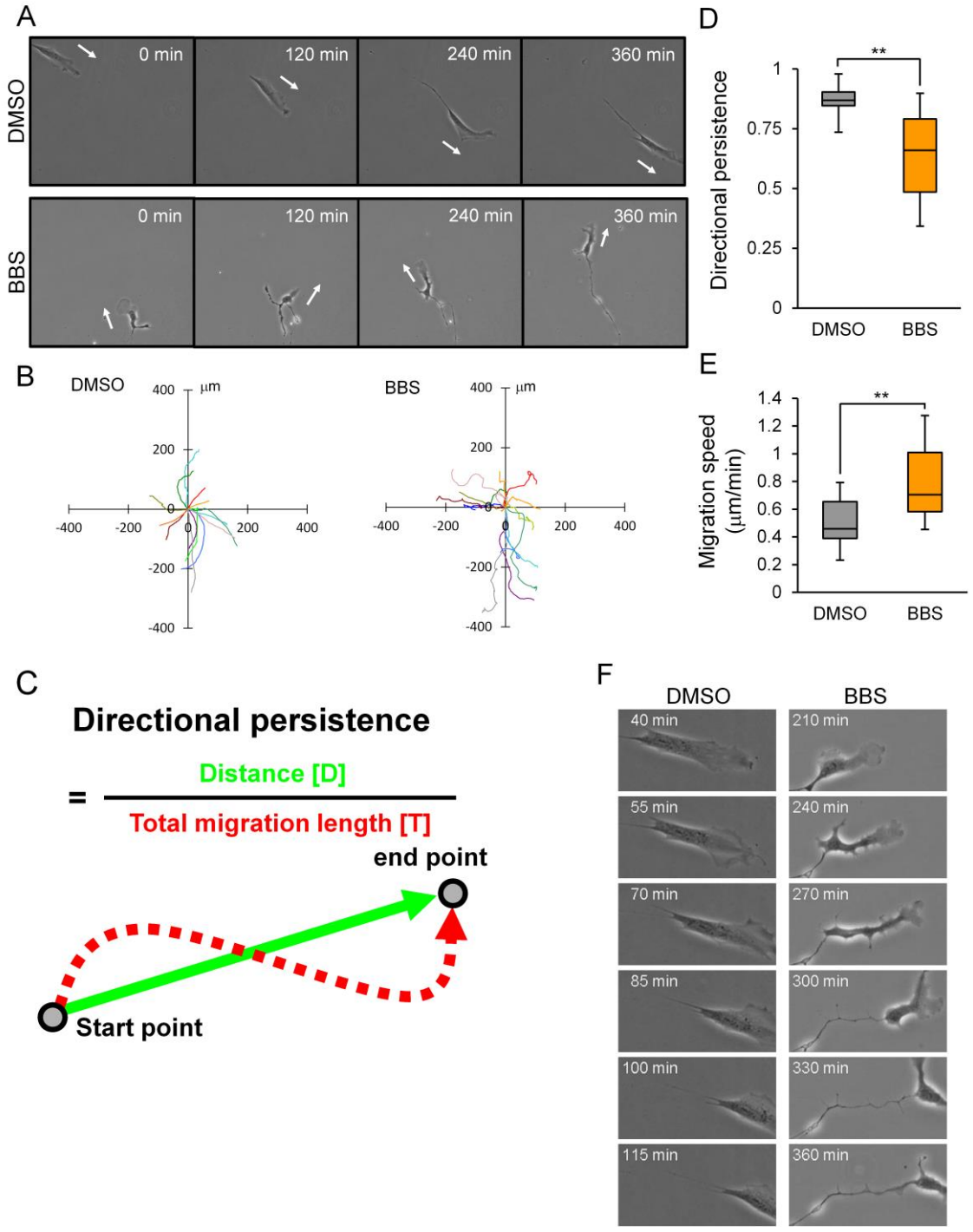

Figure 38. Effect of inhibition of NMII on migration of TIG-1cells.

(A) Time series of images showing migration of DMSO-treated (control) and BBS-treated TIG-1 cells. TIG-1 cells were treated with 0.1% DMSO (control) or 50 μM (±)-BBS. White arrows indicate the direction of migration. (B–E) Migration paths (B), directional persistence (D), and migration speed (E) of DMSO- and BBS-treated cells (n = 14 cells/condition). The migration path was determined by tracking the nucleus visualized with mCherry-NLS (B). Directional persistence was calculated as the direct distance from the start point to the end point divided by the total path distance (C, D). $^{**}P < 0.005$. (F) Time series of images showing morphological changes in the posterior region of DMSO-treated (control) and BBS-treated cells.

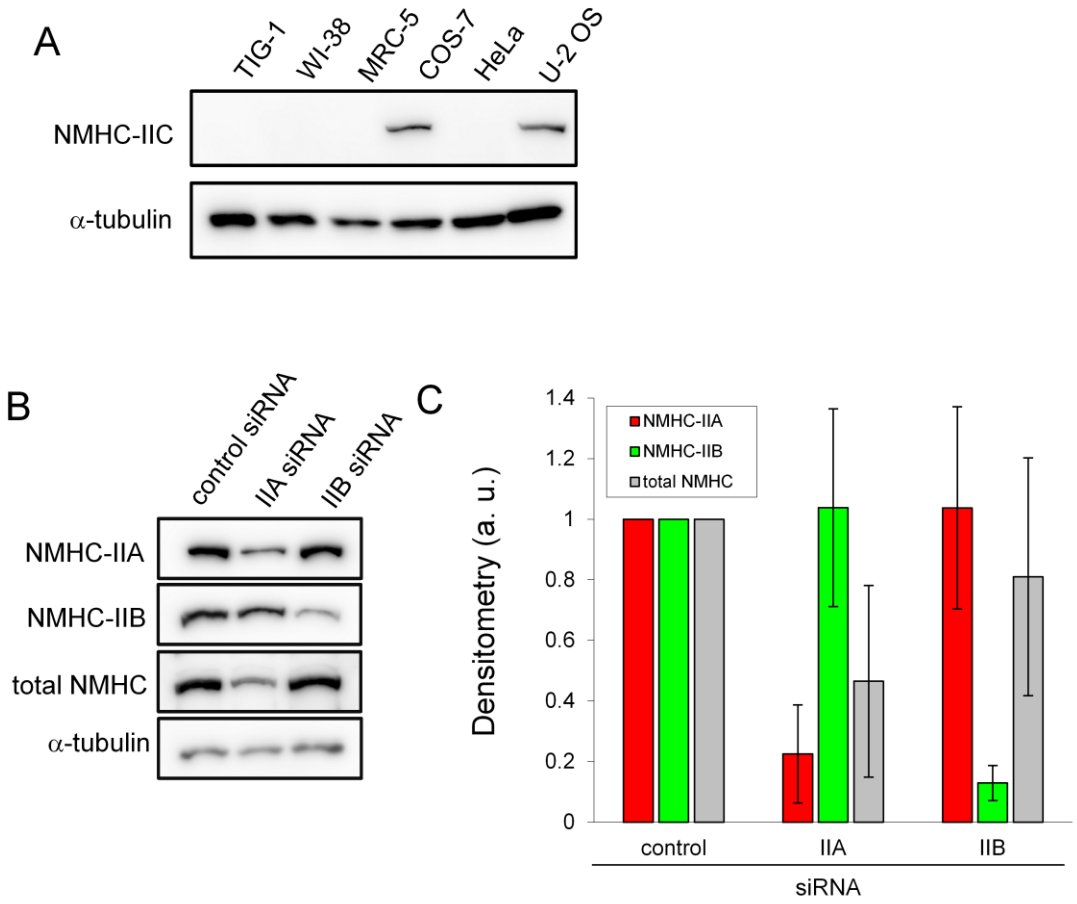

Figure 39. Expression of NMII isoforms in TIG-1 cells.
(A) Immunoblot showing expression of NMHC-IIC in the indicated cells. (B) Immunoblots showing the KD efficiency of NMHC-IIA and NMHC-IIB in the indicated siRNA-treated cells. Total NMHC-II was detected with an anti-myosin II (pan reactive) antibody. α-tubulin was used as a loading control. (C) Expression levels of NMHC-IIA and NMHC-IIB are represented as values normalized to those in control siRNA-treated cells. Data represent the mean ± SD from four independent experiments. *$P < 0.05$, **$P < 0.005$, ***$P < 0.0005$. The relative expression ratio of NMHC-IIA and NMHC-IIB was roughly estimated as follows. In NMIIA-KD cells, the remaining total amount of NMHC-II (T; 0.47) is the sum of the remaining NMHC-IIA (A; 0.23) and NMHC-IIB (B; 1.04) (i.e., 0.47T = 0.23A + 1.04B). In NMIIB-KD cells, the remaining total amount of NMHC-II (T; 0.81) is the sum of the remaining NMHC-IIB (B; 0.13) and NMHC-IIA (A; 1.04) (i.e., 0.81T = 0.13B + 1.04A). By solving the two equations, we estimated that expression of NMHC-IIA was about 2.6-fold higher than that of NMHC-IIB in TIG-1 cells.

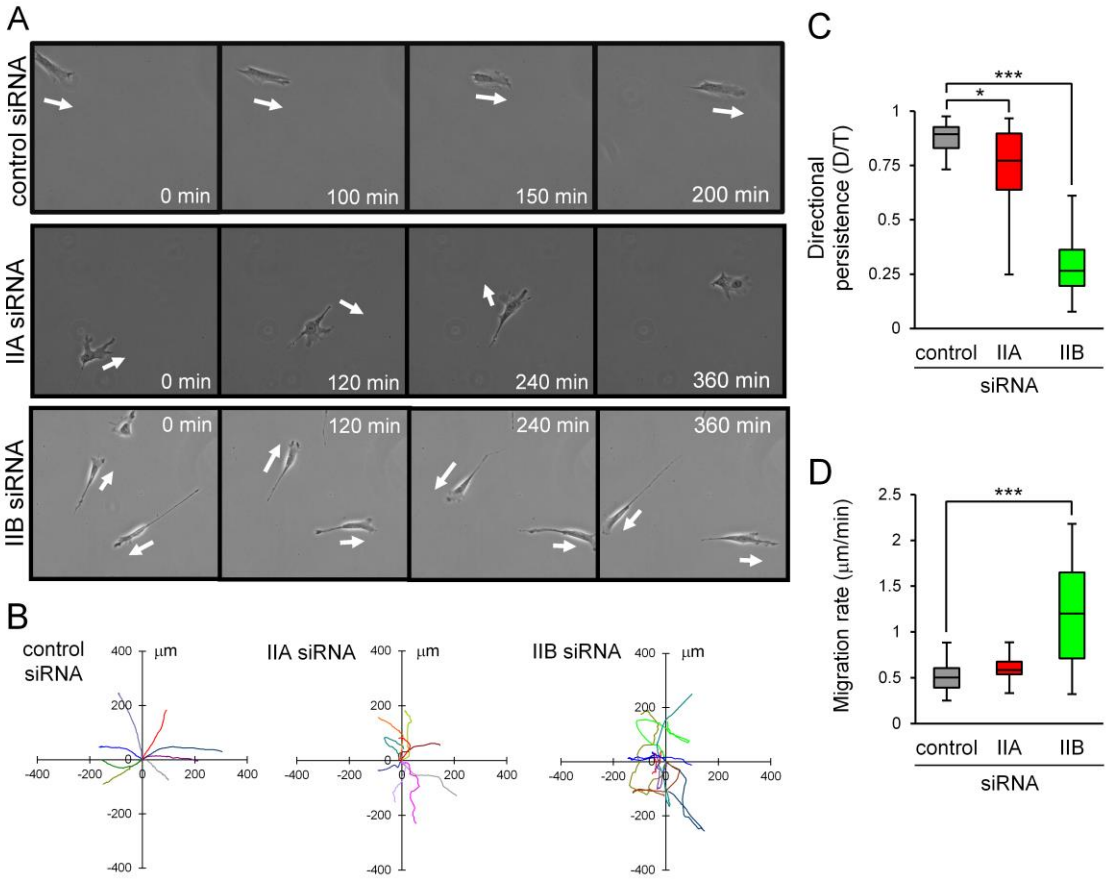

Figure 40. Effects of KD of each NMII isoform on directional migration.

(A) Time series of images showing the migration of the indicated siRNA-treated TIG-1 cells. White arrows indicate the direction of migration. (B–D) Migration paths (B), directional persistence (C), and migration speed (D) of cells treated with each siRNA (n > 15 cells/condition). The migration path was determined by tracking the nucleus visualized with mCherry-NLS. The paths of eight representative cells are shown by different colors (B). *P < 0.05, ***P < 0.0005.

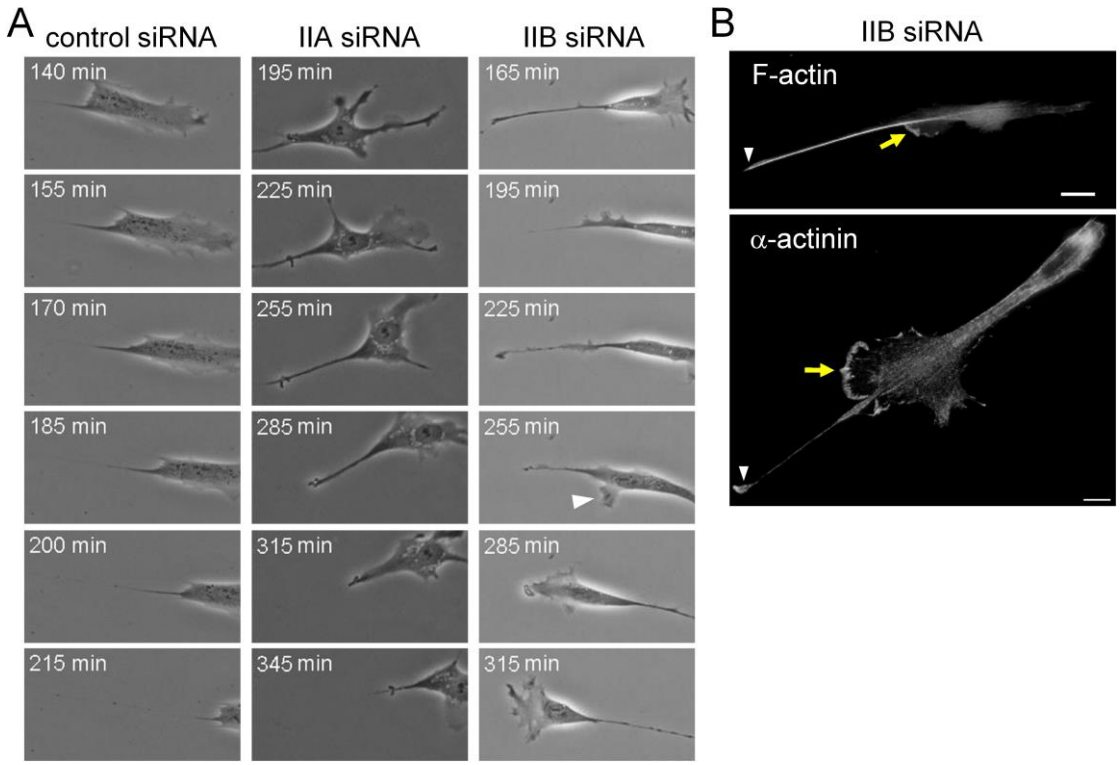

Figure 41. Effects of KD of each NMII isoform on dynamics of the tail region.
(A) Time series of images showing morphological changes in the posterior regions of the indicated siRNA-treated cells. The white arrowhead indicates protrusions from the posterior region of a NMIIB-KD cell. (B) Immunofluorescence images of the posterior region of NMIIB-KD cells. F-actin and α-actinin were stained with TRITC-phalloidin and an anti-α-actinin polyclonal antibody, respectively. Yellow arrows indicate protrusions from the posterior region. White arrowheads indicate the edge of the original tail. Bar, 10 μm.

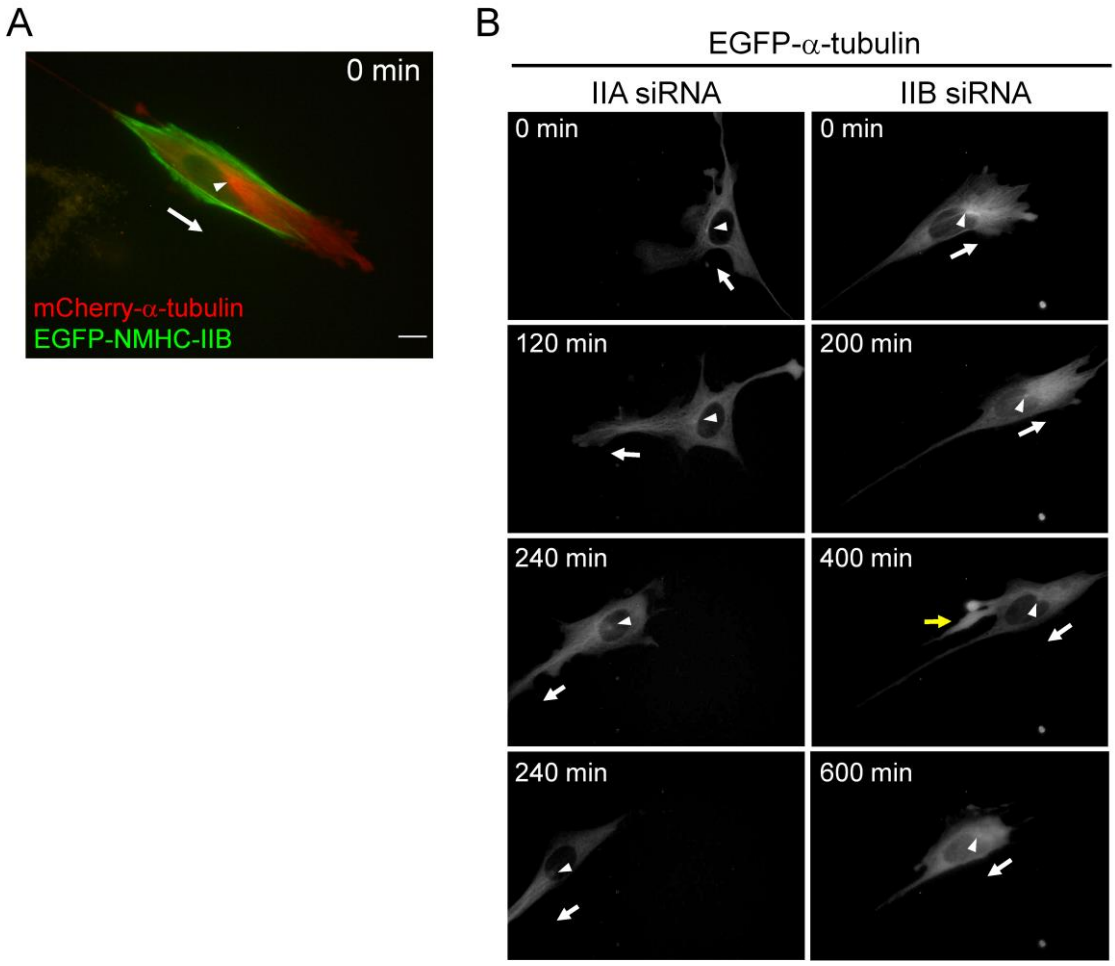

Figure 42. Orientation of the MTOC in migrating TIG-1 cells.
(A) A still image showing a live migrating TIG-1 cell expressing mCherry-α-tubulin and EGFP-NMHC-IIB. The white arrow indicates the direction of migration. The white arrowhead indicates the position of the MTOC, which was detected as a bright spot of mCherry-α-tubulin fluorescence. Bar, 10 μm. (B) Time series of images showing migrating NMIIA-KD and NMIIB-KD TIG-1 cells expressing EGFP-α-tubulin, respectively. White arrows indicate the direction of migration. White arrowheads indicate the position of the MTOC, which was detected as a bright spot of mCherry-α-tubulin fluorescence. The yellow arrow indicates aberrant protrusions from the posterior region of a NMIIB-KD cell.

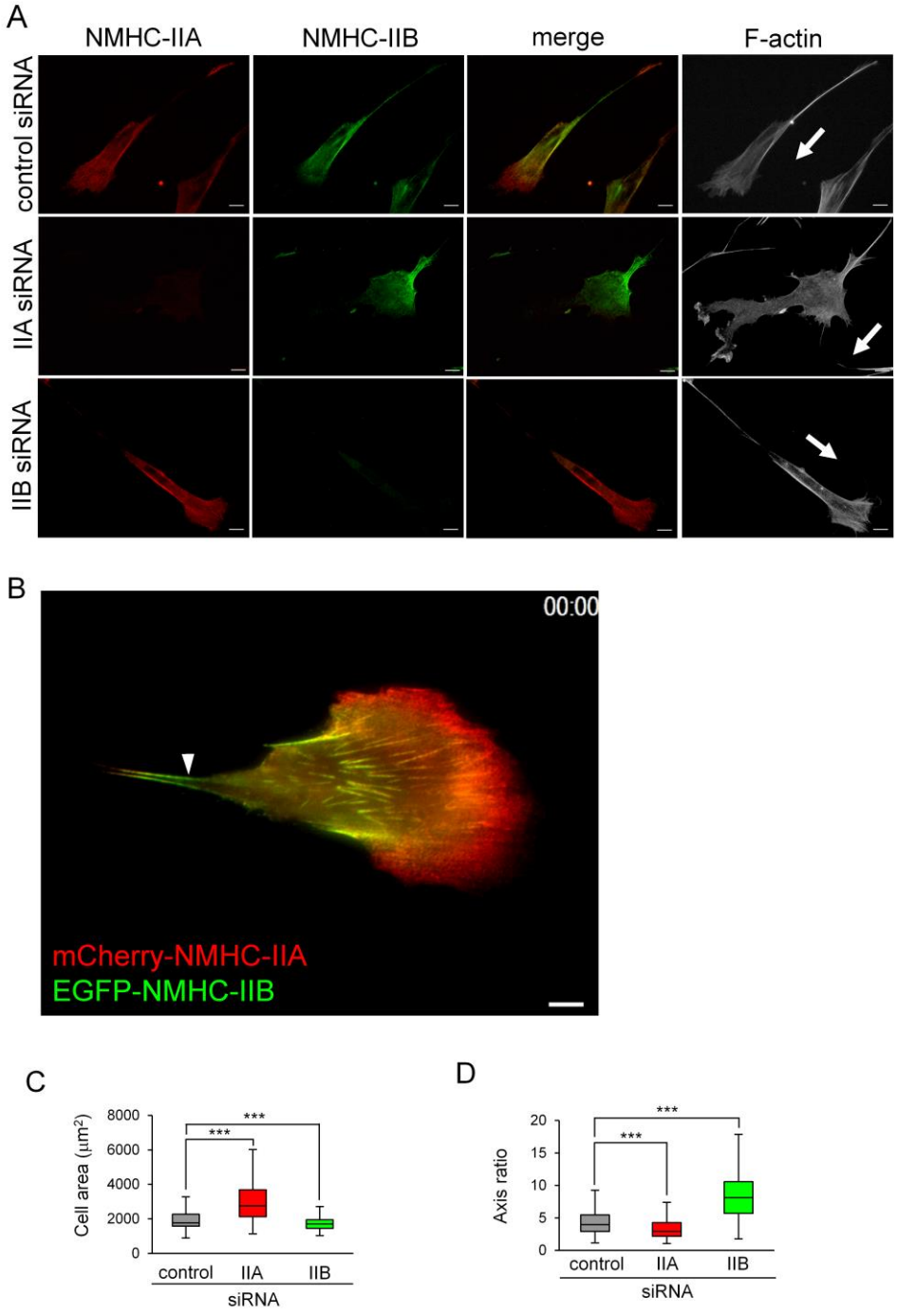

Figure 43. Effects of KD of each NMII isoform on maintenance of cell shape during migration.
(A) Direct immunofluorescence of NMIIA and NMIIB in the indicated siRNA-treated TIG-1 cells. White arrows indicate the expected direction of migration. F-actin was stained with Alexa Fluor 350-conjugated phalloidin. (B) A still image showing exogenous mCherry-NMHC-IIA and EGFP-NMHC-IIB fluorescence in a live TIG-1 cell. The white arrowhead indicates the accumulation of NMIIB in the stretched tail region. (C and D) Cell area (C) and axis ratio (major axis/minor axis) (D) of the indicated siRNA-treated cells (n > 140 cells/condition). ***$P < 0.0005$. Bar, 10 μm.

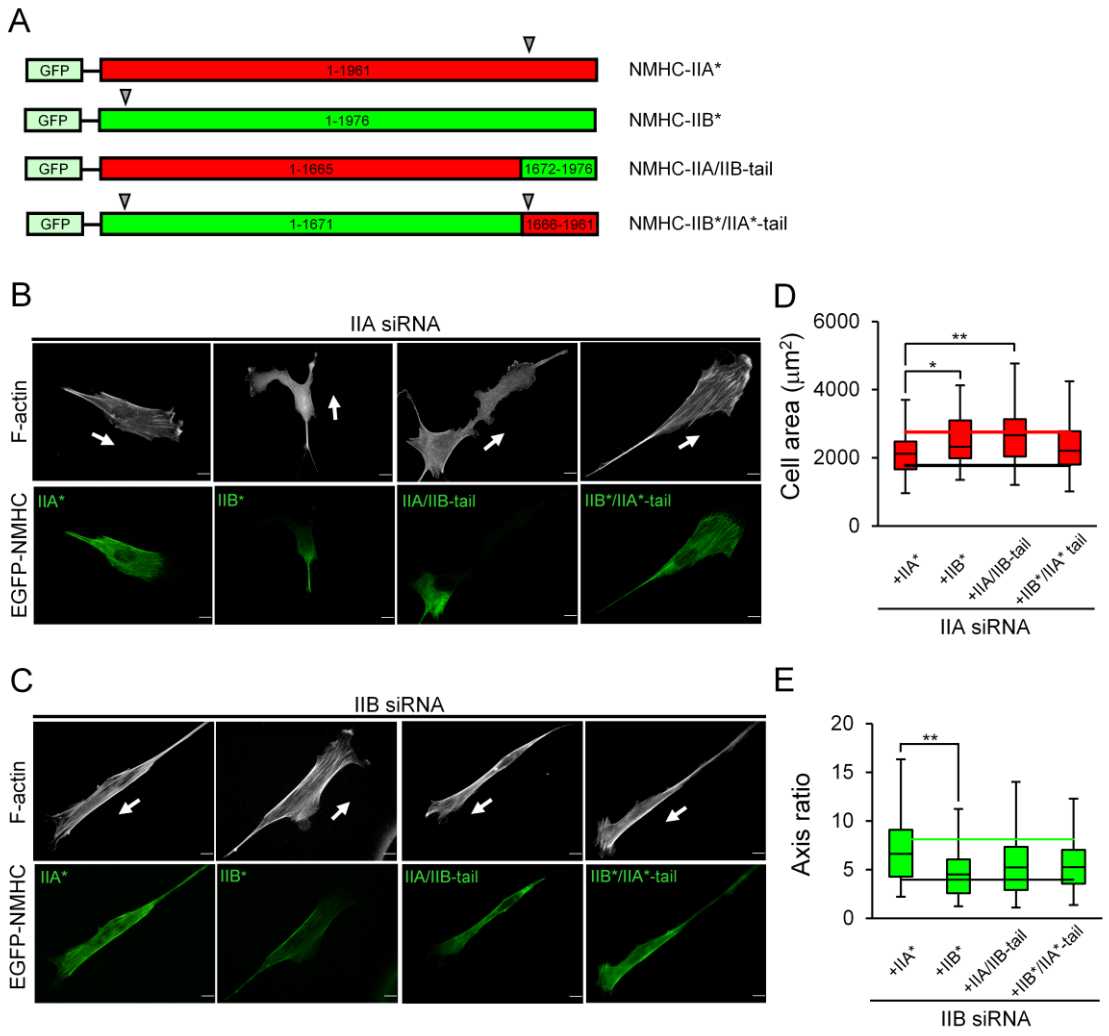

Figure 44. Rescue of morphological defects in NMIIA-KD and NMIIB-KD cells.

(A) Schematic diagrams of the NMHC-II constructs used in the KD-rescue experiments. Red and green represent regions corresponding to NMHC-IIA and NMHC-IIB, respectively. The numbers indicate the amino acid residues in the NMHC-II isoform of origin. Arrowheads indicate the target location of each siRNA. Asterisks indicate siRNA-insensitive constructs. There was no need to use the siRNA-insensitive form of NMHC-IIA/IIB-tail because it did not contain the target sequence of NMHC-IIA- or NMHC-IIB-specific siRNA. (B and C) Representative images of NMIIA-KD (B) and NMIIB-KD (C) TIG-1 cells expressing the indicated NMHC-II constructs. Fixed and permeabilized cells were stained with Alexa Fluor 350-conjugated phalloidin. White arrows indicate the expected direction of migration. Bar, 10 μm. (D and E) Cell area (D) and axis ratio (E) of cells in the conditions shown in (B) and (C), respectively (n > 40 cells/condition). Black and red lines indicate median values in control and NMIIA-KD cells, respectively (D). Black and green lines indicate median values in control and NMIIB-KD cells, respectively (E). *$P < 0.05$, **$P < 0.005$.

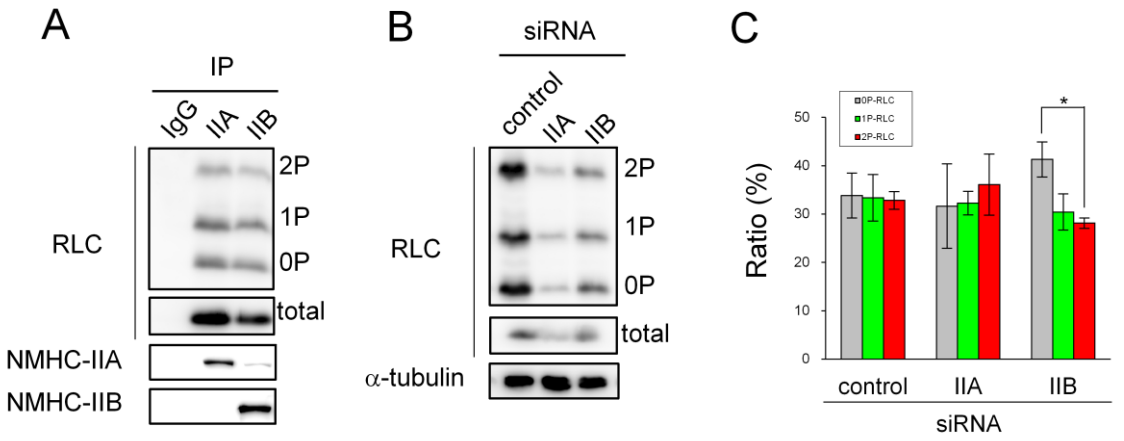

Figure 45. NMIIB is responsible for diphosphorylation of RLC and tension generation in the posterior region. (A and B) Immunoblot analyses of the immunoprecipitated NMII isoforms (A) and the indicated siRNA-treated cells (B). Top panel, Phos-tag SDS-PAGE; Other panels, standard SDS-PAGE. 0P, 1P, and 2P indicate the unphosphorylated, monophosphorylated, and diphosphorylated RLCs, respectively. (C) The ratio of each phosphorylation level of RLC in the indicated siRNA-treated cells was obtained from the immunoblot of Phos-tag SDS-PAGE (B). Data represent the mean ± SD from three independent experiments. $*P < 0.05$.

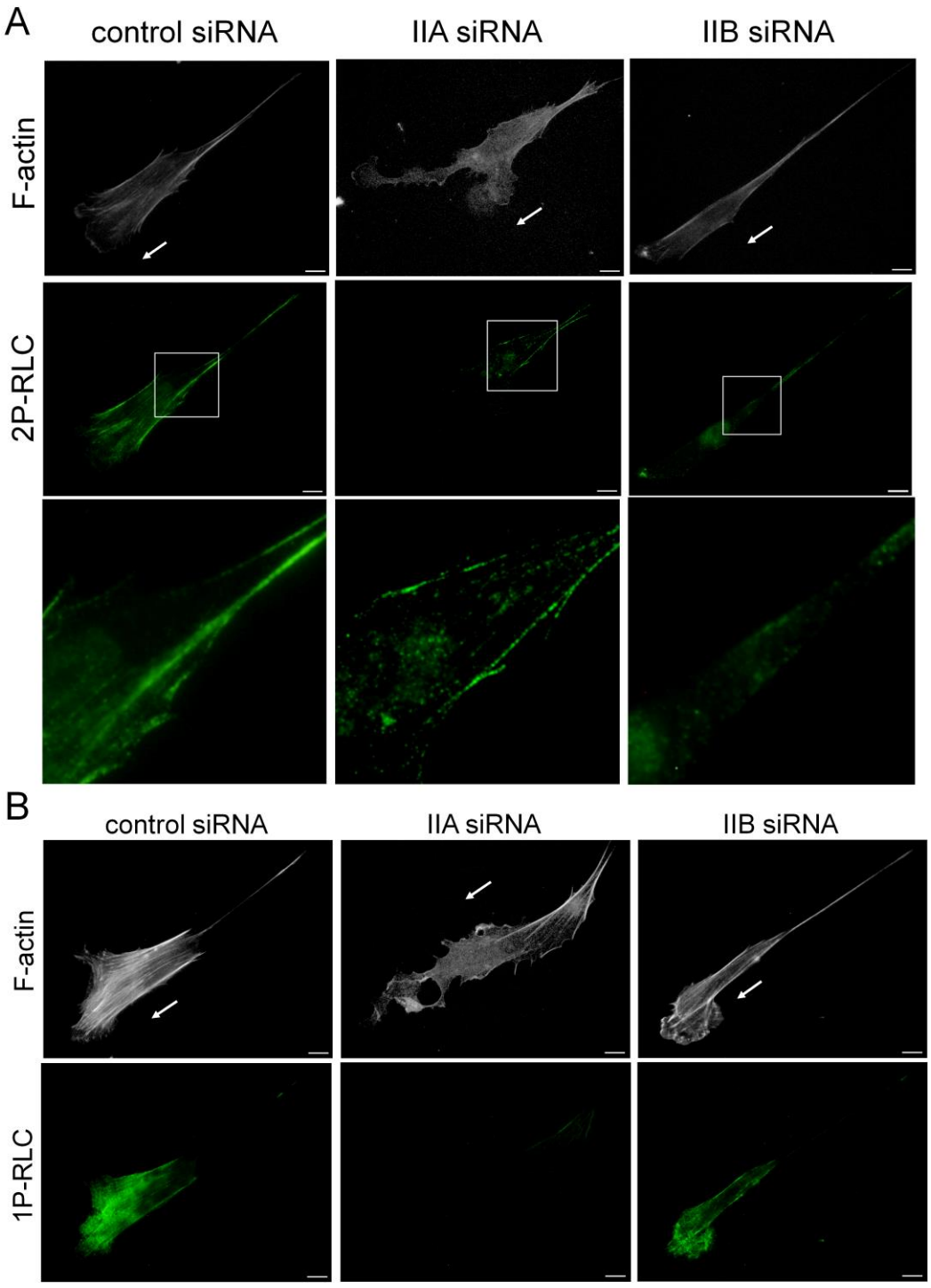

Figure 46. Localization of phosphorylated RLC in NMII isoform KD cells.
(A) Immunofluorescence of F-actin and 2P-RLC in the indicated siRNA-treated TIG-1 cells. White arrows indicate the apparent direction of migration. The bottom panels are the enlarged images of the boxed regions in the middle panels. (B) Immunofluorescence of F-actin and 1P-RLC in the indicated siRNA-treated TIG-1 cells. White arrows indicate direction of migration. Bar, 10 μm.

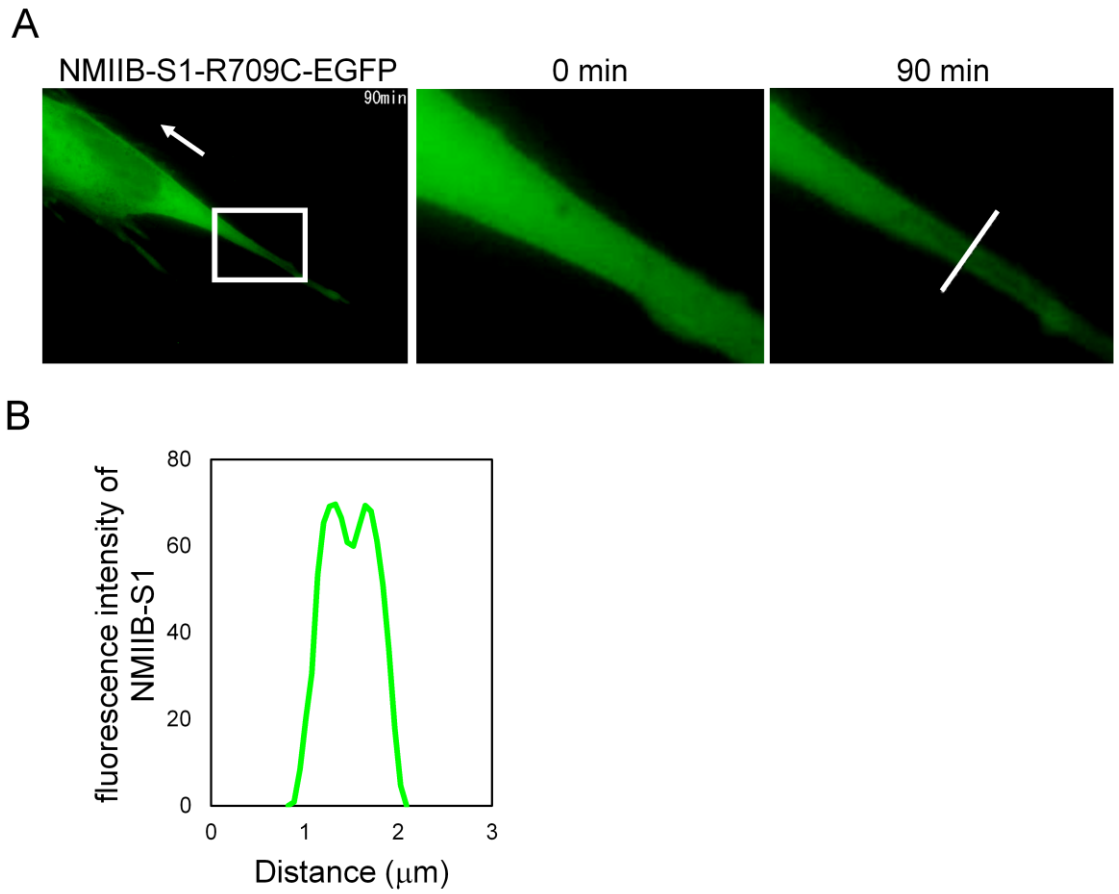

Figure 47. The localization of S1 probe in migrating TIG-1 cells.
(A) Still images showing the posterior region of a live migrating TIG-1 cell expressing S1 probe. All images were captured using a conventional fluorescence microscope. White arrows indicate direction of migration. Bar, 10 μm. Enlarged image of boxed region showed localization S1 probe at 0 min and 90 min. (B) A fluorescence intensity profile along the line in the enlarged image at 90 min (A).

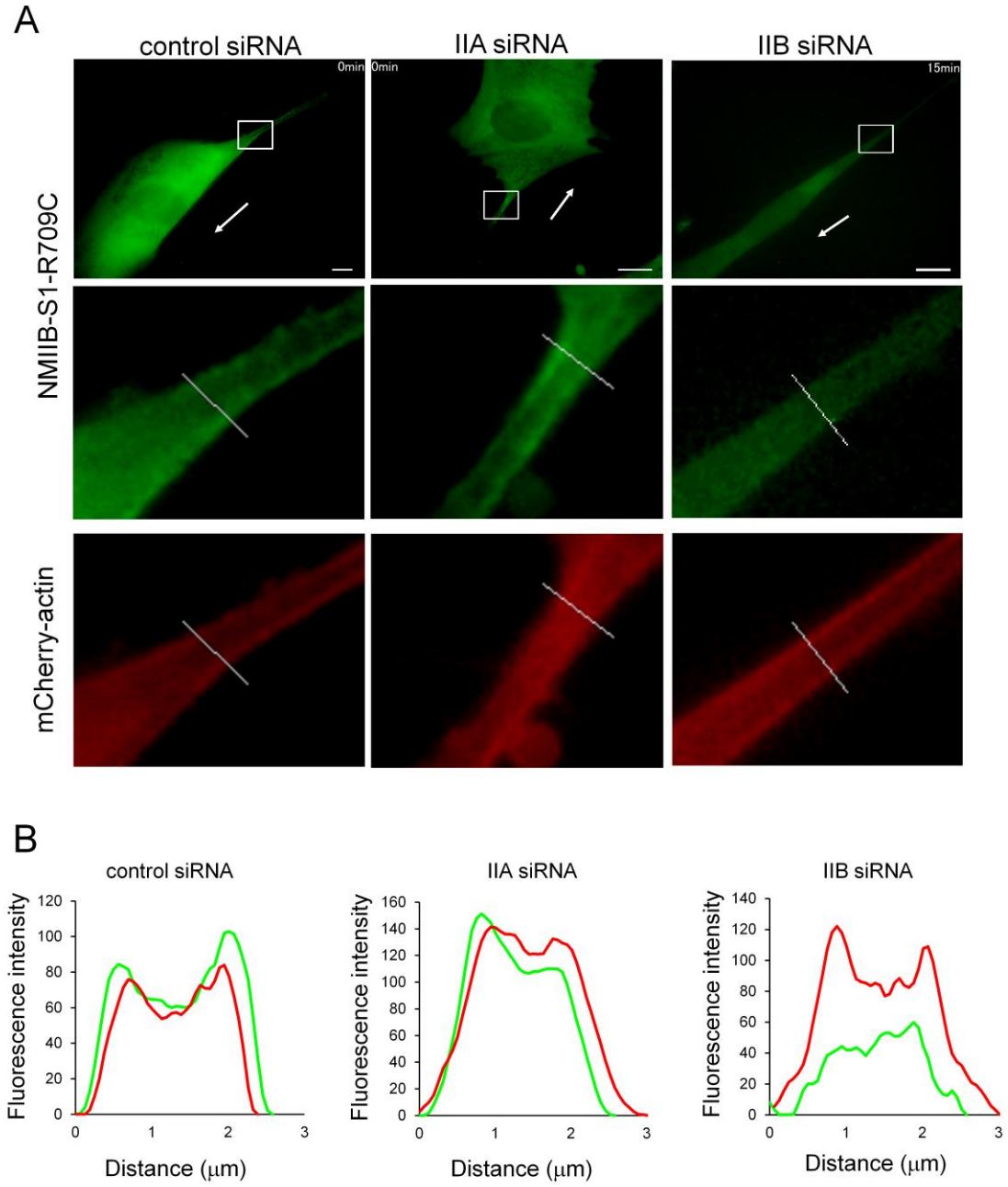

Figure 48. NMIIB is responsible for the tension generation in posterior region.
(A) Still images showing live control, NMIIA-KD and NMIIB-KD cells expressing S1 probe. All images were captured using a conventional fluorescence microscope. White arrows indicate direction of migration. Bar, 10 μm. Enlarged image of boxed region showed localization of S1 probe (top) and mCherry-actin (bottom). (B) Fluorescence intensity profiles along the lines in the middle panels of A showing the posterior regions of the indicated siRNA-treated TIG-1 cells expressing S1 probe and mCherry-actin. Lines were drawn at a position where the tail had a similar width in each condition. Green and Red lines indicate the fluorescence intensities of S1 probe and mCherry-actin, respectively.

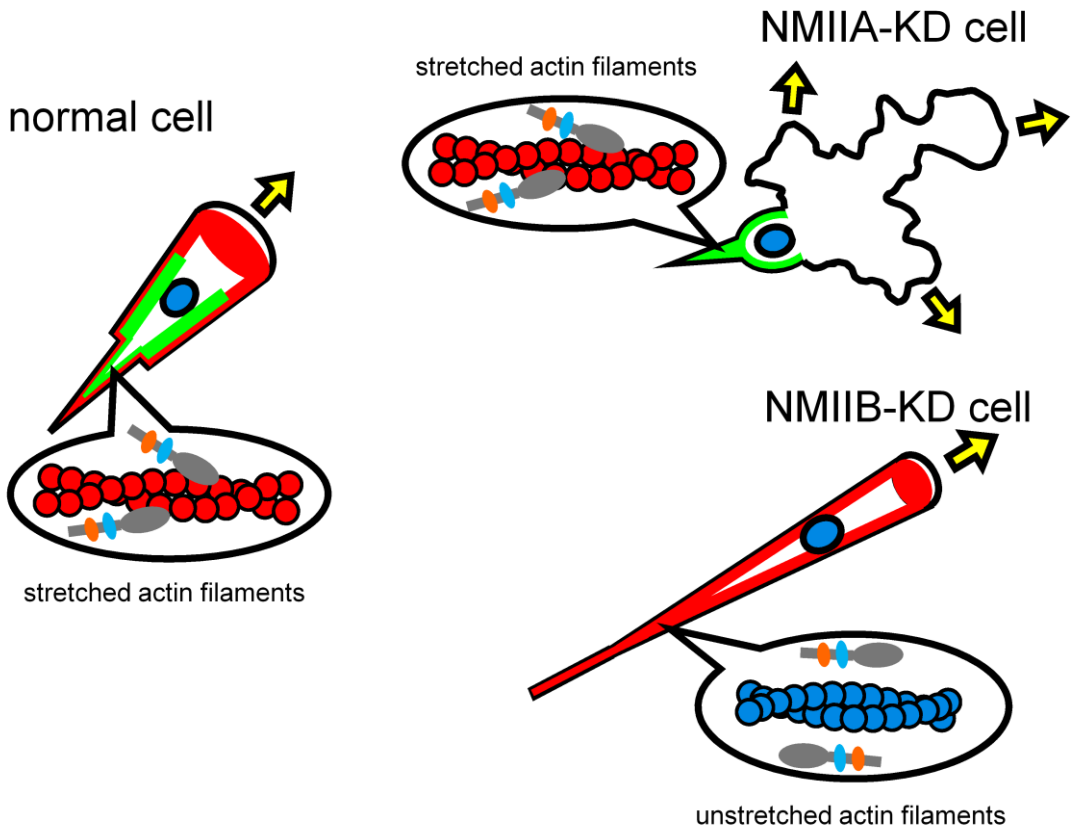

Figure 49. Model of conformational change of actin filaments in posterior region.
Because actin filaments in the tail region in normal cells and NMIIA-KD cells are stretched, S1 probe can localize there. Even though posterior region of cell body is elongated in NMIIB-KD cell, actin filaments in lateral stress fiber is not stretched. NMIIB-dependent tension generation is required for proper retraction of tail region.

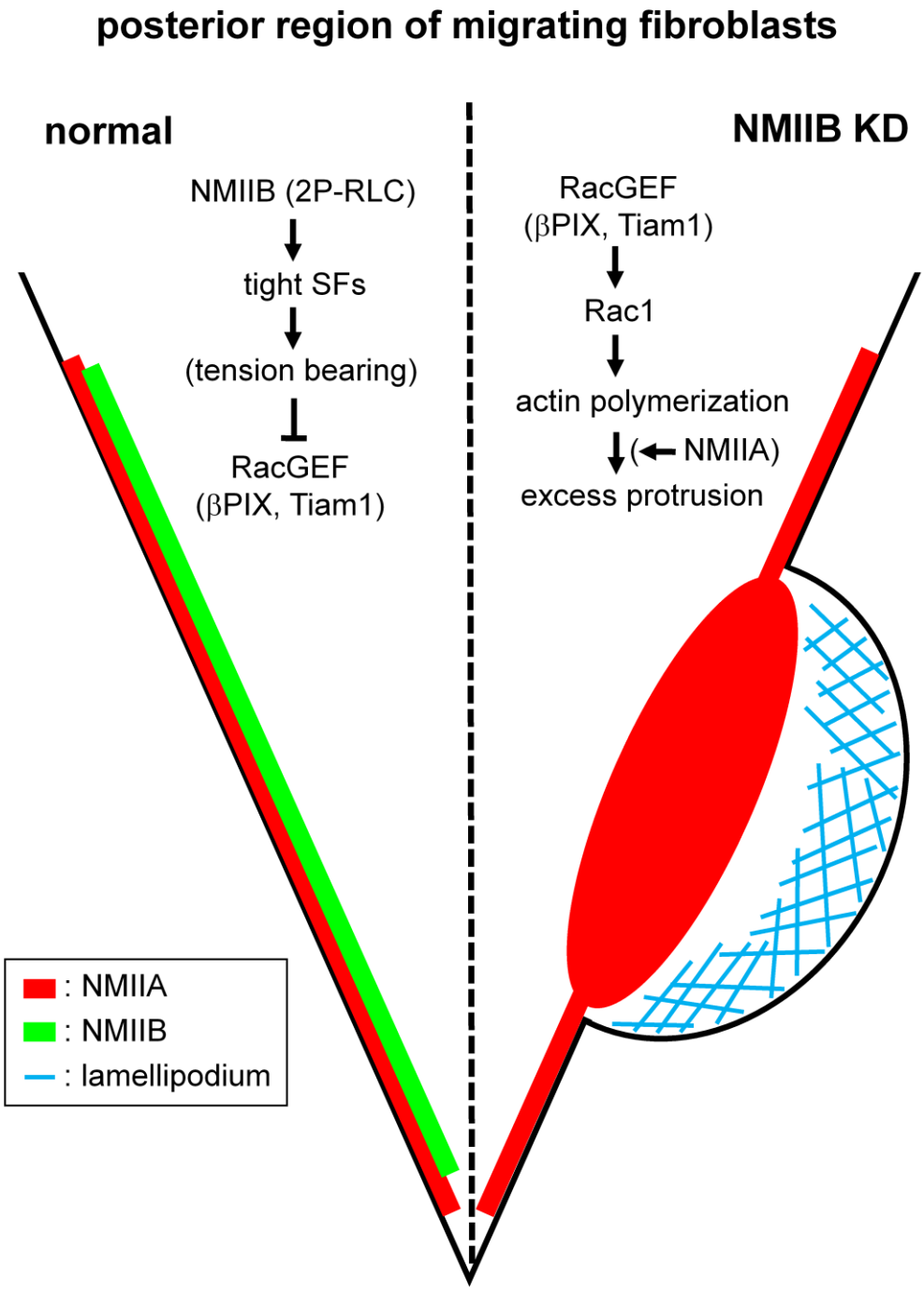

Figure 50. Schematic model for stabilization system of posterior region of migrating cells.
In the normal cells, NMIIB plays an essential role in preventing the formation of aberrant protrusions. High duty ratio and filament assembly ability of NMIIB allow formation of tight SFs, which might be functioned as a tension-bearing structure. These tight SFs might act a blocker of membrane protrusion, because NMIIB directly binds to the RacGEF (βPIX,Tiam1) [96] and inhibits the activation of Rac1 [39,55]. In NMIB-KD cells, RacGEF-Rac1 pathway is activated. Actin polymerization promoted by activation of Rac1 might cause a formation of an aberrant protrusion at the posterior region. Active NMIIA, which is localized there, might promote the advance of lamellipodia, resulting in the reversal of direction of migration.

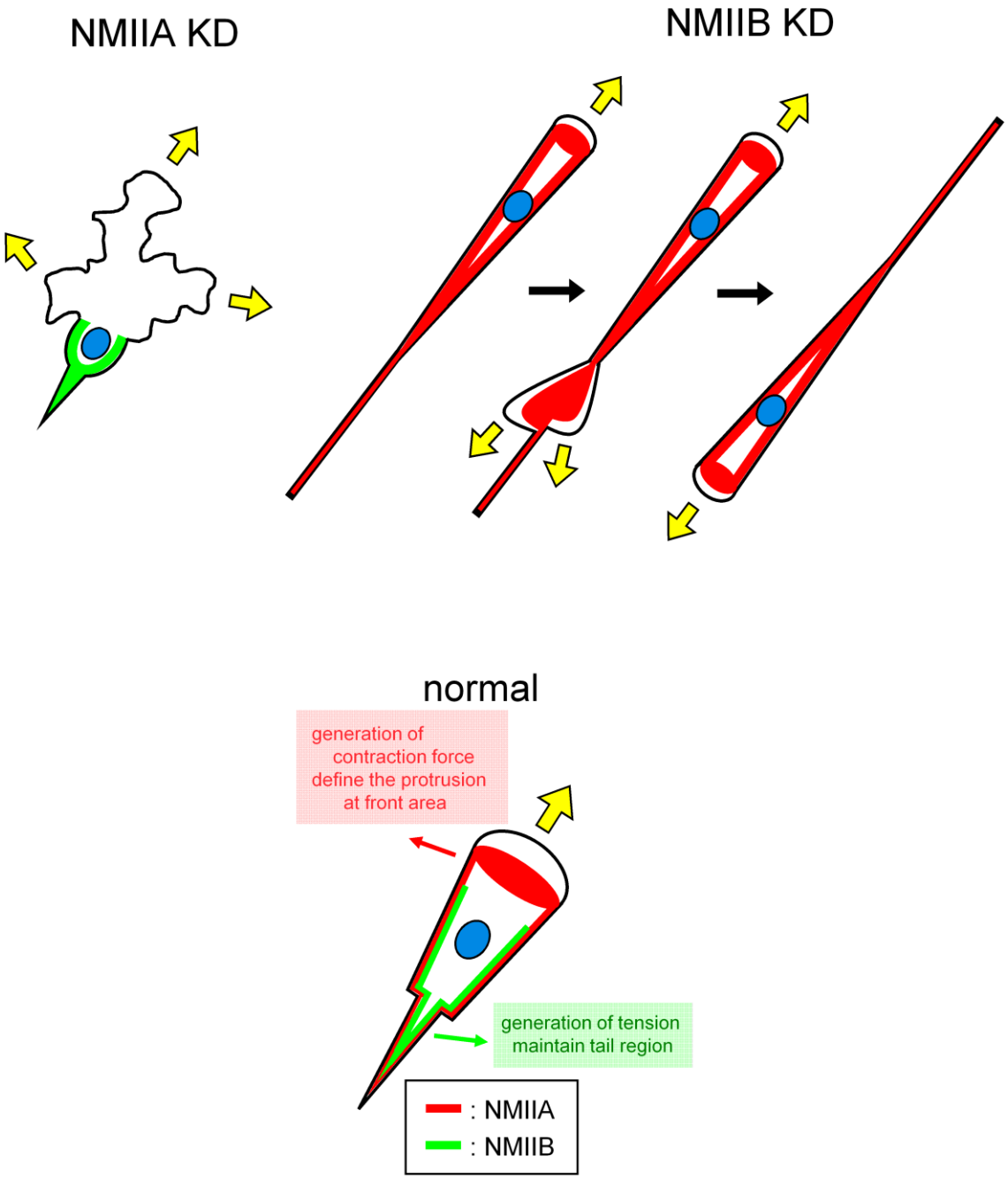

Figure 51. Schematic model of migration style in NMII isoform KD cell and normal cell.
The NMIIA-KD cells formed unstable protrusions in the anterior region and moved unsteadily but they were able to maintain the approximate direction. NMIIB-KD were likely to migrate in a directionally persistent manner for a while, but they inverted the direction of migration suddenly. NMIIA regulates protrusion in anterior region on the other hand, NMIIB keeps the front-rear polarity through tension-dependent inhibition of protrusion from posterior region.

General discussion

In this study, I investigated whether NMII isoforms have distinct roles in the organization of the SF subtypes and in the regulation of IDM. I mainly performed KD experiments using isoform-specific siRNAs and examined their effects on the organization of SF subtypes in immortalized human embryonic lung fibroblasts (SV1 cells) [99] and the migration style of normal human embryonic lung fibroblasts (TIG-1 cells) [100]. Further, I clarified the relationship between functions of NMII isoforms and generation of tension in the actomyoin cytoskeletal structures, utilizing the novel tension probe, NMIIB-S1-R709C-EGFP (S1 probe).

I propose a model for the roles of NMIIA and NMIIB in the actomyosin cytoskeletal structures (Figure 52). NMIIA and NMIIB have been suggested to mainly function in the translocation and crosslinking of actin filaments, respectively. Based on these molecular properties, I suppose that NMIIA and NMIIB are required for contraction and maintenance of contractility in the proper actomyosin cytoskeletal structures, respectively. When high load is applied to SFs, some actin filaments exhibit the stretched conformation in normal cells. The SFs in NMIIA-KD cells, which consisting of only NMIIB, may have a defect in contraction. Although NMIIB can translocate the actin filaments somewhat, NMIIB cannot completely replace the function of NMIIA. Consequently, the change of actin conformation of SFs in NMIIA-KD cells is smaller than that of normal cells. The SFs in NMIIB-KD cells may have a defect in maintenance of their contracted state, probably because NMII filaments lacking NMIIB might not be able to induce actin filaments to be stretched state. Thus, when a high load is applied to these SFs, they cannot resist it and maintain the contracted state. Consequently, the length between NMII filaments are increased and the SFs are elongated. Both of NMIIA and NMIIB would be required for the proper function of actomyosin cytoskeletons. Distinct properties of NMIIA and NMIIB would support the organization of the SF subtypes, the regulation of lamella flattening, and the IDM of normal fibroblasts.

In this study, focusing on two distinct stages concerning cell motile processes, organization of SF subtypes and cell migration, the isoform-specific functions of NMIIA and NMIIB derived from differences in the molecular properties were elucidated comprehensively. The main role of NMIIA might create dynamic properties on the cell shape, whereas the main role of NMIIB might resist the load that change the cell shape. Due to the mechanical rigidity, the region where NMIIB is present could exhibit strong resistance to the high mechanical load. It is interesting that the differences in the molecular properties of NMII isoforms greatly influence the properties of mechanical assembly of SFs and the style of migration. I believe that further development in the field of cell migration and mechanobiology would be brought by clarifying the relation between organization of SF subtypes and the mode of cell migration.

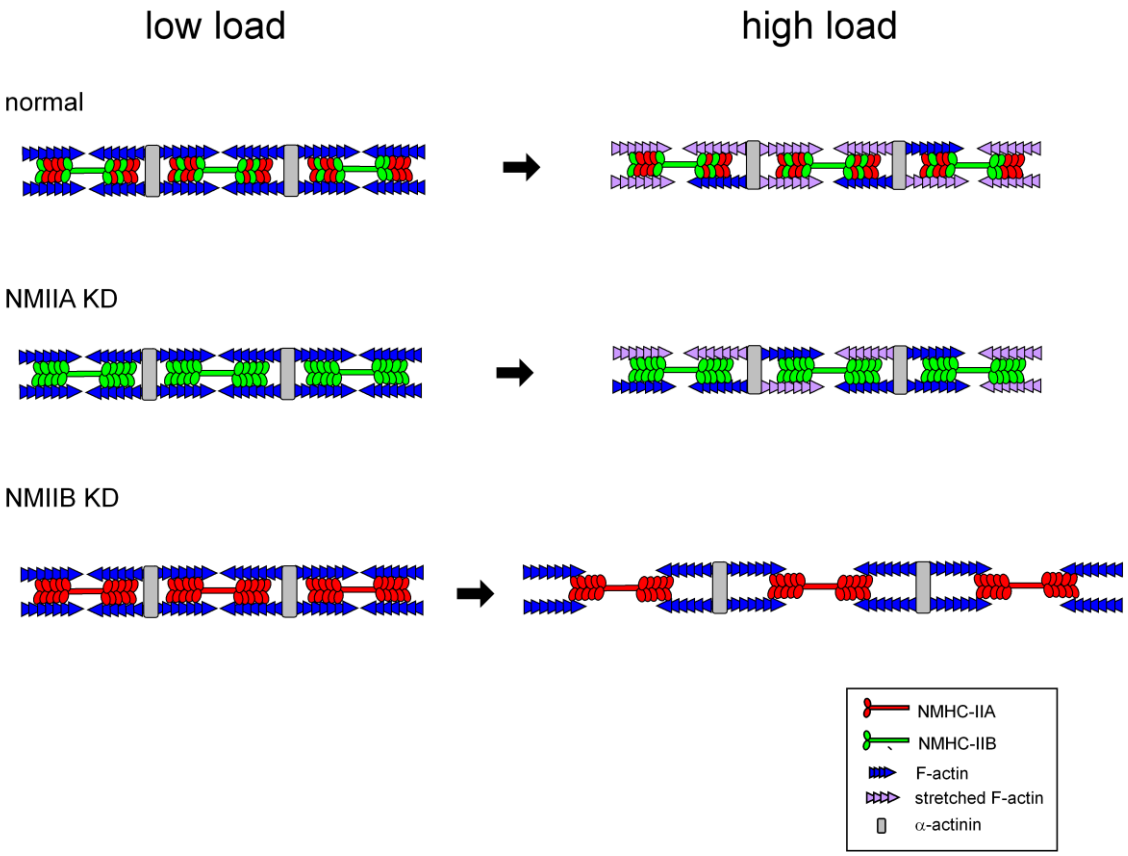

Figure 52. Schematic model for roles of NMIIA and NMIIB in actomyosin cytoskeletal structure.
Schematic model shows each condition of load applied SFs (Top; normal state, middle: NMIIA KD, bottom; NMIIB KD). Left and right panel indicate the states before and after loading, respectively. Note that NMIIA KD modestly causes decrease of stretched actin filaments. NMIB KD causes no stretching of actin filaments and fail to maintain the contraction state.

References

[1] M.A. Conti, R.S. Adelstein, Nonmuscle myosin II moves in new directions, J. Cell Sci. 121 (2008) 11–18.

[2] M. Vicente-Manzanares, X. Ma, R.S. Adelstein, A.R. Horwitz, Non-muscle myosin II takes centre stage in cell adhesion and migration, Nat. Rev. Mol. Cell Biol. 10 (2009) 778–790.

[3] S.M. Heissler, D.J. Manstein, Nonmuscle myosin-2: mix and match, Cell. Mol. Life Sci. 70 (2013) 1–21.

[4] M. Ikebe, J. Koretz, D.J. Hartshorne, Effects of phosphorylation of light chain residues threonine 18 and serine 19 on the properties and conformation of smooth muscle myosin, J. Biol. Chem. 263 (1988) 6432–6437.

[5] M. Ikebe, Phosphorylation of a second site for myosin light chain kinase on platelet myosin, Biochemistry 28 (1989) 8750–8755.

[6] B. Geiger, J.P. Spatz, A.D. Bershadsky, Environmental sensing through focal adhesions, Nat. Rev. Mol. Cell Biol. 10 (2009) 21–33.

[7] K. Ueda, M. Murata-Hori, M. Tatsuka, H. Hosoya, Rho-kinase contributes to diphosphorylation of myosin II regulatory light chain in nonmuscle cells, Oncogene. 21 (2002) 5852–5860.

[8] F. Matsumura, S. Ono, Y. Yamakita, G. Totsukawa, S. Yamashiro, Specific localization of serine 19 phosphorylated myosin II during cell locomotion and mitosis of cultured cells, J. Cell Biol. 140 (1998) 119–129.

[9] T. Saitoh, S. Takemura, K. Ueda, H. Hosoya, M. Nagayama, H. Haga, K. Kawabata, A. Yamagishi, M. Takahashi, Differential localization of non-muscle myosin II isoforms and phosphorylated regulatory light chains in human MRC-5 fibroblasts, FEBS Lett. 509 (2001) 365–369.

[10] S. Komatsu, M. Ikebe, ZIP kinase is responsible for the phosphorylation of myosin II and necessary for cell motility in mammalian fibroblasts, J. Cell Biol. 165 (2004) 243–254.

[11] N. Hirata, M. Takahashi, M. Yazawa, Diphosphorylation of regulatory light chain of myosin IIA is responsible for proper cell spreading, Biochem. Biophys. Res. Commun. 381 (2009) 682–687.

[12] L.J. Peterson, Z. Rajfur, A.S. Maddox, C.D. Freel, Y. Chen, M. Edlund, C. Otey, K. Burridge, Simultaneous stretching and contraction of stress fibers in vivo, Mol. Biol. Cell 15 (2004) 3497–3508.

[13] M. Shutova, C. Yang, J.M. Vasiliev, T. Svitkina, Functions of nonmuscle myosin II in assembly of the cellular contractile system, PLoS One. 7 (2012) e40814.

[14] B. Kovac, J.L. Teo, T.P. Mäkelä, T. Vallenius, Assembly of non-contractile dorsal stress fibers requires α-actinin-1 and Rac1 in migrating and spreading cells, J. Cell Sci. 126 (2013) 263–273.

[15] X. Ma, R.S. Adelstein, The role of vertebrate nonmuscle Myosin II in development and human disease, Bioarchitecture 4 (2014) 88–102.

[16] F. Wang, M. Kovács, A. Hu, J. Limouze, E. V Harvey, J.R. Sellers, Kinetic mechanism of non-muscle myosin IIB: functional adaptations for tension generation and maintenance, J. Biol. Chem. 278 (2003) 27439–27448.

[17] M. Kovács, F. Wang, A. Hu, Y. Zhang, J.R. Sellers, Functional divergence of human cytoplasmic myosin II: kinetic characterization of the non-muscle IIA isoform, J. Biol. Chem. 278 (2003) 38132–38140.

[18] S.S. Rosenfeld, J. Xing, L.-Q. Chen, H.L. Sweeney, Myosin IIb is unconventionally conventional, J. Biol. Chem. 278 (2003) 27449–27455.

[19] M. Kovács, K. Thirumurugan, P.J. Knight, J.R. Sellers, Load-dependent mechanism of nonmuscle myosin 2, Proc. Natl. Acad. Sci. U. S. A. 104 (2007) 9994–9999.

[20] O.M. Rossier, N. Gauthier, N. Biais, W. Vonnegut, M.-A. Fardin, P. Avigan, E.R. Heller, A. Mathur, S. Ghassemi, M.S. Koeckert, J.C. Hone, M.P. Sheetz, Force generated by actomyosin contraction builds bridges between adhesive contacts, EMBO J. 29 (2010) 1055–1068.

[21] S. Stam, J. Alberts, M.L. Gardel, E. Munro, Isoforms confer characteristic force generation and mechanosensation by myosin II filaments, Biophys. J. 108 (2015) 1997–2006.

[22] J.V. Small, K. Rottner, I. Kaverina, K.I. Anderson, Assembling an actin cytoskeleton for cell attachment and movement, Biochim. Biophys. Acta. 1404 (1998) 271–281.

[23] T. Vallenius, Actin stress fibre subtypes in mesenchymal-migrating cells, Open Biol. 3 (2013) 130001.

[24] C.T. Skau, C.M. Waterman, Specification of Architecture and Function of Actin Structures by Actin Nucleation Factors, Annu. Rev. Biophys. 44 (2015) 285–310.

[25] E. Kassianidou, S. Kumar, A biomechanical perspective on stress fiber structure and function, Biochim. Biophys. Acta. 1853 (2015) 3065–3074.

[26] S. Tojkander, G. Gateva, P. Lappalainen, Actin stress fibers--assembly, dynamics and biological roles, J. Cell Sci. 125 (2012) 1855–1864.

[27] J.P. Heath, Behaviour and structure of the leading lamella in moving fibroblasts. I. Occurrence and centripetal movement of arc-shaped microfilament bundles beneath the dorsal cell surface, J. Cell Sci. 60 (1983) 331–354.

[28] D.T. Burnette, S. Manley, P. Sengupta, R. Sougrat, M.W. Davidson, B. Kachar, J. Lippincott-Schwartz, A role for actin arcs in the leading-edge advance of migrating cells,

Nat. Cell Biol. 13 (2011) 371–381.

[29] S. Hu, K. Dasbiswas, Z. Guo, Y. Tee, V. Thiagarajan, P. Hersen, T. Chew, S.A. Safran, R. Zaidel-Bar, A.D. Bershadsky, Long-range self-organization of cytoskeletal myosin II filament stacks, Nat. Cell Biol. 19 (2017) 133–141.

[30] P. Hotulainen, P. Lappalainen, Stress fibers are generated by two distinct actin assembly mechanisms in motile cells, J. Cell Biol. 173 (2006) 383–394.

[31] P.W. Oakes, Y. Beckham, J. Stricker, M.L. Gardel, Tension is required but not sufficient for focal adhesion maturation without a stress fiber template, J. Cell Biol. 196 (2012) 363–374.

[32] D.T. Burnette, L. Shao, C. Ott, A.M. Pasapera, R.S. Fischer, M.A. Baird, C. Der Loughian, H. Delanoe-Ayari, M.J. Paszek, M.W. Davidson, E. Betzig, J. Lippincott-Schwartz, A contractile and counterbalancing adhesion system controls the 3D shape of crawling cells, J. Cell Biol. 205 (2014) 83–96.

[33] Q. Wei, R.S. Adelstein, Conditional expression of a truncated fragment of nonmuscle myosin II-A alters cell shape but not cytokinesis in HeLa cells, Mol. Biol. Cell 11 (2000) 3617–3627.

[34] Y. Cai, N. Biais, G. Giannone, M. Tanase, G. Jiang, J.M. Hofman, C.H. Wiggins, P. Silberzan, A. Buguin, B. Ladoux, M.P. Sheetz, Nonmuscle myosin IIA-dependent force inhibits cell spreading and drives F-actin flow, Biophys. J. 91 (2006) 3907–3920.

[35] J.C. Sandquist, K.I. Swenson, K.A. DeMali, K. Burridge, A.R. Means, Rho kinase differentially regulates phosphorylation of nonmuscle myosin II isoforms A and B during cell rounding and migration, J. Biol. Chem. 281 (2006) 35873–35883.

[36] V. Betapudi, L.S. Licate, T.T. Egelhoff, Distinct roles of nonmuscle myosin II isoforms in the regulation of MDA-MB-231 breast cancer cell spreading and migration, Cancer Res. 66 (2006) 4725–4733.

[37] S. Even-Ram, A.D. Doyle, M.A. Conti, K. Matsumoto, R.S. Adelstein, K.M. Yamada, Myosin IIA regulates cell motility and actomyosin-microtubule crosstalk, Nat. Cell Biol. 9 (2007) 299–309.

[38] M. Vicente-Manzanares, J. Zareno, L. Whitmore, C.K. Choi, A.F. Horwitz, Regulation of protrusion, adhesion dynamics, and polarity by myosins IIA and IIB in migrating cells, J. Cell Biol. 176 (2007) 573–580.

[39] M. Vicente-Manzanares, K. Newell-Litwa, A.I. Bachir, L.A. Whitmore, A.R. Horwitz, Myosin IIA/IIB restrict adhesive and protrusive signaling to generate front-back polarity in migrating cells, J. Cell Biol. 193 (2011) 381–396.

[40] V. Betapudi, Myosin II motor proteins with different functions determine the fate of lamellipodia extension during cell spreading, PLoS One 5 (2010) e8560.

[41] M.H. Jorrisch, W. Shih, S. Yamada, Myosin IIA deficient cells migrate efficiently despite reduced traction forces at cell periphery, Biol. Open 2 (2013) 368–372.

[42] C.-W. Chang, S. Kumar, Differential Contributions of Nonmuscle Myosin II Isoforms and Functional Domains to Stress Fiber Mechanics, Sci. Rep. 5 (2015) 13736.

[43] N. Schulze, M. Graessl, A. Blancke Soares, M. Geyer, L. Dehmelt, P. Nalbant, FHOD1 regulates stress fiber organization by controlling the dynamics of transverse arcs and dorsal fibers, J. Cell Sci. 127 (2014) 1379–1393.

[44] A.J. Ridley, M.A. Schwartz, K. Burridge, R.A. Firtel, M.H. Ginsberg, G. Borisy, J.T. Parsons, A.R. Horwitz, Cell Migration: Integrating Signals from Front to Back, Science 302 (2003) 1704–1709.

[45] R. Mayor, S. Etienne-Manneville, The front and rear of collective cell migration, Nat. Rev. Mol. Cell Biol. 17 (2016) 97–109.

[46] A.F.H. Douglas A. Lauffenburger, Cell Migration: Review A Physically Integrated Molecular Process, Cell 84 (1996) 359–369.

[47] T.J. Mitchison, L.P. Cramer, Actin-based cell motility and cell locomotion, Cell 84 (1996) 371–379.

[48] M. Raftopoulou, A. Hall, Cell migration: Rho GTPases lead the way, Dev. Biol. 265 (2004) 23–32.

[49] S.J. Heasman, A.J. Ridley, Mammalian Rho GTPases: New insights into their functions from in vivo studies, Nat. Rev. Mol. Cell Biol. 9 (2008) 690–701.

[50] R.J. Petrie, A.D. Doyle, K.M. Yamada, Random versus directionally persistent cell migration, Nat. Rev. Mol. Cell Biol. 10 (2009) 538–549.

[51] R. Pankov, Y. Endo, S. Even-Ram, M. Araki, K. Clark, E. Cukierman, K. Matsumoto, K.M. Yamada, A Rac switch regulates random versus directionally persistent cell migration, J. Cell Biol. 170 (2005) 793–802.

[52] P. Maupin, C.L. Phillips, R.S. Adelstein, T.D. Pollard, Differential localization of myosin-II isozymes in human cultured cells and blood cells, J. Cell Sci. 107 (1994) 3077–3090.

[53] J. Kolega, Cytoplasmic dynamics of myosin IIA and IIB: spatial "sorting" of isoforms in locomoting cells, J. Cell Sci. 111 (1998) 2085–2095.

[54] C.-M. Lo, D.B. Buxton, G.C.H. Chua, M. Dembo, R.S. Adelstein, Y.-L. Wang, Nonmuscle myosin IIb is involved in the guidance of fibroblast migration, Mol. Biol. Cell 15 (2004) 982–989.

[55] M. Vicente-Manzanares, M.A. Koach, L. Whitmore, M.L. Lamers, A.F. Horwitz, Segregation and activation of myosin IIB creates a rear in migrating cells, J. Cell Biol. 183 (2008) 543–554.

[56] M.K. Sato, M. Takahashi, M. Yazawa, Two regions of the tail are necessary for the

isoform-specific functions of nonmuscle myosin IIB, Mol. Biol. Cell. 18 (2007) 1009–1017.

[57] T. Kiboku, T. Katoh, A. Nakamura, A. Kitamura, M. Kinjo, Y. Murakami, M. Takahashi, Nonmuscle myosin II folds into a 10S form via two portions of tail for dynamic subcellular localization, Genes to Cells 18 (2013) 90–109.

[58] T.Q.P. Uyeda, Y. Iwadate, N. Umeki, A. Nagasaki, S. Yumura, Stretching actin filaments within cells enhances their affinity for the myosin II motor domain, PLoS One 6 (2011) e26200.

[59] K. Hayakawa, H. Tatsumi, M. Sokabe, Actin filaments function as a tension sensor by tension-dependent binding of cofilin to the filament, J. Cell Biol. 195 (2011) 721–727.

[60] V.E. Galkin, A. Orlova, E.H. Egelman, Actin filaments as tension sensors, Curr. Biol. 22 (2012) 96–101.

[61] K. Burridge, C. Guilluy, Focal adhesions, stress fibers and mechanical tension, Exp. Cell Res. 343 (2016) 14–20.

[62] N. Tang, E.M. Ostap, Motor domain-dependent localization of myo1b (myr-1), Curr. Biol. 11 (2001) 1131–1135.

[63] A. Hu, F. Wang, J.R. Sellers, Mutations in human nonmuscle myosin IIA found in patients with May-Hegglin anomaly and Fechtner syndrome result in impaired enzymatic function, J. Biol. Chem. 277 (2002) 46512–46517.

[64] K.-Y. Kim, M. Kovács, S. Kawamoto, J.R. Sellers, R.S. Adelstein, Disease-associated mutations and alternative splicing alter the enzymatic and motile activity of nonmuscle myosins II-B and II-C, J. Biol. Chem. 280 (2005) 22769–22775.

[65] T.D. Pollard, Mechanics of cytokinesis in eukaryotes, Curr. Opin. Cell Biol. 22 (2010) 50–56.

[66] J.L. Tan, J. Tien, D.M. Pirone, D.S. Gray, K. Bhadriraju, C.S. Chen, Cells lying on a bed of microneedles: An approach to isolate mechanical force, Proc. Natl. Acad. Sci. 100 (2003) 1484–1489.

[67] B. Sabass, M.L. Gardel, C.M. Waterman, U.S. Schwarz, High Resolution Traction Force Microscopy Based on Experimental and Computational Advances, Biophys. J. 94 (2008) 207–220.

[68] M. Dembo, Y.L. Wang, Stresses at the cell-to-substrate interface during locomotion of fibroblasts, Biophys. J. 76 (1999) 2307–2316.

[69] C. Grashoff, B.D. Hoffman, M.D. Brenner, R. Zhou, M. Parsons, M.T. Yang, M.A. Mclean, S.G. Sligar, C. S, T. Ha, M.A. Schwartz, R.M. Berne, Regulation of Focal Adhesion Dynamics, Nature 466 (2011) 263–266.

[70] N.S. Bryce, G. Schevzov, V. Ferguson, J.M. Percival, J.J.-C. Lin, F. Matsumura, J.R.

Bamburg, P.L. Jeffrey, E.C. Hardeman, P. Gunning, R.P. Weinberger, Specification of actin filament function and molecular composition by tropomyosin isoforms, Mol. Biol. Cell 14 (2003) 1002–1016.

[71] S. Tojkander, G. Gateva, G. Schevzov, P. Hotulainen, P. Naumanen, C. Martin, P.W. Gunning, P. Lappalainen, A molecular pathway for myosin II recruitment to stress fibers, Curr. Biol. 21 (2011) 539–550.

[72] G. Gateva, E. Kremneva, T. Reindl, T. Kotila, K. Kogan, L. Gressin, P.W. Gunning, D.J. Manstein, A. Michelot, P. Lappalainen, Tropomyosin Isoforms Specify Functionally Distinct Actin Filament Populations In Vitro, Curr. Biol. 27 (2017) 705–713.

[73] J.R. Beach, L. Shao, K. Remmert, D. Li, E. Betzig, J.A. Hammer, Nonmuscle myosin II isoforms coassemble in living cells, Curr. Biol. 24 (2014) 1160–1166.

[74] M.S. Shutova, W.A. Spessott, C.G. Giraudo, T. Svitkina, Endogenous species of mammalian nonmuscle myosin IIA and IIB include activated monomers and heteropolymers, Curr. Biol. 24 (2014) 1958–1968.

[75] M. Chrzanowska-Wodnicka, K. Burridge, Rho-stimulated contractility drives the formation of stress fibers and focal adhesions, J. Cell Biol. 133 (1996) 1403–1415.

[76] M.L. Gardel, I.C. Schneider, Y. Aratyn-Schaus, C.M. Waterman, Mechanical integration of actin and adhesion dynamics in cell migration, Annu. Rev. Cell Dev. Biol. 26 (2010) 315–333.

[77] G. Totsukawa, Y. Yamakita, S. Yamashiro, D.J. Hartshorne, Y. Sasaki, F. Matsumura, Distinct roles of ROCK (Rho-kinase) and MLCK in spatial regulation of MLC phosphorylation for assembly of stress fibers and focal adhesions in 3T3 fibroblasts, J. Cell Biol. 150 (2000) 797–806.

[78] A.M. Fenix, N. Taneja, C.A. Buttler, J. Lewis, S.B. Van Engelenburg, R. Ohi, D.T. Burnette, Expansion and concatenation of nonmuscle myosin IIA filaments drive cellular contractile system formation during interphase and mitosis, Mol. Biol. Cell 27 (2016) 1465–1478.

[79] M.A. Titus, Growing, splitting and stacking myosin II filaments, Nat. Cell Biol. 19 (2017) 77–79.

[80] K. Tokuraku, R. Kurogi, R. Toya, T.Q.P. Uyeda, Novel mode of cooperative binding between myosin and Mg2+ -actin filaments in the presence of low concentrations of ATP, J. Mol. Biol. 386 (2009) 149–162.

[81] J.R. Beach, J.A. Hammer, Myosin II isoform co-assembly and differential regulation in mammalian systems, Exp. Cell Res. 334 (2015) 2–9.

[82] J.C. Sandquist, A.R. Means, The C-terminal tail region of nonmuscle myosin II directs isoform-specific distribution in migrating cells, Mol. Biol. Cell 19 (2008) 5156–5167.

[83] J.R. Beach, K.S. Bruun, L. Shao, D. Li, Z. Swider, K. Remmert, Y. Zhang, M.A. Conti, R.S. Adelstein, N.M. Rusan, E. Betzig, J.A. Hammer, Actin dynamics and competition for myosin monomer govern the sequential amplification of myosin filaments, Nat. Cell Biol. 19 (2017) 85–93.

[84] S. Tojkander, G. Gateva, A. Husain, R. Krishnan, P. Lappalainen, Generation of contractile actomyosin bundles depends on mechanosensitive actin filament assembly and disassembly, Elife. 4 (2015) e06126.

[85] J. Bao, S.S. Jana, R.S. Adelstein, Vertebrate nonmuscle myosin II isoforms rescue small interfering RNA-induced defects in COS-7 cell cytokinesis, J. Biol. Chem. 280 (2005) 19594–19599.

[86] R. Takeya, K. Taniguchi, S. Narumiya, H. Sumimoto, The mammalian formin FHOD1 is activated through phosphorylation by ROCK and mediates thrombin-induced stress fibre formation in endothelial cells, EMBO J. 27 (2008) 618–628.

[87] S.-F. Ang, Z. Zhao, L. Lim, E. Manser, DAAM1 is a formin required for centrosome re-orientation during cell migration, PLoS One. 5 (2010).

[88] S. Deguchi, M. Sato, Biomechanical properties of actin stress fibers of non-motile cells, Biorheology. 46 (2009) 93–105.

[89] D.G. Thomas, A. Yenepalli, C.M. Denais, A. Rape, J.R. Beach, Y. -l. Wang, W.P. Schiemann, H. Baskaran, J. Lammerding, T.T. Egelhoff, Non-muscle myosin IIB is critical for nuclear translocation during 3D invasion, J. Cell Biol. 210 (2015) 583–594.

[90] M.S. Shutova, S.B. Asokan, S. Talwar, R.K. Assoian, J.E. Bear, T.M. Svitkina, Self-sorting of nonmuscle myosins IIA and IIB polarizes the cytoskeleton and modulates cell motility, J. Cell Biol. 216 (2017) 2877–2889.

[91] G.W.G. Luxton, G.G. Gundersen, Orientation and function of the nuclear-centrosomal axis during cell migration, Curr. Opin. Cell Biol. 23 (2011) 579–588.

[92] M. Raab, J. Swift, P.C.D.P. Dingal, P. Shah, J.W. Shin, D.E. Discher, Crawling from soft to stiff matrix polarizes the cytoskeleton and phosphoregulates myosin-II heavy chain, J. Cell Biol. 199 (2012) 669–683.

[93] T. Nakasawa, M. Takahashi, F. Matsuzawa, S. Aikawa, Y. Togashi, T. Saitoh, A. Yamagishi, M. Yazawa, Critical regions for assembly of vertebrate nonmuscle myosin II, Biochemistry. 44 (2005) 174–183.

[94] A. Juanes-Garcia, J.R. Chapman, R. Aguilar-Cuenca, C. Delgado-Arevalo, J. Hodges, L.A. Whitmore, J. Shabanowitz, D.F. Hunt, A.R. Horwitz, M. Vicente-Manzanares, A regulatory motif in nonmuscle myosin II-B regulates its role in migratory front-back polarity, J. Cell Biol. 209 (2015) 23–32.

[95] M. Krause, A. Gautreau, Steering cell migration: Lamellipodium dynamics and the

regulation of directional persistence, Nat. Rev. Mol. Cell Biol. 15 (2014) 577–590.

[96] C.S. Lee, C.K. Choi, E.Y. Shin, M.A. Schwartz, E.G. Kim, Myosin II directly binds and inhibits Dbl family guanine nucleotide exchange factors: A possible link to Rho family GTPases, J. Cell Biol. 190 (2010) 663–674.

[97] W.H. Guo, Y.L. Wang, A three-component mechanism for fibroblast migration with a contractile cell body that couples a myosin II-independent propulsive anterior to a myosin II-dependent resistive tail, Mol. Biol. Cell 23 (2012) 1657–1663.

[98] J. Zhang, Y.L. Wang, Centrosome defines the rear of cells during mesenchymal migration, Mol. Biol. Cell 28 (2017) 3240–3251.

[99] M. Kuragano, T.Q. Uyeda, K. Kamijo, Y. Murakami, M. Takahashi, Different contributions of nonmuscle myosin IIA and IIB to the organization of stress fiber subtypes in fibroblasts, Mol. Biol. Cell 29 (2018) 911-922.

[100] M. Kuragano, Y. Murakami, M. Takahashi, Nonmuscle myosin IIA and IIB differentially contribute to intrinsic and directed migration of human embryonic lung fibroblasts, Biochem. Biophys. Res. Commun. 498 (2018) 25–31.

Acknowledgement

I express my gratitude to Professor Yota Murakami of Hokkaido University for his helpful advice, encouragement, suggestion and discussion.

I would like to express my deepest appreciation to Associate professor Masayuki Takahashi of Hokkaido University for his helpful advice, encouragement, suggestion and discussion.

I would like to express my gratitude to Adjunct associate professor Akiko Nakatomi of Hokkaido University for her enormous supports, insightful comment and strong encouragement.

I would like to thank Assistant professor Shinya Takahata of Hokkaido University for his enormous support and insightful comment.

I am very grateful to Dr. Yo Okamoto and Dr. Michio Yazawa for their enormous supports and guidance.

I would like to express my gratitude to Professor Kazuyasu Sakaguchi of Hokkaido University for accepting the chairman of my doctoral dissertation.

I would like to express my gratitude to Professor Yasuyuki Fujita and Professor Mutsumi Takagi of Hokkaido University for accepting the vice-chairman of my doctoral dissertation.

I am very grateful to Professor Taro Uyeda of Waseda University for his helpful advice about development of tension probe.

I am very grateful to Professor Keiju Kamijo of Tohoku Medical and Pharmaceutical University for helpful advice, suggestion and discussion.

I am grateful to Professor Hisashi Haga of Hokkaido University and Associate professor Takeomi Mizutani of Hokkai-Gakuen University for helpful advice on the cell stretching assay.

I am grateful to the Dr. Kentaro Kobayashi of Hokkaido University Nikon Imaging Center for assistance with microscopy, image acquisition, and analysis.

I would like to thank Dr. Takayuki Kiboku and Dr. Naoya Hirata of National Institute of Health Sciences for their technical guidance in some experiments.

I would like to thank Assistant professor Masaaki Sato of Marianna University School of Medicine for his advice about analysis of cell migration.

I would like to thank Dr. Hirotsugu Hino of Tokyo Medical University for his support and advice.

I am thankful to all the members of Bioorganic Laboratory of Hokkaido University.

Finally, I would like to extend my indebtedness to my parents, my grandparents, my sister and my brother for their endless love, understanding, support and sacrifice throughout my study.